AD_____

Award Number: W81XWH-08-1-0113

TITLE: Imaging Heat Shock Protein 90 (Hsp90) Activity in Hormone-Refractory Prostate Cancer

PRINCIPAL INVESTIGATOR: Gang Niu

CONTRACTING ORGANIZATION: Leland Stanford Junior Unversity
Stanford, CA 94305

REPORT DATE: January 2011

TYPE OF REPORT: Final

PREPARED FOR: U.S. Army Medical Research and Materiel Command
Fort Detrick, Maryland 21702-5012

DISTRIBUTION STATEMENT: Approved for public release; distribution unlimited

The views, opinions and/or findings contained in this report are those of the author(s) and should not be construed as an official Department of the Army position, policy or decision unless so designated by other documentation.

REPORT DOCUMENTATION PAGE

Form Approved
OMB No. 0704-0188

Public reporting burden for this collection of information is estimated to average 1 hour per response, including the time for reviewing instructions, searching existing data sources, gathering and maintaining the data needed, and completing and reviewing this collection of information. Send comments regarding this burden estimate or any other aspect of this collection of information, including suggestions for reducing this burden to Department of Defense, Washington Headquarters Services, Directorate for Information Operations and Reports (0704-0188), 1215 Jefferson Davis Highway, Suite 1204, Arlington, VA 22202-4302. Respondents should be aware that notwithstanding any other provision of law, no person shall be subject to any penalty for failing to comply with a collection of information if it does not display a currently valid OMB control number. **PLEASE DO NOT RETURN YOUR FORM TO THE ABOVE ADDRESS.**

1. REPORT DATE *(DD-MM-YYYY)*	2. REPORT TYPE	3. DATES COVERED *(From - To)*
01-01-2011	Annual Summary	25 FEB 2008 - 24 FEB 2010

4. TITLE AND SUBTITLE
Imaging Heat Shock Protein 90 (Hsp90) Activity in Hormone-Refractory Prostate Cancer

5a. CONTRACT NUMBER

5b. GRANT NUMBER
W81XWH-08-1-0113

5c. PROGRAM ELEMENT NUMBER

6. AUTHOR(S)
Gang Niu

E-Mail: gniu@stanford.edu

5d. PROJECT NUMBER

5e. TASK NUMBER

5f. WORK UNIT NUMBER

7. PERFORMING ORGANIZATION NAME(S) AND ADDRESS(ES)
Leland Stanford Junior Unversity
Stanford, CA 94305

8. PERFORMING ORGANIZATION REPORT NUMBER

9. SPONSORING / MONITORING AGENCY NAME(S) AND ADDRESS(ES)
U.S. Army Medical Research and Materiel Command
Fort Detrick, Maryland 21702-5012

10. SPONSOR/MONITOR'S ACRONYM(S)

11. SPONSOR/MONITOR'S REPORT NUMBER(S)

12. DISTRIBUTION / AVAILABILITY STATEMENT
Approved for Public Release; Distribution Unlimited

13. SUPPLEMENTARY NOTES

14. ABSTRACT

During the first year of the funding period, we have labeled 1, 3-propoyldiamine modified geldanamycin with both fluorescent core (FITC in this case) and radioisotopes. Unfortunately, in vitro cell experiments failed to disclose the ability of FITC-GM to monitor Hsp90 activity changes after heat stimulation in prostate cancer cell lines. Small molecular Hsp90 inhibitors, at least GM derivatives, showed reasonable tumor accumulation after being labeled with 64Cu. However, in vitro experiments revealed that the GM derivatives are insufficient to tell the changes of both Hsp90 level and activity after stimulation. It might be more appropriate to use GM imaging for tumor detection instead of Hsp90 activity monitoring. Therefore, we switched gears to monitor Hsp90 activity indirectly through imaging downstream client proteins including EGFR and HER2 expression by 64Cu labeled antibodies. Hsp90 activity can be evaluated indirectly by imaging one or several of its downstream client proteins. The quantitative PET imaging of EGFR expression with 64Cu-DOTA-cetuximab is successful for monitoring the early therapeutic response upon 17-AAG treatment in a human prostate cancer PC-3 tumor model. The quantification of EGFR degradation upon 17-AAG treatment using PET imaging is consistent with other in vitro and ex vivo measurements. This strategy may be applied to monitor the therapeutic response in EGFR-positive cancer patients under 17-AAG treatment.

15. SUBJECT TERMS
None provided.

16. SECURITY CLASSIFICATION OF:			17. LIMITATION OF ABSTRACT	18. NUMBER OF PAGES	19a. NAME OF RESPONSIBLE PERSON
a. REPORT	b. ABSTRACT	c. THIS PAGE			USAMRMC
U	U	U	UU	74	19b. TELEPHONE NUMBER *(include area code)*

Table of Contents

Page

Introduction……..4

Body……5

Key Research Accomplishments……..10

Reportable Outcomes……11

Conclusion……12

References……13

Appendices……14

INTRODUCTION

Based on the extremely important function of Hsp90 in the survival and proliferation of tumor cells, the therapy focusing on Hsp90 inhibition will become a potentially important prostate cancer treatment strategy, especially for refractory prostate cancers. In the research proposal, we hypothesized that Hsp90 activity, *i.e.* the amount of active form of Hsp90, is the main determining factor for the response to Hsp90 inhibition therapy. The first goal is to develop probes to monitor Hsp90 activity non-invasively. We speculated that PET imaging with suitably radiolabled Hsp90 substrates will be highly valuable in assessing Hsp90 activity non-invasively and repetitively. The major objective of this 2-year training proposal is to image prostate cancer Hsp90 activity in vivo.

During the first year of the funding period, we have labeled 1, 3-propoyldiamine modified geldanamycin with both fluorescent core (FITC in this case) and radioisotopes. Unfortunately, in vitro cell experiments failed to disclose the ability of FITC-GM to monitor Hsp90 activity changes after heat stimulation in prostate cancer cell lines. The emerging literature also revealed that highly nonspecific cellular binding is the main barrier for the hyperlipophilic small molecules including GM. Therefore, we switched gears to monitor Hsp90 activity indirectly through imaging downstream client proteins including EGFR and HER2 expression by ^{64}Cu labeled antibodies.

The assessment of early response to anti-cancer therapy can improve patient care by identifying patients who do not respond and, therefore, may not benefit from the therapy. These patients can greatly benefit from avoiding unnecessary toxic side effects and switching to different, more effective therapeutic approaches in a timely manner. Compared to 2-deoxy-2-[F-18]fluoro-Dglucose (FDG)–PET, which measured the tumor glucose metabolism, PET imaging of EGFR and HER-2 expression provided more accurate information for early tumor response to Hsp90 inhibitors (17-AAG or 17-DMAG) treatment in both prostate and ovarian cancer models..

BODY

Part I. GM derivatives failed to detect Hsp90 activity changes

Geldanamycin (GM) was reacted with 1,3-propoyldiamine to afford 17-trimethylenediamine-17-demthyoxygeldanamycin (TD), which was then conjugated with activated DOTA ester to afford DOTA-TD) for ^{64}Cu labeling. Mice bearing human glioma U87MG tumors were then subjected to microPET scans at various time points post-injection (p.i.) of ^{64}Cu-DOTA-TD. The coronal slices that contain the tumor are shown in **Fig. 1.** The uptake of ^{64}Cu-DOTA-TD into U87MG tumor was rapid and high, reaching a peak at 18 h p.i. Liver and kidney also exhibited relatively high tracer uptake. The uptake in most other organs was at very low level. The uptake in the kidneys dropped steadily over time **(Fig. 1).**

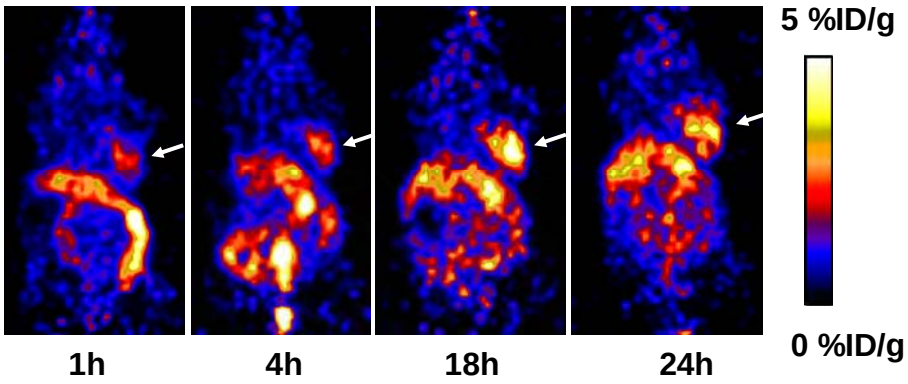

Fig. 1. MicroPET imaging of Hsp90 activity by ^{64}Cu-DOTA-TD in U87MG tumor-bearing nude mice (arrow).

After this initial success of labeling Hsp90 substrate for PET imaging, we performed in vitro experiments to explore whether the uptake of ^{64}Cu-DOTA-TD is related to Hsp90 protein level and Hsp90 ATPase activity. For in vitro uptake assay, 1 x 10^5 PC-3 cells were seeded in 24-well plates 48 h prior to uptake assay. In the stress group, cells were cultured in serum free medium (SFM) for 24 h. Then 18.5 kBq of ^{64}Cu-labeled GM was added to each well in 0.5 ml of SFM. At different time points after adding ^{64}Cu-GM, the medium was removed and the cells were washed twice with 1 ml of ice-cold PBS. Finally cells from each well were collected and the radioactivity (counts per minute) was measured with a gamma counter (Cobra II, Packard, USA). The results were shown in **Fig. 2.** The accumulation of ^{64}Cu-DOTA-GM increased along with time. Compared with control cells, however, the stressed PC-3 did not show significantly higher uptake of ^{64}Cu-DOTA-GM.

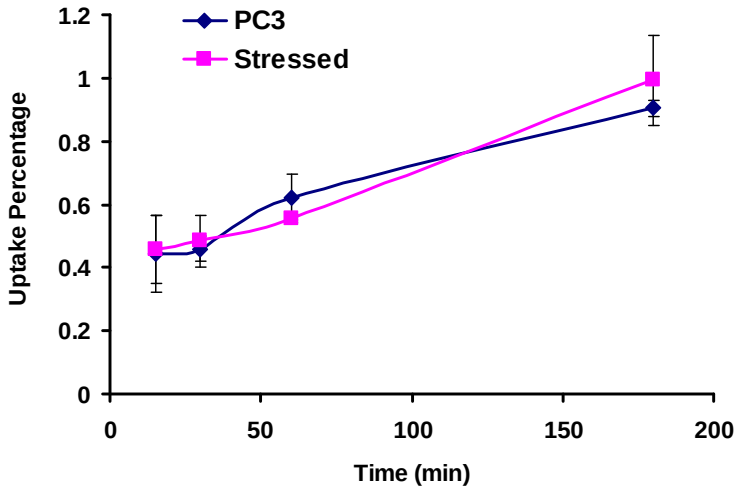

Fig. 2. Uptake assay of ^{64}Cu-GM in PC3 cells

We further modified GM and labeled it with FITC according to the reaction scheme provided in **Fig. 3A**. We then stimulated Hsp90 expression and activation in both PC3 and 22RV1 cells by heat or PMA. Still, we did not observe significant difference of signal intensity visualized by fluorescence microscope **(Fig. 3B)**.

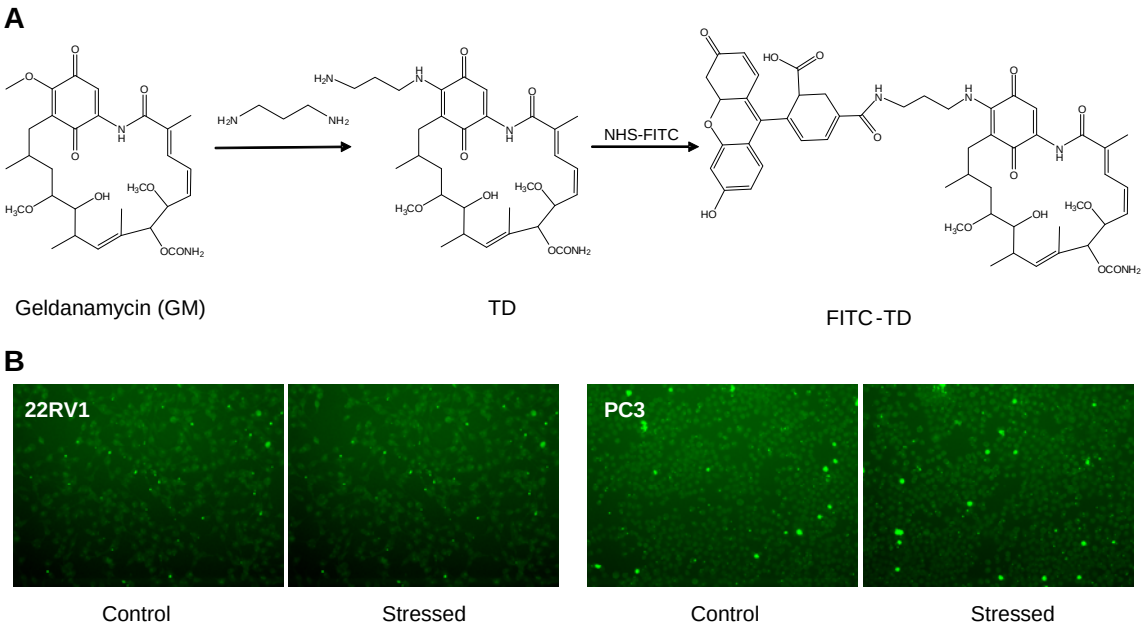

Fig. 3. (A) Synthesis of FITC-GM; **(B)** Monitoring Hsp90 activity with FITC-GM in prostate cancer cell lines.

We concluded from above experiments that it might be difficult to image Hsp90 activity with GM derivatives due to its hyperlipophicity as reported by Su *et al.* (Eur J Nucl Med Mol Imaging. 2008; 35:1089-99). Consequently, we pursued indirect imaging of Hsp90 activity with ^{64}Cu-labeled EGFR antibody instead of GM derivatives.

PART II. Non-invasive PET imaging of EGFR degradation induced by a heat shock protein 90 inhibitor

After being treated with Hsp90 inhibitor, the downstream client proteins such as EGFR, HER2 would be downregulated. However, HER-2 expression is typically low in tumors except for breast and ovarian tumors, in which HER-2 imaging has only limited applications. PC-3 cells had low HER-2 expression and 17-AAG treatment induced only minimal HER-2 degradation. Thus, we chose to image EGFR degradation with ^{64}Cu labeled cetuximab (Erbitux; C255; ImClone and Bristol-Myers Squibb), a mouse–human chimeric IgG_1 mAb that binds with high affinity to EGFR.

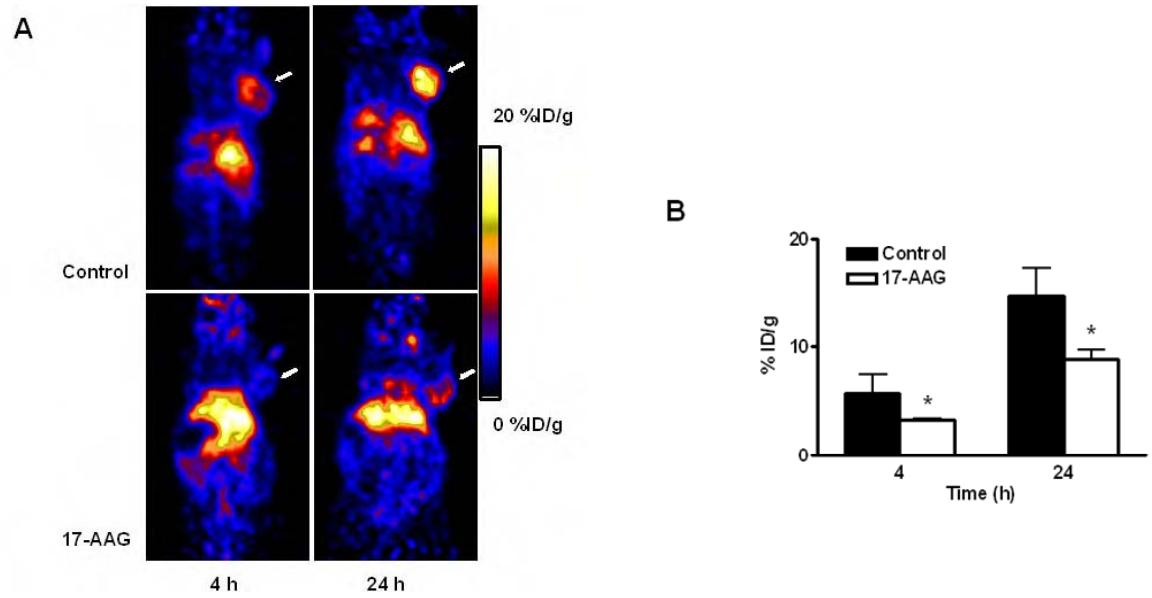

Fig. 4. (**A)** MicroPET images of PC-3 tumor-bearing nude mice at 4 h and 24 h after intravenous injection of ^{64}Cu-DOTA-cetuximab with or without 17-AAG treatment (n = 4/group). Decay-corrected whole-body coronal images that contain the tumor were shown and the tumors are indicated by white arrows. **(B)** PC-3 tumor uptake of ^{64}Cu-DOTA-cetuximab as quantified from microPET scans (n = 4/group). *, $P < 0.05$.

^{64}Cu-DOTA-cetuximab was determined to have 21.5 ± 2.2 DOTA residues per cetuximab and control human IgG_1 had 24.08 ±0.42 DOTA residues (n = 4). The specific activity of ^{64}Cu-DOTA-cetuximab was 1.24 ± 0.13 GBq/mg mAb and the radiolabeling yield was 84.0 ± 8.7% (n = 5). There was minimal reduction in the immunoreactivity of cetuximab after DOTA conjugation. After being treated with 17-AAG for 24 h, the PC-3 tumor uptake of ^{64}Cu-DOTA-cetuximab was much lower in both early and late time points as compared with the untreated group **(Fig. 4A)**. In untreated mice, the PC-3 tumor uptake of ^{64}Cu-DOTA-cetuximab was 5.8 ± 1.7 %ID/g and 14.6 ± 2.6 %ID/g at 4 and 24 h p.i., respectively. The uptake in 17-AAG treated tumors was significantly lower, 3.3 ± 0.3 %ID/g and 8.9 ± 1.6 %ID/g at 4 and 24 h p.i. respectively ($P < 0.05$ at both time points; n = 4) **(Fig. 4B)**. There were no significant differences of ^{64}Cu-DOTA-cetuximab uptake in other major organs between the 17-AAG treated group and untreated animals.

After microPET imaging at 24 h p.i., the animals were sacrificed for biodistribution studies and the results were shown in Fig. 5. The untreated PC-3 tumor had a high tracer uptake of 17.6 ± 5.3 %ID/g, consistent with the non-invasive microPET imaging results. After 17-AAG treatment, the uptake decreased significantly ($P < 0.05$) to 10.1 ± 0.7 %ID/g. The liver also had prominent radioactivity accumulation, with an uptake of 17.1 ± 4.2 %ID/g at 24 h p.i., due to both the hepatic clearance of antibody-based tracer and possible trans-chelation. Blood activity concentration was 7.9 ± 3.1 %ID/g at 24 h p.i., indicating the long circulation life time of the antibody. Compared with ^{64}Cu-DOTA-cetuximab, ^{64}Cu-DOTA-IgG$_1$ has a higher blood concentration (14.3 ± 2.4 %ID/g) and lower liver uptake (7.4 ± 1.8 %ID/g). The non-specific accumulation of ^{64}Cu-DOTA-IgG$_1$ in the PC-3 tumor (due to the leaky vasculature and lack of lymphatic drainage in the tumor) was very low (4.3 ± 0.5 %ID/g at 24 h p.i.; $P < 0.01$ compared with the control), confirming the EGFR specificity of ^{64}Cu-DOTA-cetuximab uptake in the PC-3 tumor.

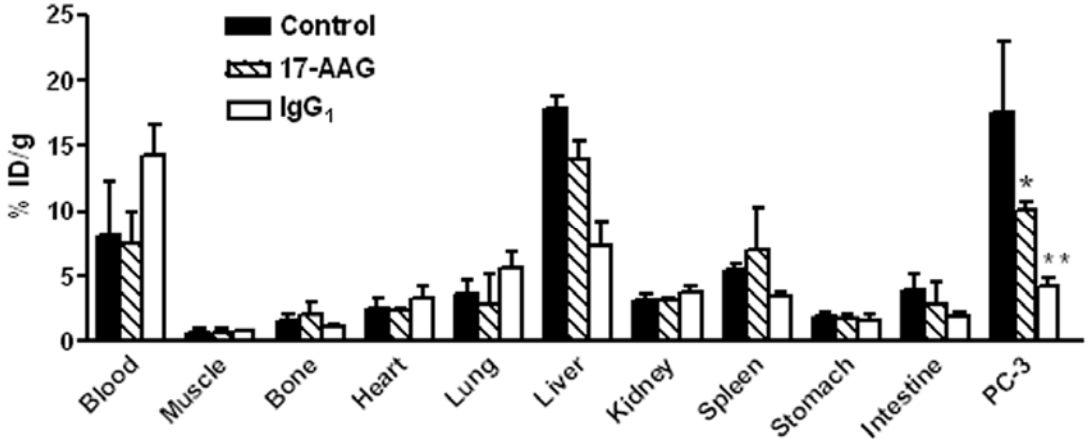

Fig. 5. Biodistribution of ^{64}Cu-DOTA-cetuximab (with or without 17-AAG treatment) and ^{64}Cu-DOTA-IgG$_1$ in PC-3 tumor-bearing mice at 24 h post-injection (n = 4 for each group). *, $P < 0.05$; **, $P < 0.01$.

To further confirm that 17-AAG induces EGFR degradation in vivo, we performed immunofluorescence staining using cetuximab as the primary antibody and Cy3-conjugated donkey anti-human IgG as the secondary antibody. Images were taken under the same condition and displayed at the same scale to make sure that the relative brightness observed in the images reflected the difference in EGFR expression level. In the untreated PC-3 tumor, EGFR expression was very high as indicated by the strong pseudo-colored red signal in the tissue (Fig. 6A). After treated with 17-AAG, EGFR expression was apparently lower with a much weaker fluorescence signal. Western blot of the tumor tissue lysate using cetuximab as the primary antibody also revealed that EGFR expression level in the PC-3 tumor decreased dramatically upon 17-AAG treatment (Fig. 6B). Taken together, biodistribution studies, immunofluorescence staining, and Western blot all confirmed that the decrease in tumor EGFR expression level upon 17-AAG treatment can be non-invasively monitored by ^{64}Cu-DOTA-cetuximab PET.

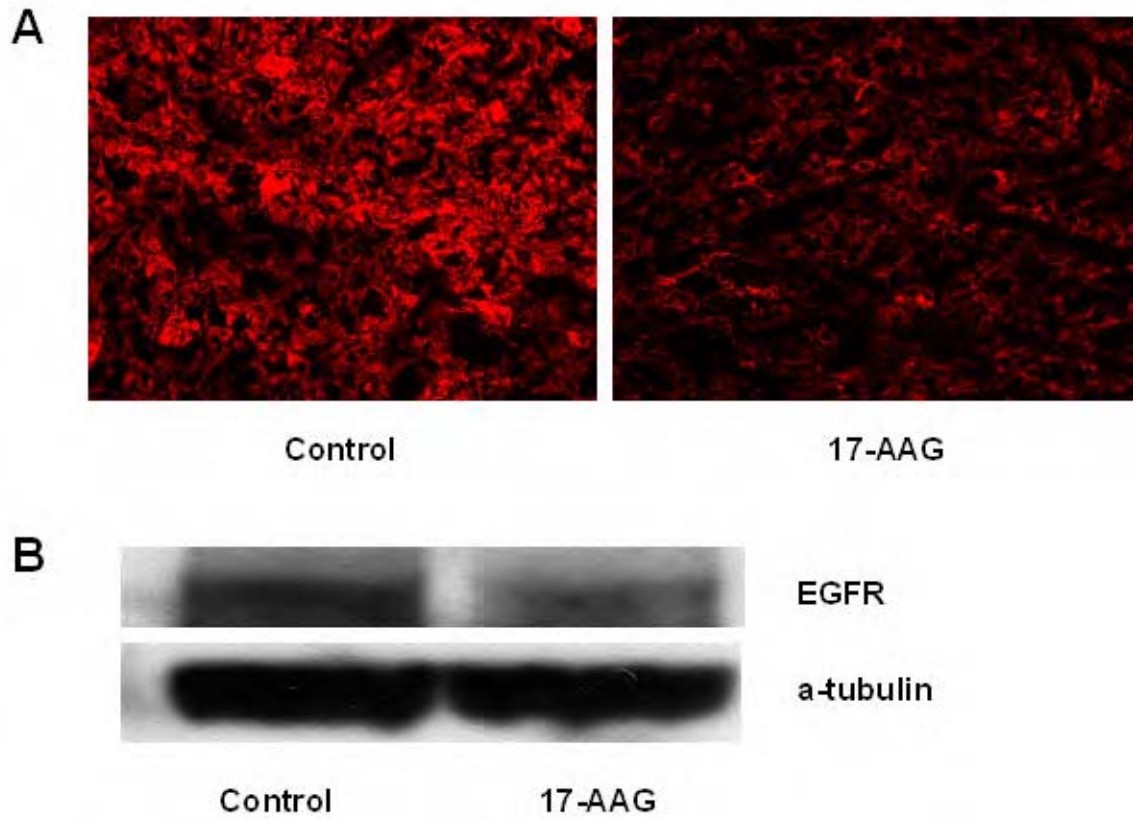

Fig. 6 (A) Immunofluorescence staining of EGFR in 17-AAG treated and untreated PC-3 tumor tissues. Images were obtained under the same conditions and displayed at the same magnification and scale (200×) **(B)** Western blot of EGFR in PC-3 tumors treated or untreated with 17-AAG. Cetuximab was used as the primary mAb.

KEY RESEARCH ACCOMPLISHMENTS

- Developed small molecular Hsp90 inhibitor, GM derivatives, to be used as imaging probes to monitor Hsp90 activity.
- Tested the feasibility of ^{64}Cu-labeled EGFR antibody to image EGFR expression with PET imaging
- Determined that ^{64}Cu-DOTA-cetuximab PET can be used to monitor the early response of EGFR degradation upon anti-Hsp90 therapy by 17-AAG.
- Summarized important applications of molecular imaging for HSPs, mainly HSP70 and HSP90.
- Expanded Hsp90 related imaging to other tumor types

REPOERABLE OUTCOMES

1. **Niu G**, Li ZB, Cao Q, Chen X. Monitor Therapeutic Response of Human Ovarian Cancer to 17-DMAG by Non-invasive PET imaging with ^{64}Cu-Trastuzumab. *Eur J Nucl Med Mol Imaging*, 2009 36(9):1510-1519.
2. **Niu G**, Chen X. PET Imaging of Angiogenesis. *PET Clinics*, 2009 4 (1): 17-38.
3. **Niu G**, Li ZB, Xie J, Le T, Chen X. Imaging Antibody Delivery with microPET in EGFR Positive Head-neck Squamous Cell Carcinoma Models. *J Nucl Med*, 2009 50(7):1116-1123.
4. **Niu G**, Chen X. Has Molecular and Cellular Imaging Enhanced Drug Discovery. *Drugs R&D*. 2008 9(6):351-368.
5. **Niu G** and Chen X. From Protein-Protein Interaction to Therapy Response: Molecular Imaging of Heat Shock Proteins. *Eur J Radiol*, 2009 70(2): 294-304.
6. **Niu G**, Cai W, Chen K, Chen X. Non-Invasive PET Imaging of EGFR Degradation Induced by a Heat Shock Protein 90 Inhibitor. *Mol Imaging Biol*, 2008 10(2):99-106.

In all publications, DOD PRCP was credited and the articles were appended.

CONCLUSIONS

Small molecular Hsp90 inhibitors, at least GM derivatives, showed reasonable tumor accumulation after being labeled with ^{64}Cu. However, in vitro experiments revealed that the GM derivatives are insufficient to tell the changes of both Hsp90 level and activity after stimulation. It might be more appropriate to use GM imaging for tumor detection instead of Hsp90 activity monitoring.

Hsp90 activity can be evaluated indirectly by imaging one or several of its downstream client proteins. The quantitative PET imaging of EGFR expression with ^{64}Cu-DOTA-cetuximab is successful for monitoring the early therapeutic response upon 17-AAG treatment in a human prostate cancer PC-3 tumor model. The quantification of EGFR degradation upon 17-AAG treatment using PET imaging is consistent with other in vitro and ex vivo measurements. This strategy may be applied to monitor the therapeutic response in EGFR-positive cancer patients under 17-AAG treatment.

Apart from EGFR, HER2 is another important downstream client protein. With the similar strategy, we labeled anti-HER-2 antibody with positron emission radioisotopes and successfully visualized tumor response to another Hsp90 inhibitor 17-DMAG.

REFERENCES

None

APPENDICES

PET of EGFR Antibody Distribution in Head and Neck Squamous Cell Carcinoma Models

Gang Niu[1], Zibo Li[2], Jin Xie[1], Quynh-Thu Le[3], and Xiaoyuan Chen[1]

[1]Molecular Imaging Program at Stanford (MIPS), Department of Radiology and Bio-X Program, Stanford University School of Medicine, Stanford, California; [2]USC Molecular Imaging Center, Department of Radiology, Keck School of Medicine, Los Angeles, California; and [3]Department of Radiation Oncology, Stanford University School of Medicine, Stanford, California

Epidermal growth factor receptor (EGFR) is a well-characterized protooncogene that has been shown to promote tumor progression in solid cancers. Clinical results for EGFR targeting with specific monoclonal antibodies (mAbs) such as cetuximab and panitumumab are promising; however, most studies indicate that only a subgroup of patients receiving the mAbs benefit from the immunotherapy, independent of EGFR expression level. To understand the in vivo kinetics of antibody delivery and localization, we performed small-animal PET studies with ^{64}Cu-labeled panitumumab in xenografts derived from 3 cell lines of human head and neck squamous cell carcinoma (HNSCC). **Methods:** Nude mice bearing HNSCC tumors with different levels of EGFR expression were imaged with small-animal PET using ^{64}Cu-1,4,7,10-tetraazacyclododecane-N,N′,N″,N‴-tetraacetic acid (DOTA)-panitumumab. Antibody distribution in the tumors was confirmed by ex vivo immunostaining using panitumumab and fluorescein 5(6)-isothiocyanate (FITC) panitumumab. CD31 immunostaining and Evans blue assay were also performed to assess the tumor vascular density and permeability. **Results:** Among these 3 tumor models, UM-SCC-22B tumors with the lowest EGFR protein expression showed the highest ^{64}Cu-DOTA-panitumumab accumulation, whereas SQB20 tumors with the highest EGFR expression showed the lowest ^{64}Cu-DOTA-panitumumab accumulation. Ex vivo staining demonstrated that SQB20 cells still had extremely high EGFR expression after forming tumors in nude mice, indicating that the low uptake of ^{64}Cu-DOTA-panitumumab in SQB20 tumors was not due to the loss of EGFR expression. The results from CD31 immunostaining and Evans blue permeability assay suggest that the low vessel density, poor vascular permeability, and binding site barrier are likely responsible for the overall low tumor uptake of the highly EGFR-expressing SQB20 tumors. **Conclusion:** The results from this study provide a possible explanation for the lack of an observed correlation between therapeutic efficacy of cetuximab and panitumumab and EGFR expression level as determined by immunohistochemistry or fluorescent in situ hybridization and may shed new light on the complications of anti-EGFR mAb therapy for HNSCC and other malignancies.

Received Jan. 6, 2009; revision accepted Mar. 16, 2009.
For correspondence or reprints contact: Xiaoyuan Chen, Molecular Imaging Program at Stanford (MIPS), Department of Radiology and Bio-X Program, Stanford University School of Medicine, 1201 Welch Rd., P095, Stanford, CA 94305-5484.
E-mail: shawchen@stanford.edu
COPYRIGHT © 2009 by the Society of Nuclear Medicine, Inc.

Key Words: epidermal growth factor receptor (EGFR); monoclonal antibody (mAb); positron emission tomography (PET); head-neck squamous cell carcinoma (HNSCC); tumor binding barrier

J Nucl Med 2009; 50:1116–1123
DOI: 10.2967/jnumed.109.061820

The epidermal growth factor receptor (EGFR) is a well-characterized protooncogene that has been shown to promote tumor progression in several solid cancers (*1*). EGFR is a member of the structurally related erbB family of receptor tyrosine kinases (*2*). It has been reported that more than 95% of head and neck squamous cell carcinomas (HNSCCs) express elevated EGFR levels, compared with the levels in normal mucosa (*3*). Further investigations show that the elevated EGFR expression is an independent indicator of poor prognosis and reduced survival in HNSCC patients (*4*). EGFR-targeted therapies include monoclonal antibodies (mAbs) such as cetuximab (IMC-C225; ImClone Systems Inc.) and panitumumab (ABX-EGF; Amgen Inc.), which block the extracellular ligand-binding domain of the receptor and tyrosine kinase inhibitors that prevent activation of the cytoplasmic kinase portion. These targeting approaches have shown great promise in preclinical studies (*5,6*). In patients with locoregionally advanced HNSCC, the combination of cetuximab and high-dose radiation was found to yield survival superior to that of radiation alone (*7*). Similarly, the addition of cetuximab to chemotherapy resulted in significantly longer median survival when compared with chemotherapy alone in patients with recurrent or metastatic HNSCC in a large randomized study (*8*).

Even though clinical results for EGFR targeting with specific antibodies are promising, most studies indicate that only a subgroup of patients receiving the mAbs benefit from them (*9,10*). To date, there is no known marker that can be used consistently to identify patients who would likely benefit from cetuximab therapy (*11*). No correlation has been found between the efficacy of cetuximab and EGFR tumoral staining intensity by immunohistochemistry (*11,12*). In addition, a response to cetuximab has been observed in

patients with EGFR-negative tumors (*13*). Although it has been reported that the EGFR gene copy number may predict the response to cetuximab, there are concerns about the reproducibility of such an assay (*14*). Most recently, KRAS mutations have been shown to be markers of resistance to anti-EGFR antibody in colorectal cancer; however, such a mutation is rare in HNSCC (*15*). Because EGFR antibody treatment is rather expensive and not without associated toxicity, a reliable marker would be quite helpful in the management of HNSCC patients.

It has been demonstrated that noninvasive molecular imaging can provide additional diagnostic information to improve patient management (*16,17*). Such an imaging approach has also been applied to EGFR using SPECT with ^{111}In and ^{99m}Tc-labeled EGFR-specific antibodies (*18–20*). PET of EGFR has also been performed with cetuximab conjugated to a bifunctional chelator such as 1,4,7,10-tetraazacyclododecane-*N,N′,N″,N‴*-tetraacetic acid (DOTA) and labeled with ^{64}Cu (*21,22*). Small-animal PET showed that uptake of ^{64}Cu-DOTA-cetuximab increased over time in EGFR-positive tumors but was relatively low in EGFR-negative tumors (*23*). ^{64}Cu-DOTA-cetuximab has also been used to detect and quantify EGFR expression in cervical cancer tumors (*21*).

To fully understand the issue of antibody delivery in HNSCC and shed some light on the seemingly contradictory observation of EGFR expression and antibody therapeutic efficacy, we labeled panitumumab, a fully humanized mAb against EGFR (*24*), with ^{64}Cu and performed quantitative PET studies on different HNSCC tumor xenografts. We found that the in vivo uptake of labeled panitumumab in tumors failed to correlate with EGFR protein expression levels in HNSCC xenograft models.

MATERIALS AND METHODS

All commercially available chemical reagents were used without further purification. DOTA was purchased from Macrocyclics, Inc., and Chelex 100 resin (50–100 mesh) was purchased from Sigma-Aldrich. Water and all buffers were passed though a Chelex 100 column (1 × 15 cm) before use in radiolabeling procedures to ensure that the aqueous buffer was free of heavy metals. PD-10 desalting columns were purchased from GE Healthcare. Athymic nude mice were obtained from Harlan at 4–6 wk of age. ^{64}Cu was ordered from the University of Wisconsin–Madison. The human HNSCC cell lines SQB20, SAS, and UM-SCC-22B were obtained, respectively, from Dr. J. Martin Brown's laboratory at Stanford University; from the Cell Resource Center for the Biomedical Research Institute of Development, Aging, and Cancer, Tohoku University; and from the University of Michigan. The cell lines were maintained in DMEM medium supplemented with 10% fetal bovine serum, 1% glutamine, 100 U of penicillin per milliliter, and 100 μg of streptomycin per milliliter (Invitrogen).

Antibody Labeling

Fluorescein 5(6)-isothiocyanate (FITC), purchased from Sigma-Aldrich, was dissolved in anhydrous dimethyl sulfoxide immediately before use and then added to panitumumab with a ratio of 50 μg per mg of antibody. The mixture was incubated and rotated at room temperature for 60 min for covalent conjugation. The unreacted FITC was removed by PD-10 column. FITC-to-antibody ratio and antibody concentration were determined by the following equation after measuring the absorbance at 280 and 495 nm: antibody (mg/mL) = $[A_{280} - 0.31 \times A_{495}]/1.4$; FITC-to-antibody ratio = $3.1 \times A_{495}/(A_{280} - 0.31 \times A_{495})$. The FITC-to-antibody ratio is 10.13 for FITC-panitumumab.

Detailed procedures for DOTA conjugation and for measurement of DOTA number have been reported earlier (*23,25*). The reaction ratio of DOTA to antibody is 200:1. $^{64}CuCl_2$ (74 MBq) was diluted in 300 μL of 0.1 M sodium acetate buffer (pH 6.5) and added to 50 μg of DOTA-panitumumab. The reaction mixture was incubated for 1 h at 40°C with constant shaking. ^{64}Cu-DOTA-panitumumab was then purified by PD-10 column using phosphate-buffered saline (PBS) as the mobile phase. The labeling yield was calculated by dividing the decay-corrected radioactivity of ^{64}Cu-DOTA-panitumumab by the total radioactivity used for reaction.

Flow Cytometry

HNSCC cells were harvested and washed with PBS containing 0.5% bovine serum albumin. On blockade by 2% bovine serum albumin in PBS, the cells were incubated with panitumumab (10 μg/mL in PBS containing 2% bovine serum albumin). FITC-conjugated donkey antihuman IgG (1:200) was then added and allowed to incubate for 1 h at room temperature. After washing, the cells were analyzed using an LSR flow cytometer (Beckman Coulter). The FITC signal intensity was analyzed using CellQuest software (version 3.3; Becton-Dickinson).

Tumor Models

All animal experiments were performed under a protocol approved by the Stanford University Administrative Panel on Laboratory Animal Care. Subcutaneous HNSCC tumor models were established in 4- to 6-wk-old female athymic nude mice. Typically, 5×10^6 cells suspended in 50 μL of PBS were injected and the mice underwent PET when the tumor volume reached 200–400 mm^3 (3–4 wk after inoculation).

PET and Image Analysis

PET of tumor-bearing mice was performed on a microPET R4 rodent model scanner (Siemens Medical Solutions) as described earlier (*23*). The mice were intravenously injected with ^{64}Cu-DOTA-panitumumab or ^{64}Cu-DOTA-IgG (Jackson ImmunoResearch Laboratories) (7–8 MBq/6 μg/mouse), and static scans were acquired at 4, 20, 30, and 48 h after injection. For each scan, 3-dimensional regions of interest were drawn over the tumor, liver, heart, and muscle on decay-corrected whole-body coronal images. The average radioactivity concentration within a tumor or an organ was obtained from mean pixel values within the region-of-interest volume. These mean values were converted to counts/mL/min using a conversion factor. Assuming a tissue density of 1 g/mL, the counts/mL/min were converted to counts/g/min and then divided by the injected dose to obtain an imaging region-of-interest–derived percentage injected dose (%ID)/g.

Measurement of Vascular Permeability Using Evans Blue

The effective microvascular permeability of albumin–Evans blue was determined using the simplified indicator diffusion method (*26*). Evans blue (Sigma-Aldrich) was administered intravenously at a dose of 30 mg/kg. The mice were reperfused at an elevated perfusion pressure with physiologic saline immediately before

tumor excision to remove albumin–Evans blue from the tumor circulation. Tumors were excised 4 h after the dye had been injected and were cut into pieces weighing approximately 50 mg to facilitate the extraction of Evans blue. The pieces were pooled in a tube and weighed before Evans blue was extracted in formamide (0.01 mL/mg of tumor tissue) for 72 h. Relative Evans blue concentrations were determined by measuring the light absorbance at 620 nm. For Evans blue fluorescence staining, tumors were harvested and sectioned at 4 h after dye injection. After being mounted with medium containing 4,6-diamino-2-phenylindole (DAPI), the sections were observed under an LSM 510 confocal microscope (Zeiss) with optical filters (543-nm excitation; long pass, 585-nm emission).

Immunofluorescence Staining

Frozen HNSCC tumor sections (5 μm thick) were warmed to room temperature, fixed with ice-cold acetone for 10 min, and dried in the air for 30 min. The sections were rinsed in PBS for 2 min and blocked in 10% donkey serum for 1 h at room temperature. The sections were incubated with panitumumab (10 μg/mL) for 1 h at room temperature and visualized with FITC-conjugated donkey antihuman secondary antibody (1:200, Jackson ImmunoResearch Laboratories) under a microscope (Axiovert 200 M; Carl Zeiss USA). Images were acquired under the same conditions and displayed at the same scale.

For in vivo staining, 100 μg of DOTA-panitumumab or FITC-panitumumab were injected by tail vein. The animals were sacrificed 30 h after injection, and the tumor samples were collected. The tumor sections with DOTA-panitumumab were fixed and stained using a similar procedure except that no primary antibody was added. The tumor sections with FITC-panitumumab were mounted with DAPI-containing mounting medium and were observed directly without any further staining.

CD31 Staining and Microvascular Density Measurement

Frozen slices (5 μm thick) of HNSCC tumor were fixed with cold acetone for 10 min and dried in the air for 30 min. The slices were rinsed with PBS for 2 min and blocked with 10% donkey serum for 30 min at room temperature. The slices were then incubated with panitumumab and rat antimouse CD31 antibody for 1 h at room temperature and visualized using FITC-conjugated donkey antihuman secondary antibody (1:200; Jackson ImmunoResearch Laboratories, Inc.) and Cy3-conjugated rat antimouse IgG (1:200; Jackson ImmunoResearch Laboratories, Inc.).

After CD31 staining, 10 random views in both the center and the periphery of the tumor slices were selected for microvessel density (MVD) analysis using an observer-set threshold to distinguish vascular elements from surrounding tissue parenchyma. The vessel that contained branching points was counted as a single vessel. The number of vessels counted was divided by the field of view to yield the MVD, as vessels/mm^2.

Statistical Analysis

Quantitative data were expressed as mean ± SD. Means were compared using 1-way ANOVA and the Student t test. P values less than 0.05 were considered statistically significant.

RESULTS

High Expression of EGFR in HNSCC Cell Lines

We selected 3 different HNSCC cell lines and analyzed their EGFR expression levels by FACS (Fig. 1). All 3 cell lines showed relatively high EGFR expression, in the order of SQB20 > SAS > UM-SCC-22B. Immunostaining of tumor sections derived from these cell lines also showed extremely high EGFR expression in SQB20 tumors, high expression in SAS tumors, and relatively low expression in UM-SCC-22B tumors.

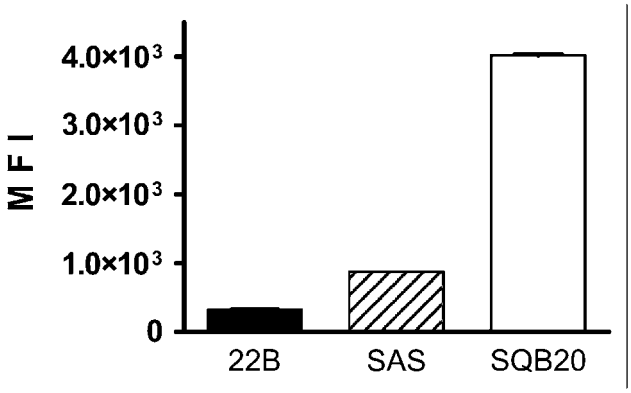

FIGURE 1. Flow cytometric analysis of EGFR expression on HNSCC cells. Panitumumab was used as primary antibody, and FITC-conjugated donkey antihuman IgG was used as secondary antibody. Mean values (±SD) of FITC signal intensity (MFI) of 3 measurements are shown. 22B = UM-SCC-22B.

PET of EGFR Expression

The specific activity of ^{64}Cu-DOTA-panitumumab was 1.35 ± 0.26 GBq/mg, and the radiolabeling yield was 85.0% ± 9.2% (n = 5). The decay-corrected whole-body transaxial images containing the tumors are shown in Figure 2. At all time points, the accumulation of ^{64}Cu-DOTA-panitumumab was highest in UM-SCC-22B tumors, lowest in SQB20 tumors, and moderate in SAS tumors. Quantitative data based on region-of-interest analysis are shown in Table 1. At 30 h after injection, the UM-SCC-22B tumor uptake of ^{64}Cu-DOTA-panitumumab was 31.42 ± 10.77 %ID/g, SAS tumor uptake was 12.39 ± 4.15 %ID/g, and SQB20 tumor uptake was 8.76 ± 1.07 %ID/g. The liver also had prominent radioactivity accumulation, with an uptake of 11.96 ± 3.87 %ID/g at 30 h after injection, due to both the hepatic clearance of antibody-based tracer and possible transchelation. The blood activity concentration was 12.35 ± 4.25 %ID/g at 30 h after injection, indicating the long circulation life of the antibody.

We also imaged these HNSCC tumors with ^{64}Cu-DOTA-IgG to eliminate the influence of passive targeting for PET quantification. Compared with ^{64}Cu-DOTA-panitumumab, ^{64}Cu-DOTA-IgG had a similar blood concentration (13.01 ± 1.28 %ID/g at 30 h) and liver uptake (10.92 ± 1.77 %ID/g at 30 h). The tumor uptake of ^{64}Cu-DOTA-IgG was low in all 3 tumor models. After IgG subtraction, UM-SCC-22B still showed the highest absolute uptake (14.14 ± 3.89 %ID/g), whereas SQB20 showed the lowest absolute uptake (2.85 ± 0.82 %ID/g) (Fig. 2B).

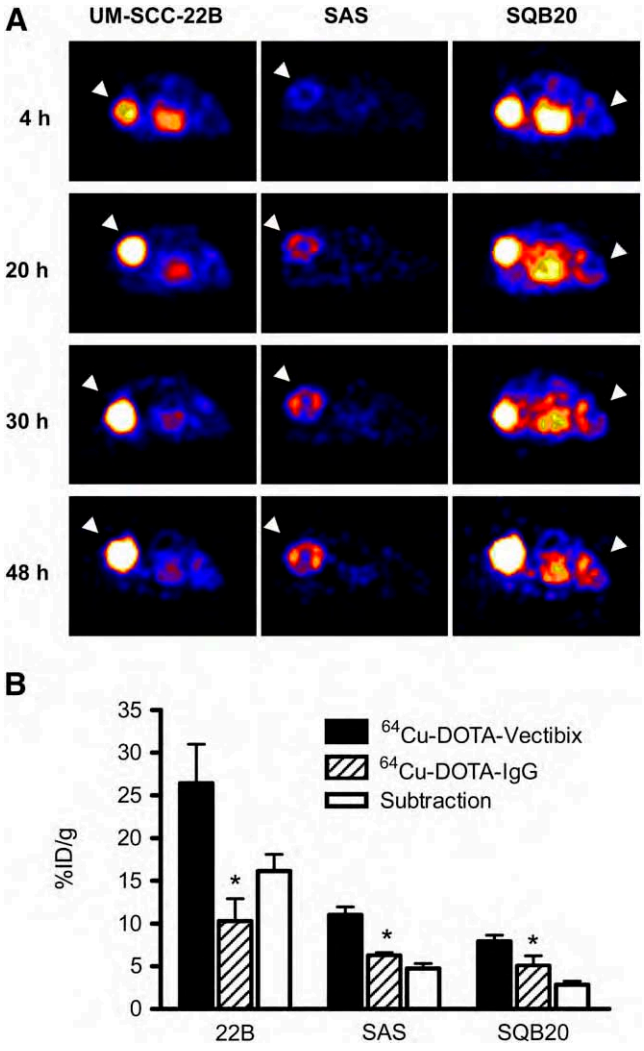

FIGURE 2. (A) Small-animal PET images of HNSCC tumor-bearing nude mice at different time points after intravenous injection of ^{64}Cu-DOTA-panitumumab (n = 4/group). Decay-corrected transaxial images at different time points are shown, and tumors are indicated by arrowheads. For UM-SCC-22B and SAS tumors, scale ranged from 0 %ID/g to 30 %ID/g, and for SQB20 tumors, scale ranged from 0 %ID to 15 %ID/g for optimal visualization. (B) HNSCC tumor uptake levels of ^{64}Cu-DOTA-panitumumab and ^{64}Cu-DOTA-IgG at 20 h after injection quantified from small-animal PET scans (n = 4). 22B = UM-SCC-22B. *$P < 0.05$.

Panitumumab Distribution in HNSCC Tumors

The PET data showed that uptake of ^{64}Cu-DOTA-panitumumab was highest in the UM-SCC-22B tumors that had the lowest EGFR protein expression. Inversely, the radioactivity accumulation was lowest in the SQB20 tumors that had the highest EGFR expression. To further explain this seemingly abnormal phenomenon, we conjugated panitumumab with a fluorescent dye FITC and harvested tumors at 30 h after intravenous injection of FITC-panitumumab. After being coated with a mounting medium containing DAPI, the tumor sections were examined under a fluorescence microscope and images were taken and displayed under the same conditions to make sure that the fluorescence intensity represented the FITC-panitumumab level. As shown in Figure 3B, for SQB20 tumors, FITC-panitumumab was primarily detected within several cell diameters of the blood vessels with high fluorescence density; for SAS tumors, the fluorescence signal was also limited to perivascular regions with a longer diffusive distance. In contrast, the fluorescence signal diffused much more homogeneously in UM-SCC-22B tumors. DOTA-panitumumab showed an intratumoral distribution similar to that of FITC-panitumumab. Costaining with CD31 further demonstrated the limited perivascular localization of panitumumab in both SQB20 and SAS tumors (Fig. 3C and 3D). These results indicate that the poor penetration of the antibody through perivascular tissues is at least partially responsible for the low accumulation of ^{64}Cu-DOTA-panitumumab in SQB20 tumors.

Vascular Density and Permeability of HNSCC Tumors

Vascular density is another determining factor for antibody diffusion and binding. The microvascular density (MVD) of HNSCC tumors was determined with CD31-stained tumor sections. UM-SCC-22B tumors are highly vascularized, with an MVD of 27.1/mm^2. SQB20 tumors have the lowest MVD, 4.7/mm^2, and SAS tumors have an intermediate MVD of 12.5/mm^2 (Fig. 4). The morphology of the vasculature also varied among these 3 tumor models.

Evans blue forms a complex with albumin in vivo by electrostatic interaction between the sulfonic acid group of the dye and the ε-amine groups of the lysine residues of albumin. The strong binding makes the behavior of Evans blue reflect the transport of albumin, which is about 67 kDa with a diameter of about 7 nm (*26*). As shown in Figure 5A, the tumor vasculature was visualized through the high-fluorescence signal of Evans blue, as is consistent with CD31 staining. In UM-SCC-22B tumors, moreover, the interstitial diffusion of Evans blue albumin from vessels can be identified. The quantification of Evan blue perfusion showed that UM-SCC-22B tumors were the most permeable among the 3 HNSCC tumor models, whereas SAS tumors were less permeable and SQB20 tumors were the least permeable (Fig. 5B).

DISCUSSION

In this study, we conjugated an EGFR-specific antibody, panitumumab, with DOTA and labeled the conjugate with ^{64}Cu. Small-animal PET was performed to evaluate EGFR expression in tumor models derived from 3 HNSCC cell lines with different levels of EGFR expression. We found no correlation between PET quantification and EGFR protein expression level. To our surprise, UM-SCC-22B tumors, which had the lowest EGFR protein expression, showed the highest accumulation of ^{64}Cu-DOTA-panitumumab accumulation whereas SQB20 tumors, with the highest EGFR expression, showed the lowest accumulation of ^{64}Cu-DOTA-panitumumab. The low uptake of ^{64}Cu-DOTA-panitumumab

TABLE 1. Biodistribution of ^{64}Cu Activity in HNSCC Tumor Models

	^{64}Cu-DOTA-panitumumab (%ID/g)				^{64}Cu-DOTA-IgG (%ID/g)			
Site	4 h	20 h	30 h	48 h	4 h	20 h	30 h	48 h
Blood	22.73 ± 3.99	14.42 ± 4.47	12.35 ± 4.25	10.29 ± 4.04	20.54 ± 2.58	13.84 ± 2.24	13.01 ± 1.28	11.49 ± 1.99
Liver	15.94 ± 3.35	12.52 ± 3.29	11.96 ± 3.87	11.55 ± 3.64	13.77 ± 2.04	10.42 ± 1.17	10.92 ± 1.77	10.83 ± 2.25
Muscle	3.32 ± 1.50	2.479 ± 1.08	2.79 ± 1.31	2.14 ± 1.03	2.63 ± 0.78	2.20 ± 0.40	2.72 ± 0.83	2.10 ± 0.11
22B	16.09 ± 6.52	26.41 ± 9.16	31.42 ± 10.77	34.80 ± 9.26	5.70 ± 3.92	10.27 ± 5.27	11.75 ± 6.35	12.14 ± 6.71
SAS	6.39 ± 1.60*	11.01 ± 1.84*	12.39 ± 4.15*	15.35 ± 3.33*	3.51 ± 0.86	6.26 ± 0.68	7.20 ± 2.25	8.05 ± 3.75
SQB20	4.02 ± 1.87†	7.92 ± 1.48†	8.76 ± 1.07†	9.39 ± 1.44†	3.54 ± 1.04	5.07 ± 2.30	7.26 ± 5.15	8.57 ± 5.04

*$P < 0.05$.
†$P < 0.01$.
22B = UM-SCC-22B.
Data are %ID/g and represent mean ± SD of 4 mice.

in SQB20 tumors was not due to the loss of EGFR expression. On the contrary, ex vivo staining using panitumumab as the primary antibody demonstrated that SQB20 cells still had extremely high EGFR expression after forming tumors in nude mice. These results indicated that the expression level of EGFR cellular protein correlated poorly with the efficiency of antibody delivery to the tumors. Similar findings have also been reported for ^{111}In-conjugated anti-EGFR antibody in breast cancer models (*20*).

At present, antibodies are indisputably the best-established class of binding molecules for tumor diagnosis and therapy (*27,28*). Tumor antigen density is known to influence antibody-based tumor targeting (*29*). The expression level of EGFR in all 3 HNSCC cell lines tested was quite high compared with the other solid tumors. We have previously performed PET with ^{64}Cu-DOTA-cetuximab on another 7 different solid tumor models, including U87MG human glioblastoma; PC-3 human prostate carci-

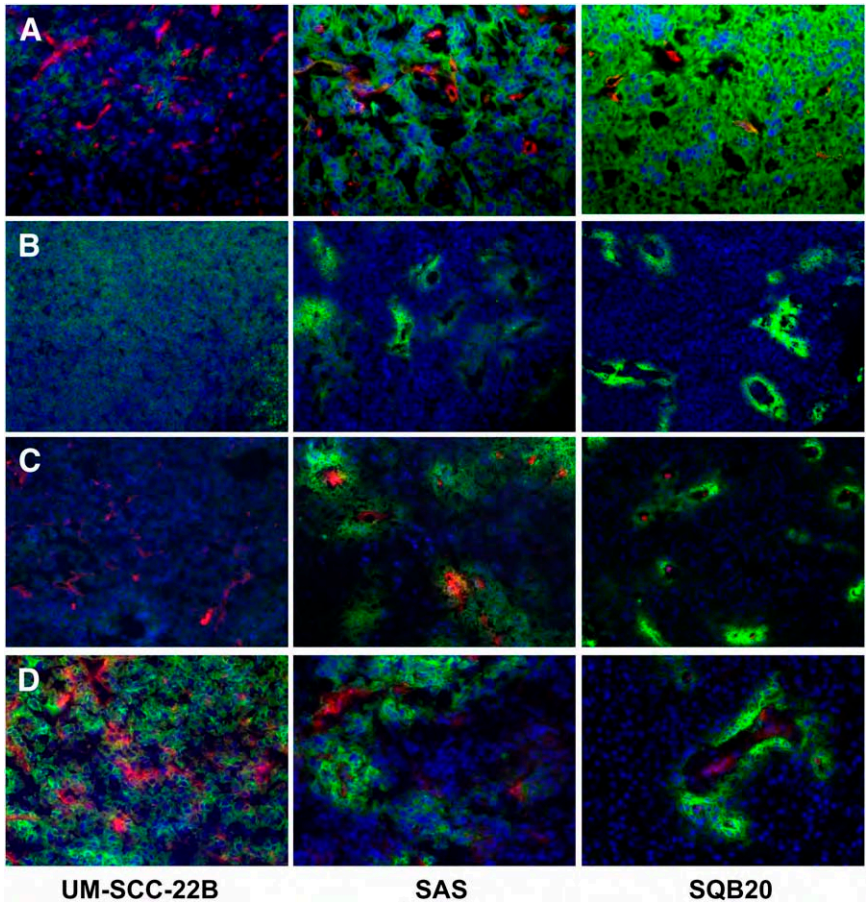

FIGURE 3. Immunofluorescence examination of EGFR expression and panitumumab localization in HNSCC tumors. Images were obtained under same conditions and displayed at same magnification and scale (except D). (A) Tumor sections were directly stained with panitumumab as primary antibody and with FITC-conjugated donkey antihuman IgG as secondary antibody. Murine CD31 was stained with Cy3-conjugated IgG to visualize tumor vasculature. SQB20 tumors showed highest fluorescence intensity, corresponding to highest EGFR expression. (B) Thirty hours after FITC-panitumumab injection, tumors were harvested and tumor sections were observed after being mounted with DAPI-containing medium. (C) Thirty hours after DOTA-panitumumab injection, tumors were harvested and tumor sections were stained with FITC-conjugated donkey antihuman IgG. (D) In high-magnification view of images shown in C, color was rescaled to emphasize relationship of panitumumab and vasculature (red from Cy3 for CD31; green from FITC for EGFR and panitumumab; blue from DAPI for nucleus visualization).

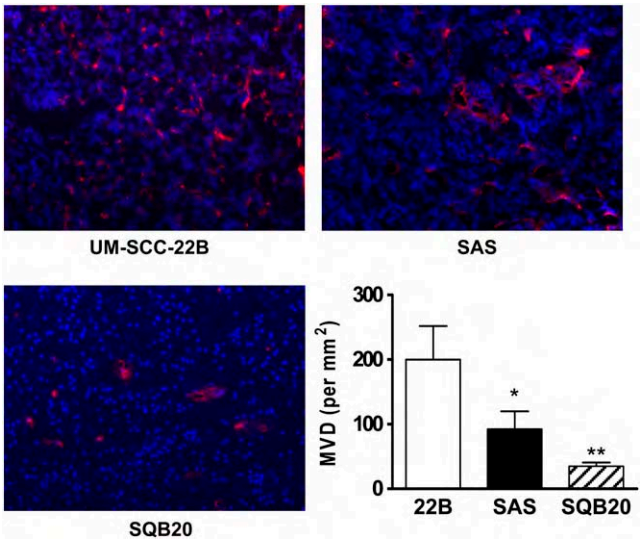

FIGURE 4. MVD measurement of HNSCC tumors. Frozen slices of HNSCC tumor were stained with rat antimouse CD31 antibody and visualized using Cy3-conjugated rat antimouse IgG. After CD31 staining, 10 random views in both center and periphery of tumor slices were selected for MVD analysis using observer-set threshold to distinguish vascular elements from surrounding tissue parenchyma. Number of vessels counted was divided by field of view to yield MVD, as number of vessels/mm^2. 22B = UM-SCC-22B. *$P < 0.05$. *$P < 0.05$. **$P < 0.01$.

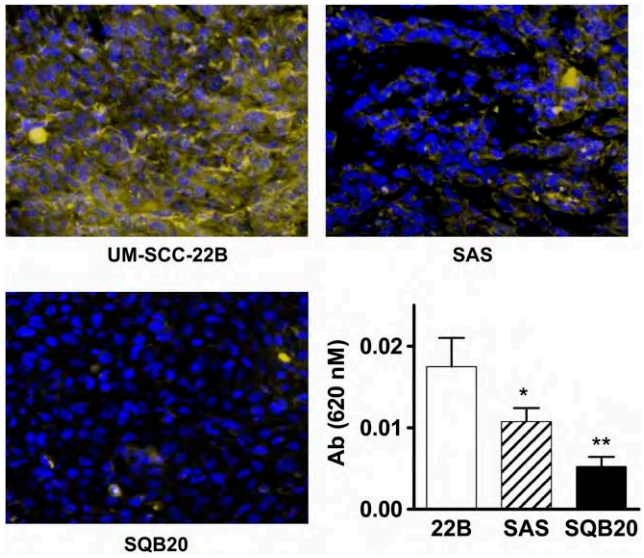

FIGURE 5. Measurement of vascular permeability using Evans blue. Tumors were excised 4 h after dye had been injected. After being mounted with medium containing DAPI, sections were observed under LSM 510 (Zeiss) confocal microscope with optical filters (543-nm excitation; long pass, 585-nm emission). For quantification, Evans blue was extracted in formamide (0.01 mL/mg of tumor tissue) for 72 h. Relative Evans blue concentrations were determined by measuring light absorbance at 620 nm. 22B = UM-SCC-22B. *$P < 0.05$. **$P < 0.01$.

noma; CT-26 murine colorectal carcinoma; HCT-8, HCT-116, and SW620 human colorectal carcinoma; and MDA-MB-435 human breast cancer (*23*). We found an increased accumulation of activity in EGFR-positive tumors over time but relatively low uptake in EGFR-negative tumors at all time points examined. Moreover, tracer uptake as measured by PET showed a good linear correlation with EGFR protein expression level as measured by Western blotting. Eiblmaier et al. (*21*) have also shown that EGFR messenger RNA expression corresponded directly to EGFR densities and levels of internalization of ^{64}Cu-DOTA-centuximab in 5 cervical cancer cell lines. When compared between the 3 HNSCC cell lines and these other cell lines, the levels of EGFR expression were similar between the lowest-expressing HNSCC cells (UM-SCC22B) and the highest-expressing non-HNSCC cells (PC-3 prostate cancer). We speculated that antigen density is a major determining factor in PET with radionuclide-labeled antibodies when antigen expression level is below a certain threshold. Such a threshold may have been exceeded in the HNSCCs tested here. With regard to antibody binding affinity, we have tested ^{64}Cu-DOTA-cetuximab in these 3 HNSCC models and the results were similar to those obtained with ^{64}Cu-DOTA-panitumumab, despite the fact that panitumumab has a higher affinity for EGFR than does cetuximab. Again, if antigen density exceeds a certain threshold, binding affinity may play a smaller role in antibody distribution.

Because of the lack of correlation between antigen density, binding affinity, and imaged antibody distribution, we surmised that low MVD and poor vascular permeability were mainly responsible for the observed imaging results. Compared with the other 2 HNSCC models, SQB20 tumors were poorly vascularized as indicated by CD31 staining. In addition, the vascular permeability of SQB20 tumors was the worst among the 3 tumor models, on the basis of Evans blue perfusion data. Apart from MVD and vascular permeability, we also speculated that there exists a binding-site barrier for ^{64}Cu-DOTA-panitumumab penetration in SQB20 tumors. The high-affinity binding of mAbs to the first encountered tumor antigen would retard antibody percolation (*30*), resulting in a more heterogeneous distribution. In the case of SQB20 tumors, the high number of EGFR receptors on the tumor cell surface may act as a barrier against distal diffusion of antibody. As shown in Figure 2, most panitumumab molecules were perivascular and diffused through a distance of only several cells. The implication is that the perivascular tumor cells depleted mAbs quickly and inhibited further penetration of panitumumab. The localization of panitumumab in SQB20 and UM-SCC-22B tumors is illustrated in Supplemental Figure 1 (supplemental materials are available online only at http://jnm.snmjournals.org). Because of the abundant blood supply, high MVD, and high blood vessel permeability, UM-SCC-22B tumors showed a noticeably higher accumulation of ^{64}Cu-DOTA-panitumumab than did the other 2 HNSCC tumor

models. Compared with a therapeutic dose of antibody (100–200 μg per mouse), the imaging dose was very low (~5 μg per mouse). The difference in antibody concentration should be considered when one is integrating imaging data into therapeutic scenarios, because images with low concentrations of antibody may exaggerate the influence of vascular density and permeability.

Under physiologic conditions, EGFR is internalized on ligand activation and ligand–receptor complexes are targeted for lysosomal degradation, resulting in signal attenuation (*31*). A similar phenomenon has been observed for EGFR binding antibody (*32*). ^{64}Cu-DOTA-cetuximab internalization was reported in cervical cancer cells and correlated well with EGFR expression, with approximately 25% of cell-surface EGFR being internalized after 4 h of incubation in all cell lines tested (*21*). We also evaluated panitumumab internalization in HNSCC cell lines and found that all HNSCC cells showed a similar internalization ratio of around 30% after 2 h of incubation at 37°C (Supplemental Fig. 2). Therefore, antibody internalization after panitumumab binding to EGFR was unlikely to have contributed to the differential distribution of ^{64}Cu-DOTA-panitumumab in HNSCC tumor models (*33*).

PET with radiolabeled antibody visualizes and quantifies several parameters, including tumor-specific binding, perfusion, vascularity, vascular permeability, and plasma half-life. Moreover, radiolabeled antibody PET provides more comprehensive information for patient screening and therapeutic guidance than does immunohistochemistry or fluorescent in situ hybridization—techniques that only sample antigen density in a small part of the tumor. The results from this study may provide a possible explanation for the lack of an observed correlation between therapeutic efficacy of cetuximab and panitumumab and EGFR expression level as determined by immunohistochemistry or fluorescent in situ hybridization (*34*). For tumors such as SQB20, even with high EGFR expression, the patchy and incomplete tumor perfusion could result in suboptimal therapeutic effects when therapeutic efficacy is dependent on uniform delivery to tumor cells (*30,35*). We are pursuing studies to determine whether the results of ^{64}Cu-DOTA-panitumumab or ^{64}Cu-DOTA-cetuximab imaging correlate with treatment efficacy when the same antibody is used alone or conjugated to a high-energy radioisotope for radioimmunotherapy.

CONCLUSION

The in vivo tumor uptake quantified from PET with ^{64}Cu-DOTA-panitumumab in HNSCC tumor models failed to reflect the expression level of EGFR in vivo. The results revealed a possible explanation for the lack of an observed correlation between therapeutic efficacy of cetuximab and panitumumab and EGFR expression level as determined by immunohistochemistry or fluorescent in situ hybridization. This study may shed new light on the complications of anti-EGFR mAb therapy for HNSCC and other malignancies.

ACKNOWLEDGMENTS

This project was supported in part by the National Cancer Institute (R21 CA102123, P50 CA114747, U54 CA119367, R24 CA93862, and R01 CA118582) and by a Department of Defense Prostate Cancer Postdoctoral Training Award.

REFERENCES

1. Salomon DS, Brandt R, Ciardiello F, Normanno N. Epidermal growth factor-related peptides and their receptors in human malignancies. *Crit Rev Oncol Hematol.* 1995;19:183–232.
2. Matheny KE, Barbieri CE, Sniezek JC, Arteaga CL, Pietenpol JA. Inhibition of epidermal growth factor receptor signaling decreases p63 expression in head and neck squamous carcinoma cells. *Laryngoscope.* 2003;113:936–939.
3. Grandis JR, Tweardy DJ. Elevated levels of transforming growth factor alpha and epidermal growth factor receptor messenger RNA are early markers of carcinogenesis in head and neck cancer. *Cancer Res.* 1993;53:3579–3584.
4. Grandis JR, Zeng Q, Drenning SD, Tweardy DJ. Normalization of EGFR mRNA levels following restoration of wild-type p53 in a head and neck squamous cell carcinoma cell line. *Int J Oncol.* 1998;13:375–378.
5. Heimberger AB, Learn CA, Archer GE, et al. Brain tumors in mice are susceptible to blockade of epidermal growth factor receptor (EGFR) with the oral, specific, EGFR-tyrosine kinase inhibitor ZD1839 (Iressa). *Clin Cancer Res.* 2002;8:3496–3502.
6. Luwor RB, Johns TG, Murone C, et al. Monoclonal antibody 806 inhibits the growth of tumor xenografts expressing either the de2-7 or amplified epidermal growth factor receptor (EGFR) but not wild-type EGFR. *Cancer Res.* 2001;61:5355–5361.
7. Bonner JA, Harari PM, Giralt J, et al. Radiotherapy plus cetuximab for squamous-cell carcinoma of the head and neck. *N Engl J Med.* 2006;354:567–578.
8. Vermorken JB, Mesia R, Rivera F, et al. Platinum-based chemotherapy plus cetuximab in head and neck cancer. *N Engl J Med.* 2008;359:1116–1127.
9. Folprecht G, Lutz MP, Schoffski P, et al. Cetuximab and irinotecan/5-fluorouracil/folinic acid is a safe combination for the first-line treatment of patients with epidermal growth factor receptor expressing metastatic colorectal carcinoma. *Ann Oncol.* 2006;17:450–456.
10. Cohenuram M, Saif MW. Panitumumab the first fully human monoclonal antibody: from the bench to the clinic. *Anticancer Drugs.* 2007;18:7–15.
11. Saltz LB, Meropol NJ, Loehrer PJ Sr, Needle MN, Kopit J, Mayer RJ. Phase II trial of cetuximab in patients with refractory colorectal cancer that expresses the epidermal growth factor receptor. *J Clin Oncol.* 2004;22:1201–1208.
12. Cunningham D, Humblet Y, Siena S, et al. Cetuximab monotherapy and cetuximab plus irinotecan in irinotecan-refractory metastatic colorectal cancer. *N Engl J Med.* 2004;351:337–345.
13. Chung KY, Shia J, Kemeny NE, et al. Cetuximab shows activity in colorectal cancer patients with tumors that do not express the epidermal growth factor receptor by immunohistochemistry. *J Clin Oncol.* 2005;23:1803–1810.
14. Moroni M, Veronese S, Benvenuti S, et al. Gene copy number for epidermal growth factor receptor (EGFR) and clinical response to antiEGFR treatment in colorectal cancer: a cohort study. *Lancet Oncol.* 2005;6:279–286.
15. Lievre A, Bachet JB, Boige V, et al. KRAS mutations as an independent prognostic factor in patients with advanced colorectal cancer treated with cetuximab. *J Clin Oncol.* 2008;26:374–379.
16. Adams GP, Schier R, McCall AM, et al. High affinity restricts the localization and tumor penetration of single-chain fv antibody molecules. *Cancer Res.* 2001;61:4750–4755.
17. Erjala K, Sundvall M, Junttila TT, et al. Signaling via ErbB2 and ErbB3 associates with resistance and epidermal growth factor receptor (EGFR) amplification with sensitivity to EGFR inhibitor gefitinib in head and neck squamous cell carcinoma cells. *Clin Cancer Res.* 2006;12:4103–4111.
18. Goldenberg A, Masui H, Divgi C, Kamrath H, Pentlow K, Mendelsohn J. Imaging of human tumor xenografts with an indium-111-labeled anti-epidermal growth factor receptor monoclonal antibody. *J Natl Cancer Inst.* 1989;81:1616–1625.
19. Scopinaro F, De Vincentis G, Banci M, et al. In vivo study of a technetium labelled anti-EGFr MoAB. *Anticancer Res.* 1997;17:1761–1765.
20. Reilly RM, Kiarash R, Sandhu J, et al. A comparison of EGF and MAb 528 labeled with ^{111}In for imaging human breast cancer. *J Nucl Med.* 2000;41:903–911.
21. Eiblmaier M, Meyer LA, Watson MA, Fracasso PM, Pike LJ, Anderson CJ. Correlating EGFR expression with receptor-binding properties and internalization of ^{64}Cu-DOTA-cetuximab in 5 cervical cancer cell lines. *J Nucl Med.* 2008;49:1472–1479.
22. Ping Li W, Meyer LA, Capretto DA, Sherman CD, Anderson CJ. Receptor-binding, biodistribution, and metabolism studies of ^{64}Cu-DOTA-cetuximab, a

PET-imaging agent for epidermal growth-factor receptor-positive tumors. *Cancer Biother Radiopharm.* 2008;23:158–171.
23. Cai W, Chen K, He L, Cao Q, Koong A, Chen X. Quantitative PET of EGFR expression in xenograft-bearing mice using ^{64}Cu-labeled cetuximab, a chimeric anti-EGFR monoclonal antibody. *Eur J Nucl Med Mol Imaging.* 2007;34:850–858.
24. Yang XD, Jia XC, Corvalan JR, Wang P, Davis CG. Development of ABX-EGF, a fully human anti-EGF receptor monoclonal antibody, for cancer therapy. *Crit Rev Oncol Hematol.* 2001;38:17–23.
25. Cai W, Wu Y, Chen K, Cao Q, Tice DA, Chen X. In vitro and in vivo characterization of ^{64}Cu-labeled Abegrin, a humanized monoclonal antibody against integrin alpha v beta 3. *Cancer Res.* 2006;66:9673–9681.
26. Graff BA, Bjornaes I, Rofstad EK. Microvascular permeability of human melanoma xenografts to macromolecules: relationships to tumor volumetric growth rate, tumor angiogenesis, and VEGF expression. *Microvasc Res.* 2001;61:187–198.
27. Wu AM, Olafsen T. Antibodies for molecular imaging of cancer. *Cancer J.* 2008;14:191–197.
28. Bernier J. Drug insight: cetuximab in the treatment of recurrent and metastatic squamous cell carcinoma of the head and neck. *Nat Clin Pract Oncol.* 2008;5:705–713.
29. Jain RK. Physiological barriers to delivery of monoclonal antibodies and other macromolecules in tumors. *Cancer Res.* 1990;50(3, suppl)814s–819s.
30. Fujimori K, Covell DG, Fletcher JE, Weinstein JN. A modeling analysis of monoclonal antibody percolation through tumors: a binding-site barrier. *J Nucl Med.* 1990;31:1191–1198.
31. Stoscheck CM, Carpenter G. Down regulation of epidermal growth factor receptors: direct demonstration of receptor degradation in human fibroblasts. *J Cell Biol.* 1984;98:1048–1053.
32. Lammerts van Bueren JJ, Bleeker WK, Bogh HO, et al. Effect of target dynamics on pharmacokinetics of a novel therapeutic antibody against the epidermal growth factor receptor: implications for the mechanisms of action. *Cancer Res.* 2006;66:7630–7638.
33. Wheeler DL, Huang S, Kruser TJ, et al. Mechanisms of acquired resistance to cetuximab: role of HER (ErbB) family members. *Oncogene.* 2008;27:3944–3956.
34. Chung CH, Ely K, McGavran L, et al. Increased epidermal growth factor receptor gene copy number is associated with poor prognosis in head and neck squamous cell carcinomas. *J Clin Oncol.* 2006;24:4170–4176.
35. Juweid M, Neumann R, Paik C, et al. Micropharmacology of monoclonal antibodies in solid tumors: direct experimental evidence for a binding site barrier. *Cancer Res.* 1992;52:5144–5153.

MOLECULAR IMAGING AND BIOLOGY

© Academy of Molecular Imaging, 2007

Mol Imaging Biol (2007)
DOI: 10.1007/s11307-007-0123-2

RESEARCH ARTICLE

Non-Invasive PET Imaging of EGFR Degradation Induced by a Heat Shock Protein 90 Inhibitor

Gang Niu, Weibo Cai, Kai Chen, Xiaoyuan Chen

The Molecular Imaging Program at Stanford (MIPS), Department of Radiology and Bio-X Program, Stanford University School of Medicine, 1201 Welch Rd, P095, Stanford, CA 94305-5484, USA

Abstract

Purpose: The aim of this study is to non-invasively monitor the epidermal growth factor receptor (EGFR) response to a Hsp90 inhibitor–17-AAG treatment in a PC-3 prostate cancer model.

Procedures: Nude mice bearing PC-3 tumor were injected intraperitoneally with 17-AAG and then imaged with micro positron emission tomography (microPET) using ^{64}Cu-DOTA–cetuximab. Biodistribution studies, immunofluorescence staining, and Western blot were performed to validate the microPET results.

Results: PC-3 cells are sensitive to 17-AAG treatment in a dose-dependent manner. Quantitative microPET showed that ^{64}Cu-DOTA–cetuximab has prominent tumor activity accumulation in untreated tumors (14.6±2.6%ID/g) but significantly lower uptake in 17-AAG-treated tumors (8.9±1.6% ID/g) at 24 h post-injection. Both immunofluorescence staining and Western blot confirmed the significantly lower EGFR expression level in the tumor tissue upon 17-AAG treatment.

Conclusions: The early response to anti-Hsp90 therapy was successfully monitored by quantitative PET using ^{64}Cu-DOTA–cetuximab, which indicates that this approach may be valuable in monitoring the therapeutic response to Hsp90 inhibitor 17-AAG in EGFR-positive cancer patients.

Key words: Epidermal growth factor receptor (EGFR), Positron emission tomography (PET), Heat shock protein 90 (Hsp90), 17-Allyamino-17-demethoxygeldanamycin (17-AAG), Cetuximab

Introduction

The epidermal growth factor receptor (EGFR) is a 170-kDa cell-surface protein overexpressed in many epithelial cancers [1]. Upon ligand binding, EGFR dimerizes either with itself to form a homodimer or with other human epidermal growth factor receptor (HER) family members to form heterodimers. Dysregulation of EGFR is associated with several key features of cancer such as autonomous cell growth, inhibition of apoptosis, angiogenic potential, invasion, and metastasis [2]. Gene amplification and/or overexpression of EGFR have been reported in several cancer types, including cancer of the bladder, prostate, kidney, lung, breast, and head and neck [3]. Several studies have indicated that the level of EGFR expression correlates with poor disease prognosis and reduced survival [4–7].

EGFR is now a validated target for the treatment of cancer patients [8]. Accurate evaluation of the EGFR status in tumors will provide guidance for EGFR targeted therapy either by antibodies [9] or tyrosine kinase inhibitors (TKIs) [10]. Analyzing the overexpression of EGFR in surgical specimens is most commonly accomplished by either immunohistochemical (IHC) staining or fluorescence *in situ*

Correspondence to: Xiaoyuan Chen; *e-mail:* shawchen@stanford.edu

hybridization testing [11, 12]. Currently, various non-invasive molecular imaging modalities are under intensive investigation to provide the comprehensive diagnostic information that can improve patient management [13, 14]. Previously, we reported the first quantitative positron emission tomography (PET) imaging of EGFR expression in xenograft-bearing mice using ^{64}Cu ($t_{1/2}$=12.7 h)-labeled cetuximab (Erbitux; C255; ImClone and Bristol-Myers Squibb) [15], a mouse–human chimeric IgG_1 mAb that binds with high affinity to EGFR [16]. Using up to seven xenograft tumor models, the tumor uptake of ^{64}Cu-DOTA–cetuximab measured by PET had good linear correlation (r^2=0.80) with the EGFR expression level as quantified by Western blotting [15]. MicroPET imaging showed that ^{64}Cu-DOTA–cetuximab had increasing tumor activity accumulation over time in EGFR-positive tumors but relatively low uptake in EGFR-negative tumors at all time points examined (<5 percentage injected dose per gram of tissue; % ID/g). The ability to quantitatively image EGFR expression by PET with ^{64}Cu-DOTA–cetuximab will enable future evaluation of EGFR expression level upon therapeutic intervention.

Non-invasive monitoring of EGFR expression is not only crucial to EGFR-targeted immunotherapy or radioimmunotherapy (RIT) but also important in other related chemotherapies. Recently, the chaperone heat shock protein (Hsp90) has emerged as a promising target for cancer therapy. The activity of Hsp90 promotes the attainment and maintenance of proper conformation of its clients, including EGFR, HER-2, Akt, and wild type or mutated androgen receptor, which are of potential importance in mediating prostate cancer progression [17–19]. An Hsp90 inhibitor, geldanamycin (GM), has been shown to have two distinct effects on EGFR: promoting its degradation and mediating its intracellular retention [20]. It has also been reported that 17-allyamino-17-demethoxygeldanamycin (17-AAG), a GM-derived Hsp90 inhibitor, could induce the degradation of both wild-type and mutant form EGFR [21]. The chaperone-associated degradation of EGFR is both proteasome- and ubiquitin-dependent [22]. 17-AAG possesses anti-tumor activity at nontoxic doses in various animal models [23], and phase II single-agent studies are now under way in patients with prostate cancer and cancers of other organ origins [24].

The assessment of early response to anti-cancer therapy can improve patient care by identifying patients who do not respond and, therefore, may not benefit from the therapy. These patients can greatly benefit from avoiding unnecessary toxic side effects and switching to different, more effective therapeutic approaches in a timely manner. Degradation of HER-2, another client protein of Hsp90, in a human breast cancer xenograft model by 17-AAG has been assessed by PET imaging [25]. Compared to 2-deoxy-2-[F-18]fluoro-D-glucose (FDG)–PET, which measured the tumor glucose metabolism, PET imaging of HER-2 expression was shown to provide more accurate information for early tumor response to 17-AAG treatment [26].

In this study, we treated a human prostate cancer PC-3 xenograft model with 17-AAG and carried out ^{64}Cu-DOTA-cetuximab PET before and after treatment. The goal of this study was to determine whether ^{64}Cu-DOTA-cetuximab PET could be used to monitor the early response of EGFR degradation upon anti-Hsp90 therapy by 17-AAG.

Materials and Methods

All commercially available chemical reagents were used without further purification. 1,4,7,10-Tetraazadodecane-*N*, *N′*,*N″*,N‴-tetra-acetic acid (DOTA) was purchased from Macrocyclics, Inc. (Dallas, TX, USA) and Chelex 100 resin (50–100 mesh) was purchased from Aldrich (St. Louis, MO, USA). Water and all buffers were passed though Chelex 100 column (1×15 cm) before use in radiolabeling procedures to ensure that the aqueous buffer is heavy metal free. PD-10 desalting columns were purchased from GE Healthcare (Piscataway, NJ, USA). Athymic nude mice were obtained from Harlan (Indianapolis, IN, USA) at 4–6 weeks of age. ^{64}Cu was provided by the University of Wisconsin–Madison. The human prostate cancer PC-3 cell line was obtained from the American Type Culture Collection and maintained in RPMI 1640 medium supplemented with 10% fetal bovine serum, 1% glutamine, 100 U/ml penicillin, and 100 mg/ml streptomycin (Invitrogen, Carlsbad, CA, USA).

3-(4, 5-Dimethylthiazol-2-yl)-2, 5-Diphenyl Tetrazolium Bromide Assay

The toxicity of 17-AAG to PC-3 cells was determined by 3-(4, 5-dimethylthiazol-2-yl)-2, 5-diphenyl tetrazolium bromide (MTT) assay. All studies were performed with triplicate samples and repeated at least three times independently. Briefly, cells were harvested by trypsinization, resuspended in RPMI 1640, and plated in a 96-well plate at 3,000 cells per well. At 72 h after treatment with different doses of 17-AAG (ranging from 1 nM to 2 μM) in 0.1% dimethylsulfoxide (DMSO; Sigma, St. Louis, MO, USA), the culture medium was replaced and 50 μl of 1.0 mg/ml sterile filtered MTT (Sigma) was added to each well. The unreacted dye was removed after 4 h, and the insoluble formazan crystals were dissolved in 150 μl of DMSO. The absorbance at 570 nm (reference wavelength, 630 nm) was measured with a Tecan microplate reader (Tecan, San Jose, CA, USA).

Flow Cytometry

Twenty-four hours after 17-AAG treatment, PC-3 cells were harvested and washed with phosphate-buffered saline (PBS) containing 0.5% bovine serum albumin (BSA). Upon blockade by 2% BSA in PBS, the cells were incubated with cetuximab (10 μg/ml in PBS containing 2% BSA). Flourescein isothiocyanate (FITC)-conjugated donkey anti-human IgG (1:200) was then added and allowed to incubate for 1 h at room temperature. After washing, the cells were analyzed using an LSR flow cytometer (Beckman Coulter, Fullerton, CA, USA). The FITC signal intensity was analyzed using the Cell-Quest software (version 3.3, Becton–Dickinson, Franklin Lakes, NJ, USA). In another flow cytometry study, both cetuximab and DOTA–centuximab with a concentration of 1 or 0.01 μg/ml were used under the same procedure as described above.

Tumor Model and Treatment Protocol

All animal experiments were performed under a protocol approved by the Stanford University Administrative Panel on Laboratory Animal Care (A-PLAC).

Subcutaneous PC-3 tumor models were established in 4 to 6-week-old male athymic nude mice. Typically, 5×10^6 cells suspended in 100 µl of serum-free RPMI 1640 medium were injected into the right front flank of the mice. The mice were subjected to microPET imaging studies when the tumor volume reached 200–400 mm^3 (3–4 weeks after inoculation). Animals in one group each received a total of 150 mg/kg of 17-AAG dissolved in 10% DMSO and 2% egg phospholipids (EPL; Avanti Polar Lipid, Alabaster, AL, USA) over a 24-h period in three doses of 50 mg/kg each (one dose every 8 h). The control animals were each injected with equal amounts of DMSO/EPL without 17-AAG.

MicroPET and Image Analysis

Detailed procedures for DOTA conjugation and DOTA number measurement have been reported earlier [15, 27]. $^{64}CuCl_2$ (74 MBq) was diluted in 300 µl of 0.1 M sodium acetate buffer (pH 6.5) and added to 50 µg of DOTA–cetuximab. The reaction mixture was incubated for 1 h at 40°C with constant shaking. ^{64}Cu-DOTA–cetuximab was then purified by PD-10 column using PBS as the mobile phase. PET of tumor-bearing mice was performed on a microPET R4 rodent model scanner (Siemens Medical Solutions USA, Inc.) as described earlier [15]. Twenty four hours after the last dose of 17-AAG treatment, the mice were intravenously injected with ^{64}Cu-DOTA–cetuximab (7–8 MBq/mouse), and static scans were acquired at 4 and 24 h post-injection (p.i.). For each microPET scan, 3D regions of interest (ROIs) were drawn over the tumor, liver, kidneys, and muscle on decay-corrected whole-body coronal images. The average radioactivity concentration within a tumor or an organ was obtained from mean pixel values within the ROI volume, which were converted to counts per milliliter per minute by using a conversion factor. Assuming a tissue density of 1 g/ml, the counts per milliliter per minute were converted to counts per gram per minute and then divided by the injected dose (ID) to obtain an imaging ROI-derived % ID/g.

Biodistribution Studies

After microPET imaging, mice bearing PC-3 tumor xenografts were sacrificed and dissected. Blood, tumor, and major organ tissues were collected and weighed (wet weight). The radioactivity in each tissue was measured using a γ-counter (Packard Instrument), and the results were presented as % ID/g. For each mouse, the radioactivity of the tissue samples was calibrated against a known aliquot of the injectate and normalized to a body mass of 30 g. Values were expressed as mean ± SD for a group of four animals. Mice bearing PC-3 tumors (n=4) were also injected with 7–8 MBq of ^{64}Cu-DOTA-IgG_1 (Jackson ImmunoResearch Laboratories, West Grove, PA, USA) with a similar procedure as described above to evaluate the non-specific uptake of ^{64}Cu-labeled antibody in the tumor.

Western Blot

After the microPET studies, the mice were sacrificed, and the tumor tissues were harvested and stored at −80°C. Tumor tissue protein was extracted using T-PER tissue protein extraction buffer (Pierce Biotechnology, Rockford, IL, USA) after the radioactivity had mostly decayed, and the concentration of total protein was determined using a microBCA protein assay kit (Pierce Biotechnology). After sodium dodecyl sulfate polyacrylamide gel electrophoresis separation of 40 µg of total protein, it was transferred to a polyvinylidene fluoride membrane (Invitrogen) and incubated at room temperature with 5% non-fat milk blocking buffer. The blots were then incubated overnight at 4°C with cetuximab, followed by incubation at room temperature for 1 h with horseradish-peroxidase-conjugated anti-human antibody (GE Healthcare, Piscataway). The bands were detected using an ECL Western blotting detection system (GE Healthcare, Piscataway) with α-tubulin as the loading control.

Immunofluorescence Staining

Frozen PC-3 tumor sections (5-µm thick) were warmed to room temperature, fixed with ice-cold acetone for 10 min, and dried in the air for 30 min. The sections were rinsed in PBS for 2 min and blocked in 10% donkey serum for 20 min at room temperature. The sections were incubated with cetuximab (10 µg/ml) for 1 h at room temperature and visualized with FITC-conjugated donkey anti-human secondary antibody (1:200, Jackson ImmunoResearch Laboratories) under a microscope (Axiovert 200M, Carl Zeiss USA, Thornwood, NY). Images were acquired under the same conditions and displayed at the same scale.

Statistical Analysis

Quantitative data were expressed as mean ± SD. Means were compared using one-way ANOVA and Student's t test. P values< 0.05 were considered statistically significant.

Results

17-AAG Inhibits PC-3 Cell Growth and Induces EGFR Degradation

The effect of 17-AAG on the cellular proliferation of PC-3 cells was assessed by MTT colorimetric assay. We found that 17-AAG inhibited cell proliferation in a dose-dependent manner (Fig. 1a). The IC_{50} value was about 68.7 nM at the 72-h time point. After being treated with 0.5 µM of 17-AAG for 72 h, the cell proliferating rate decreased to 39.5% of the control (treated with equal concentrations of DMSO in the absence of 17-AAG).

17-AAG has been reported to down-regulate EGFR expression in spite of inhibition of the Hsp90 function [21, 28]. Next, we performed flow cytometry analysis using cetuximab as the primary antibody to assess the effect of 17-AAG on EGFR expression level in PC-3 cells. As shown in Fig. 1b, 17-AAG significantly decreased EGFR expression. After incubation with 0.5 µM of 17-AAG for 24 h, the EGFR level dropped by 2.2-fold. These findings suggest that EGFR degradation is a potential indicator of the early response of PC-3 cells to 17-AAG treatment.

MicroPET Imaging of EGFR Degradation

^{64}Cu-DOTA–cetuximab was determined to have 21.5±2.2 DOTA residues per cetuximab, and control human IgG_1 had

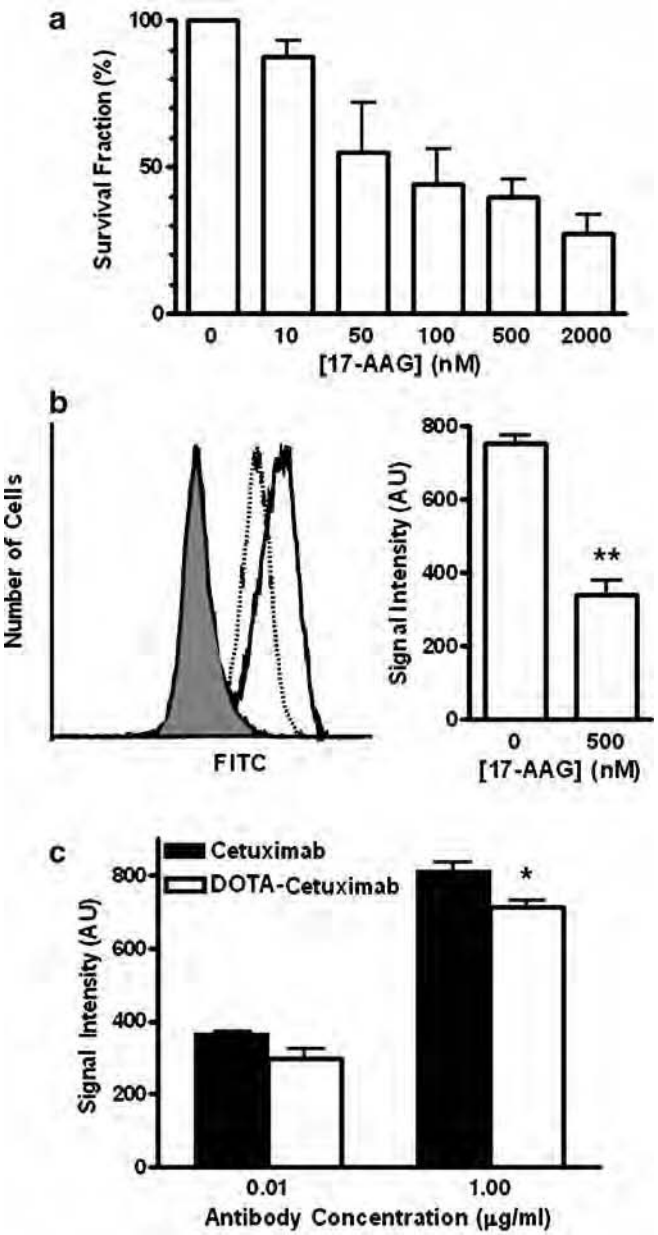

Fig. 1. **a** The cytotoxic effect of 17-AAG on human prostate cancer PC-3 cells. PC-3 cells were treated with serial concentrations of 17-AAG for 72 h, and the cell proliferation was determined by MTT assay. **b** Flow cytometric analysis of EGFR expression on PC-3 cells. *Solid line* Untreated cells, *dotted line* 17-AAG-treated cells, *solid line with shadow* negative control with secondary antibody only. Cetuximab was used as the primary antibody, and FITC-conjugated donkey anti-human IgG was used as secondary antibody. The mean value of FITC signal intensity of the three measurements were also shown (mean ± SD). **c** Immunoreactivity of DOTA–cetuximab, and cetuximab is determined by flow cytometry with PC-3 cells. *$P<0.05$.

24.08±0.42 DOTA residues ($n=4$). The specific activity of ^{64}Cu-DOTA–cetuximab was 1.24±0.13 GBq/mg mAb, and the radiolabeling yield was 84.0±8.7% ($n=5$) [15]. As shown in Fig. 1c, there was minimal reduction in the immunoreactivity of cetuximab after DOTA conjugation. Our previous study revealed that the uptake of ^{64}Cu-DOTA–cetuximab in the PC-3 tumor reached a plateau at about 24 h. Hence, in this study, the PC-3 tumor-bearing mice were scanned at 4 and 24 h p.i. of ^{64}Cu-DOTA–cetuximab. The

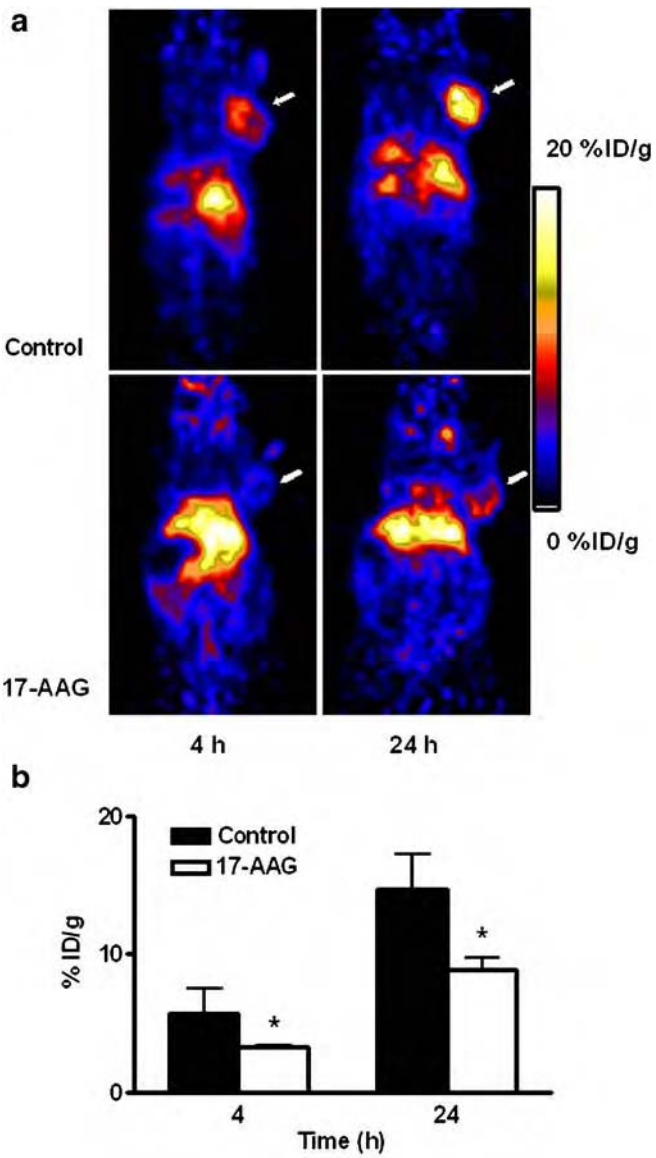

Fig. 2. **a** MicroPET images of PC-3 tumor-bearing nude mice at 4 and 24 h after intravenous injection of ^{64}Cu-DOTA–cetuximab with or without 17-AAG treatment ($n=4$ per group). Decay-corrected whole-body coronal images that contain the tumor were shown, and the tumors are indicated by *white arrows*. **b** PC-3 tumor uptake of ^{64}Cu-DOTA–cetuximab as quantified from microPET scans ($n=4$). *$P<0.05$.

decay-corrected whole-body coronal images that contained the tumor are shown in Fig. 2a. After being treated with 17-AAG for 24 h, the PC-3 tumor uptake of ^{64}Cu-DOTA–cetuximab was much lower in both early and late time points as compared with the untreated group. Quantitative data based on ROI analysis are shown in Fig. 2b. In untreated mice, the PC-3 tumor uptake of ^{64}Cu-DOTA–cetuximab was 5.8±1.7% ID/g and 14.6±2.6% ID/g at 4 and 24 h p.i., respectively. The uptake in 17-AAG-treated tumors was significantly lower, 3.3±0.3% ID/g and 8.9±1.6 %ID/g at 4 and 24 h p.i., respectively ($P<0.05$ at both time points; $n=4$). There were no significant difference of ^{64}Cu-DOTA–cetuximab uptake in other major organs between the 17-AAG-treated group and untreated animals.

Biodistribution Studies

After microPET imaging at 24 h p.i., the animals were sacrificed for biodistribution studies, and the results are shown in Fig. 3. The untreated PC-3 tumor had a high tracer uptake of 17.6±5.3% ID/g, consistent with the non-invasive microPET imaging results. After 17-AAG treatment, the uptake decreased significantly ($P<0.05$) to 10.1±0.7% ID/g. The liver also had prominent radioactivity accumulation, with an uptake of 17.1±4.2% ID/g at 24 h p.i., because of both the hepatic clearance of antibody-based tracer and possible trans-chelation. Blood activity concentration was 7.9±3.1% ID/g at 24 h p.i., indicating the long circulation life time of the antibody. Compared with ^{64}Cu-DOTA–cetuximab, ^{64}Cu-DOTA–IgG$_1$ has a higher blood concentration (14.3±2.4% ID/g) and lower liver uptake (7.4±1.8% ID/g). The non-specific accumulation of ^{64}Cu-DOTA–IgG$_1$ in the PC-3 tumor (because of the leaky vasculature and lack of lymphatic drainage in the tumor) was very low (4.3±0.5% ID/g at 24 h p.i.; $P<0.01$ compared with the control), confirming the EGFR specificity of ^{64}Cu-DOTA–cetuximab uptake in the PC-3 tumor.

Immunofluorescence Staining and Western Blot

To further confirm that 17-AAG induces EGFR degradation *in vivo*, we performed immunofluorescence staining using cetuximab as the primary antibody and Cy3-conjugated donkey anti-human IgG as the secondary antibody. Images were taken under the same condition and displayed at the same scale to make sure that the relative brightness observed in the images reflected the difference in EGFR expression level. In the untreated PC-3 tumor, EGFR expression was very high as indicated by the strong pseudo-colored red signal in the tissue (Fig. 4a). After treated with 17-AAG, EGFR expression was apparently lower with a much weaker fluorescence signal. Western blot of the tumor tissue lysate using cetuximab as the primary antibody also revealed that EGFR expression level in the PC-3 tumor decreased dramatically upon 17-AAG treatment (Fig. 4b). Taken together, biodistribution studies, immunofluorescence staining, and Western blot all confirmed that the decrease in tumor EGFR expression level upon 17-AAG treatment can be non-invasively monitored by ^{64}Cu-DOTA–cetuximab PET.

Discussion

In this study, we utilized a ^{64}Cu-labeled anti-EGFR mAb for the non-invasive monitoring of EGFR degradation, upon 17-AAG treatment, with microPET. The study demonstrated that quantitative PET imaging of EGFR expression can detect the early response to 17-AAG treatment in prostate tumors. *In vitro*, florescence-activated cell sorting (FACS) analysis revealed that EGFR expression level in PC-3 cells decreased by 2.2-fold after incubation with 0.5 μM of 17-AAG for 24 h. *In vivo*, ^{64}Cu-DOTA–cetuximab had significantly lower PC-3 tumor uptake when treated with the Hsp90 inhibitor 17-AAG (8.9% ID/g vs 14.6% ID/g at 24 h p.i.). It is worth mentioning that 17-AAG treatment did not completely ablate the EGFR expression either *in vitro* or *in*

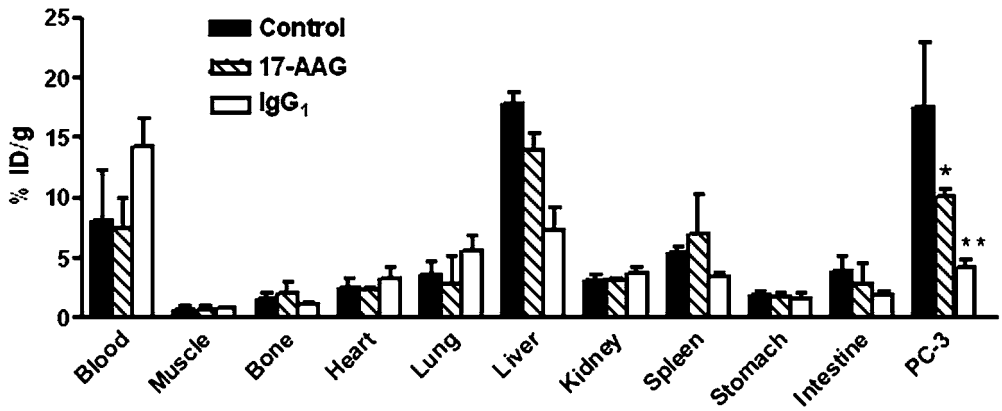

Fig. 3. Biodistribution of ^{64}Cu-DOTA–cetuximab (with or without 17-AAG treatment) and ^{64}Cu-DOTA-IgG$_1$ in PC-3 tumor-bearing mice at 24 h post-injection ($n=4$ for each group). *$P<0.05$; **$P<0.01$.

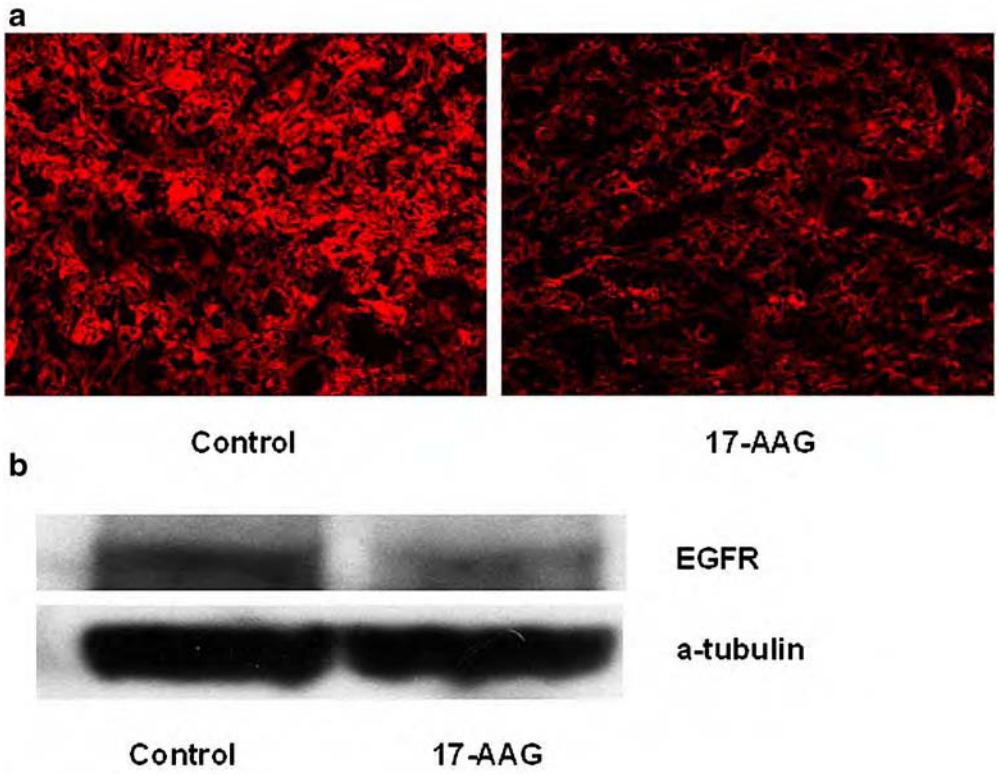

Fig. 4. **a** Immunofluorescence staining of EGFR in 17-AAG-treated and untreated PC-3 tumor tissues. Images were obtained under the same conditions and displayed at the same magnification and scale (×200). **b** Western blot of EGFR in PC-3 tumors treated or untreated with 17-AAG. Cetuximab was used as the primary mAb.

vivo, based on *in vitro* FACS analysis, *in vivo* microPET imaging, *ex vivo* biodistribution studies, immunofluorescence staining, and Western blot.

Of the four HER family members, both EGFR and HER-2 have been established as clients of Hsp90 [29, 30]. The interaction with Hsp90, as well as the regulation by Hsp90, differs between the two receptors, although the kinase domains of both receptors are responsible for the recruitment of Hsp90, and these domains share 80% identity in their amino-acid sequences [29]. HER-2 is dependent upon Hsp90 throughout its whole life span, including the maturation process in the endoplasmic reticulum (ER) and during its residency at the plasma membrane. On the other hand, EGFR is only dependent upon Hsp90 during its maturation in the ER [31]. HER-2-targeted PET imaging with antibody fragments or affibodies has been used to monitor the therapeutic response of Hsp90 inhibitors in human breast cancer models with high HER-2 expression [25, 26, 32]. However, HER-2 expression is typically much lower in tumors other than breast and ovarian tumors, in which HER-2 imaging has only limited applications. PC-3 cells had low HER-2 expression and 17-AAG treatment induced only minimal HER-2 degradation (data not shown). Thus, we chose to image EGFR degradation instead of HER-2 in this study.

We have studied the effect of different levels of DOTA conjugation on the tumor uptake of the resulting ^{64}Cu-labeled antibody. Five different DOTA: antibody reaction ratios (20:1, 50:1, 100:1, 200:1, and 1,000:1) were tested, and it was found that all five conjugates with different DOTA/antibody ratio exhibited good tumor contrast in target expressing tumor models [33]. Our previous study has demonstrated the linear correlation between the tumor uptake of ^{64}Cu-DOTA–cetuximab (measured by microPET) and the tumor EGFR expression level (measured by Western blot) in seven xenograft models including PC-3 [15], which provided the basis for this study because only quantitative PET imaging can allow for effective and non-invasive monitoring of the treatment efficacy. After DOTA conjugation, cetuximab retained a slightly decreased but acceptable immunoreactivity (Fig. 1c). In this study, ^{64}Cu-labeled human IgG_1 was also used as a negative control to evaluate the non-specific tumor uptake resulting from the leaky vasculature of tumors. At 24 h p.i., ^{64}Cu-DOTA–IgG_1 accumulation in PC-3 tumors (<5.0% ID/g) was much lower than ^{64}Cu-DOTA–cetuximab, consistent with previous reports on radio-labeled antibodies [34, 35]. The reason for the relatively higher circulating concentration and lower liver uptake of ^{64}Cu-DOTA–IgG_1 compared with ^{64}Cu-DOTA–cetuximab was unknown. The different pharmaco-

kinetics of individual antibody even if they are isotype-matched, as well as the variant influence of DOTA conjugation on the pharmacokinetics of different antibody, may be partially responsible for such discrepancy [36].

The slow clearance of antibody-based tracers (e.g., cetuximab) potentially makes them unsuitable for multiple microPET scans within short-time intervals. For such purposes, shorter half-life radioisotopes such as ^{18}F- ($t_{1/2}$= 110 min) or ^{68}Ga ($t_{1/2}$=68 min)-labeled small molecules, peptides, antibody fragments, or affibodies should be tested in the future. Trans-chelation may present a problem for radiocopper-labeling through DOTA chelator. However, we have found that ^{64}Cu-DOTA complex is very stable when attached to macromolecules or nanoparticles, with the majority of the ^{64}Cu label remaining intact after incubation in full mouse serum at 37°C for 24 h [37]. Nonetheless, other chelators suitable for more stable ^{64}Cu-labeling under mild conditions should be investigated further in the future. CB-TE2A, 4,11-bis(carboxymethyl)-1,4,8,11-tetraazabicyclo [6.6.2]hexadecane, has been reported to be superior than DOTA for overcoming trans-chelation [38]. However, the relatively harsh reaction conditions may not be optimal for antibody labeling.

Quantitative PET of EGFR expression can be applied to other EGFR-positive, 17-AAG-sensitive cancer types to monitor therapeutic effects during the early stages of treatment. It may also be used in other therapeutic strategies in which EGFR expression is regulated upon treatment. For example, histone deacetylase (HDAC) is capable of regulating gene expression through diverse mechanisms that include modulation of the histone code and acetylation of many non-histone proteins [39, 40]. HDAC inhibitors of diverse structures have shown preclinical and clinical promise as cancer therapeutics [41]. Moreover, given that HDAC inhibitors have been reported to reduce EGFR expression [42, 43], PET imaging of EGFR expression could also be utilized to predict the therapeutic response upon HDAC inhibitor therapy soon after initiation of the treatment.

In summary, we describe in this paper the use of quantitative PET imaging of EGFR expression with ^{64}Cu-DOTA–cetuximab for monitoring the early therapeutic response upon 17-AAG treatment in a human prostate cancer PC-3 tumor model. The quantification of EGFR degradation upon 17-AAG treatment using PET imaging is consistent with other *in vitro* and *ex vivo* measurements. This strategy may be applied to monitor the therapeutic response in EGFR-positive cancer patients under 17-AAG treatment.

Acknowledgment. This project was financially supported by the National Institute of Biomedical Imaging and Bioengineering (NIBIB; R21 EB001785), National Cancer Institute (NCI; R21 CA102123, P50 CA114747, U54 CA119367, and R24 CA93862), Department of Defense (DOD; W81XWH-04-1-0697, W81XWH-06-1-0665, W81XWH-06-1-0042, and DAMD17-03-1-0143), and a DOD Prostate Cancer Training Award PC073549 (to G. Niu), and a Benedict Cassen Postdoctoral Fellowship from the Education and Research Foundation of the Society of Nuclear Medicine (to W. Cai).

References

1. Arteaga C (2003) Targeting HER1/EGFR: a molecular approach to cancer therapy. Semin Oncol 30:3–14
2. Schlessinger J (2000) Cell signaling by receptor tyrosine kinases. Cell 103:211–225
3. Salomon DS, Brandt R, Ciardiello F, Normanno N (1995) Epidermal growth factor-related peptides and their receptors in human malignancies. Crit Rev Oncol Hematol 19:183–232
4. Raymond E, Faivre S, Armand JP (2000) Epidermal growth factor receptor tyrosine kinase as a target for anticancer therapy. Drugs 60:15–23
5. Veale D, Kerr N, Gibson GJ, Kelly PJ, Harris AL (1993) The relationship of quantitative epidermal growth factor receptor expression in non-small cell lung cancer to long term survival. Br J Cancer 68: 162–165
6. Raymond E, Faivre S, Armand JP (2000) Epidermal growth factor receptor tyrosine kinase as a target for anticancer therapy. Drugs 60: 15–23 (discussion 41)
7. Veale D, Kerr N, Gibson GJ, Kelly PJ, Harris AL (1993) The relationship of quantitative epidermal growth factor receptor expression in non-small cell lung cancer to long-term survival. Br J cancer 68:162–165
8. Gross ME, Shazer RL, Agus DB (2004) Targeting the HER-kinase axis in cancer. Semin Oncol 31:9–20
9. Ranson M, Sliwkowski MX (2002) Perspectives on anti-HER monoclonal antibodies. Oncology 63:17–24
10. Soulieres D, Senzer NN, Vokes EE, Hidalgo M, Agarwala SS, Siu LL (2004) Multicenter phase II study of erlotinib, an oral epidermal growth factor receptor tyrosine kinase inhibitor, in patients with recurrent or metastatic squamous cell cancer of the head and neck. J Clin Oncol 22:77–85
11. McManus DT, Patterson AH, Maxwell P, Humphreys MW, Anderson NH (1999) Fluorescence in situ hybridisation detection of erbB2 amplification in breast cancer fine needle aspirates. Mol Pathol 52:75–77
12. Stomper PC, Budnick RM, Stewart CC (2000) Use of specimen mammography-guided FNA (fine-needle aspirates) for flow cytometric multiple marker analysis and immunophenotyping in breast cancer. Cytometry 42:165–173
13. Weiner RE, Sasso DE, Gionfriddo MA, Syrbu SI, Smilowitz HM, Vento J, Thrall RS (1998) Early detection of bleomycin-induced lung injury in rat using indium-111-labeled antibody directed against intercellular adhesion molecule-1. J Nucl Med 39:723–728
14. Niu G, Cai W, Chen X (2008) Molecular imaging of human epidermal growth factor receptor 2 (HER-2) expression. Front Biosci 13:790–805
15. Cai W, Chen K, He L, Cao Q, Koong A, Chen X (2007) Quantitative PET of EGFR expression in xenograft-bearing mice using 64Cu-labeled cetuximab, a chimeric anti-EGFR monoclonal antibody. Eur J Nucl Med Mol Imaging 34:850–858
16. Ciardiello F, Damiano V, Bianco R et al. (1996) Antitumor activity of combined blockade of epidermal growth factor receptor and protein kinase A. J Natl Cancer Inst 88:1770–1776
17. Solit DB, Zheng FF, Drobnjak M et al. (2002) 17-Allylamino-17-demethoxygeldanamycin induces the degradation of androgen receptor and HER-2/neu and inhibits the growth of prostate cancer xenografts. Clin Cancer Res 8:986–993
18. Basso AD, Solit DB, Munster PN, Rosen N (2002) Ansamycin antibiotics inhibit Akt activation and cyclin D expression in breast cancer cells that overexpress HER2. Oncogene 21:1159–1166
19. Pratt WB, Toft DO (2003) Regulation of signaling protein function and trafficking by the hsp90/hsp70-based chaperone machinery. Exp Biol Med (Maywood) 228:111–133
20. Barzilay E, Ben-Califa N, Supino-Rosin L, Kashman Y, Hirschberg K, Elazar Z, Neumann D (2004) Geldanamycin-associated inhibition of intracellular trafficking is attributed to a co-purified activity. J Biol Chem 279:6847–6852
21. Lang SA, Klein D, Moser C et al. (2007) Inhibition of heat shock protein 90 impairs epidermal growth factor-mediated signaling in gastric cancer cells and reduces tumor growth and vascularization *in vivo*. Mol Cancer Ther 6:1123–1132
22. Sepp-Lorenzino L, Ma Z, Lebwohl DE, Vinitsky A, Rosen N (1995) Herbimycin A induces the 20 S proteasome- and ubiquitin-dependent degradation of receptor tyrosine kinases. J Biol Chem 270:16580–16587
23. Kelland LR, Sharp SY, Rogers PM, Myers TG, Workman P (1999) DT-Diaphorase expression and tumor cell sensitivity to 17-allylamino, 17-demethoxygeldanamycin, an inhibitor of heat shock protein 90. J Natl Cancer Inst 91:1940–1949

24. Solit DB, Rosen N (2006) Hsp90: a novel target for cancer therapy. Curr Top Med Chem 6:1205–1214
25. Smith-Jones PM, Solit DB, Akhurst T, Afroze F, Rosen N, Larson SM (2004) Imaging the pharmacodynamics of HER2 degradation in response to Hsp90 inhibitors. Nat Biotechnol 22:701–706
26. Smith-Jones PM, Solit D, Afroze F, Rosen N, Larson SM (2006) Early tumor response to Hsp90 therapy using HER2 PET: comparison with 18F-FDG PET. J Nucl Med 47:793–796
27. Cai W, Chen K, Mohamedali KA, Cao Q, Gambhir SS, Rosenblum MG, Chen X (2006) PET of vascular endothelial growth factor receptor expression. J Nucl Med 47:2048–2056
28. Yang S, Qu S, Perez-Tores M, Sawai A, Rosen N, Solit DB, Arteaga CL (2006) Association with HSP90 inhibits Cbl-mediated down-regulation of mutant epidermal growth factor receptors. Cancer Res 66:6990–6997
29. Murakami Y, Mizuno S, Uehara Y (1994) Accelerated degradation of 160 kDa epidermal growth factor (EGF) receptor precursor by the tyrosine kinase inhibitor herbimycin A in the endoplasmic reticulum of A431 human epidermoid carcinoma cells. Biochem J 301:63–68
30. Sakagami M, Morrison P, Welch WJ (1999) Benzoquinoid ansamycins (herbimycin A and geldanamycin) interfere with the maturation of growth factor receptor tyrosine kinases. Cell Stress Chaperones 4:19–28
31. Citri A, Alroy I, Lavi S et al. (2002) Drug-induced ubiquitylation and degradation of ErbB receptor tyrosine kinases: implications for cancer therapy. EMBO J 21:2407–2417
32. Orlova A, Tolmachev V, Pehrson R et al. (2007) Synthetic affibody molecules: a novel class of affinity ligands for molecular imaging of HER2-expressing malignant tumors. Cancer Res 67:2178–2186
33. Cai W, Wu Y, Chen K, Cao Q, Tice DA, Chen X (2006) *In vitro* and *in vivo* characterization of 64Cu-labeled AbegrinTM, a humanized monoclonal antibody against integrin avb3. Cancer Res 66:9673–9681
34. Weiner RE, Sasso DE, Gionfriddo MA, Syrbu SI, Smilowitz HM, Vento J, Thrall RS (1998) Early detection of bleomycin-induced lung injury in rat using indium-111-labeled antibody directed against intercellular adhesion molecule-1. J Nucl Med 39:723–728
35. Cai W, Ebrahimnejad A, Chen K, Cao Q, Li ZB, Tice DA, Chen X (2007) Quantitative radioimmunoPET imaging of EphA2 in tumour-bearing mice. Eur J Nucl Med Mol Imaging (in press)
36. van Gog FB, Visser GWM, Klok R, van der Schors R, Snow GB, van Dongen GAMS (1996) Monoclonal antibodies labeled with rhenium-186 using the MAG3 chelate: relationship between the number of chelated groups and biodistribution characteristics. J Nucl Med 37:352–362
37. Liu Z, Cai W, He L, Nakayama N, Chen K, Sun X, Chen X, Dai H (2007) *In vivo* biodistribution and highly efficient tumour targeting of carbon nanotubes in mice. Nature Nanotechnology 2:47–52
38. Boswell CA, Sun X, Niu W, Weisman GR, Wong EH, Rheingold AL, Anderson CJ (2004) Comparative *in vivo* stability of copper-64-labeled cross-bridged and conventional tetraazamacrocyclic complexes. J Med Chem 47:1465–1474
39. Strahl BD, Allis CD (2000) The language of covalent histone modifications. Nature 403:41–45
40. Johnson CA, White DA, Lavender JS, O'Neill LP, Turner BM (2002) Human class I histone deacetylase complexes show enhanced catalytic activity in the presence of ATP and co-immunoprecipitate with the ATP-dependent chaperone protein Hsp70. J Biol Chem 277:9590–9597
41. Drummond DC, Noble CO, Kirpotin DB, Guo Z, Scott GK, Benz CC (2005) Clinical development of histone deacetylase inhibitors as anticancer agents. Annu Rev Pharmacol Toxicol 45:495–528
42. Chinnaiyan P, Varambally S, Tomlins SA, Ray S, Huang S, Chinnaiyan AM, Harari PM (2006) Enhancing the antitumor activity of ErbB blockade with histone deacetylase (HDAC) inhibition. Int J Cancer 118:1041–1050
43. Yu X, Guo ZS, Marcu MG, Neckers L, Nguyen DM, Chen GA, Schrump DS (2002) Modulation of p53, ErbB1, ErbB2, and Raf-1 expression in lung cancer cells by depsipeptide FR901228. J Natl Cancer Inst 94:504–513

European Journal of Radiology xxx (2009) xxx–xxx

Contents lists available at ScienceDirect

European Journal of Radiology

journal homepage: www.elsevier.com/locate/ejrad

From protein–protein interaction to therapy response: Molecular imaging of heat shock proteins

Gang Niu, Xiaoyuan Chen*

The Molecular Imaging Program at Stanford (MIPS), Department of Radiology and Bio-X Program, Stanford University School of Medicine, 1201 Welch Rd, P095, Stanford, CA 94305-5484, USA

ARTICLE INFO

Article history:
Received 13 January 2009
Accepted 14 January 2009

Keywords:
Molecular imaging
Heat shock protein
HSP70
HSP90
Reporter gene
Positron emission tomography

ABSTRACT

HSP70 promoter-driven gene therapy and inhibition of HSP90 activity with small molecule inhibitors are two shining points in a newly developed cohort of cancer treatment. For HSP70 promoters, high efficiency and heat inducibility within a localized region make it very attractive to clinical translation. The HSP90 inhibitors exhibit a broad spectrum of anticancer activities due to the downstream effects of HSP90 inhibition, which interfere with a wide range of signaling processes that are crucial for the malignant properties of cancer cells. In this review article, we summarize exciting applications of newly emerged molecular imaging techniques as they relate to HSP, including protein–protein interactions of HSP90 complexes, therapeutic response of tumors to HSP90 inhibitors, and HSP70 promoters-controlled gene therapy. In the HSPs context, molecular imaging is expected to play a vital role in promoting drug development and advancing individualized medicine.

© 2009 Elsevier Ireland Ltd. All rights reserved.

1. Introduction

Molecular imaging is "the visualization, characterization, and measurement of biological processes at the cellular and molecular levels in humans and other living systems" [1]. Molecular imaging is a powerful new research tool that has only been made feasible by recent collaborative developments from diverse fields such as multiple image-capture techniques, cell and molecular biology, chemistry, medicine, pharmacology, medical physics, biomathematics and bioinformatics. Advanced multiple molecular imaging modalities have shed new light on a wide range of biomedical topics, including imaging specific cellular and molecular processes like gene expression or protein–protein interactions to optimize drug and gene therapies [2]. In this review, after a brief introduction of molecular imaging and heat shock proteins (HSPs), we discussed some important applications of molecular imaging for HSPs, mainly HSP70 and HSP90.

2. Molecular imaging

A molecular imaging agent typically has three main components: the targeting carrier, the imaging label, and a linker moiety (Fig. 1) although in some cases only one or two components also have the full function [3]. To date, a wide range of molecular imaging modalities are available, including techniques such as the positron emission tomography (PET), single-photon emission computed tomography (SPECT), molecular magnetic resonance imaging (mMRI), magnetic resonance spectroscopy (MRS), contrast enhanced ultrasound (CEU), optical bioluminescence, and optical fluorescence [2,4].

At present, PET is considered the most sensitive and specific technique for imaging molecular pathways *in vivo* in humans [5]. With probes labeled with positron-emitting radionuclides, PET produces a three-dimensional image or map of functional processes in the body. Another radionuclide-based imaging modality is SPECT. Due to its use of lead collimators to define the angle of incidence, however, SPECT imaging has a relatively low detection efficiency ($<10^{-4}$ times the emitted number of gamma rays) [6].

Non-radionuclide-based imaging techniques include MRI, ultrasound, and optical imaging. MRI is a non-invasive diagnostic technique based on the interactions of protons (or other nuclei) with one other and with surrounding molecules in a tissue of interest [7]. Different tissues have different relaxation times that can result in endogenous contrast. The major advantages of MRI over radionuclide-based imaging are the absence of radiation and higher spatial resolution (usually sub-millimeter level). The major disadvantage of MRI is its inherent low sensitivity, which can be partially compensated by working at higher magnetic fields (4.7–14 T), acquiring data for longer time periods during imaging, and using exogenous contrast agents. For ultrasound imaging, high-frequency sound waves are emitted from a transducer placed against the

* Corresponding author. Tel.: +1 650 725 0950; fax: +1 650 736 7925.
E-mail address: shawchen@stanford.edu (X. Chen).

0720-048X/$ – see front matter © 2009 Elsevier Ireland Ltd. All rights reserved.
doi:10.1016/j.ejrad.2009.01.052

Please cite this article in press as: Niu G, Chen X. From protein–protein interaction to therapy response: Molecular imaging of heat shock proteins. Eur J Radiol (2009), doi:10.1016/j.ejrad.2009.01.052

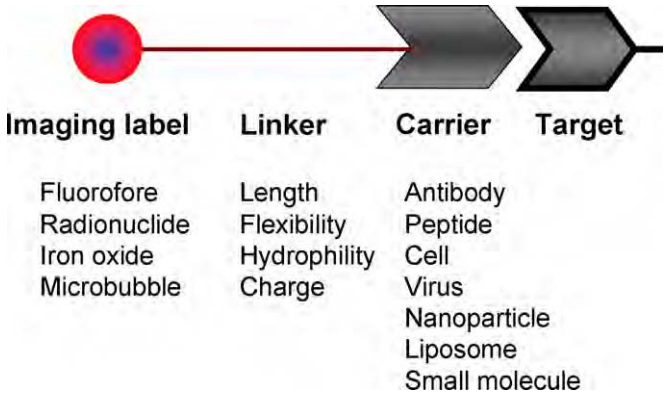

Fig. 1. An imaging agent is typically composed of an imaging label, a carrier that is/contains a targeting ligand, and a linker between the carrier and the label.

skin and ultrasound images are obtained based on the sound wave reflected back from the internal organs. The contrast of ultrasound is dependent on the sound speed, sound attenuation, backscatter, and the imaging algorithm [8]. Because of its safety, low cost, ease of use, and wide availability, ultrasonography is one of the most commonly used clinical imaging modalities [9]. Ultrasound contrast agents have been used in the clinic for applications such as blood pool enhancement, characterization of liver lesions, and perfusion imaging [10,11]. These contrast agents are generally in the form of small acoustically active particles ranging from several hundred nanometers to a few micrometers in diameter. X-ray computerized tomography (CT) is a medical imaging method that uses digital geometry processing to generate a 3-D image of the internals of an object from a large series of two-dimensional X-ray images taken around a single axis of rotation [12]. However, CT is not a typical molecular imaging modality due to the lack of target-specific contrast agents.

Two main branches of optical imaging are fluorescence imaging and bioluminescence imaging. In fluorescence imaging, excitation light illuminates the subject, and a charge-coupled device (CCD) camera collects the emission light at a shifted wavelength [2]. A number of high-resolution microscopic imaging techniques have recently been developed to study molecular events *in vivo*. In particular, intravital fluorescence microscopy [13], confocal laser scanning microscopy [14], multiphoton laser scanning microscopy [15], and *in situ* scanning force microscopy [16] have recently been introduced. The major limitation of optical imaging is that tissue light scattering and absorption can affect both image resolution and depth of light penetration of tissues [4]. Optical coherence tomography (OCT), an imaging technique with higher spatial resolutions (typically 10–15 μm), allows for real-time, cross-sectional imaging through biological tissues [17]. A series of fluorescent proteins, such as the green fluorescent protein, have also enabled sophisticated studies of protein function and wide-ranging processes from gene expression to second-messenger cascades and intercellular signaling, typically through fusion protein approach rather than through direct labeling [18]. Bioluminescence imaging (BLI) is based on the expression of a light-emitting enzyme (such as firefly luciferase) in target cells and tissues [19]. In the presence of its substrate (such as D-luciferin), an energy-dependent reaction releases photons that can be detected using sensitive detection systems. BLI has been applied for various applications such as studying gene-expression patterns [19], measuring gene transfer efficiency [20], monitoring tumor growth and response to therapy [21], investigating protein–protein interactions *in vivo* [22,23], and determining the location and proliferation of stem cells [24].

3. Heat shock proteins

Following exposure to protein-damaging environmental stresses, cells dramatically increase the expression of a group of proteins as an adaptive response to enhance protein renaturation, restore homeostasis, and improve survival—a process termed the "heat shock response" [25]. These heat shock proteins are named according to the approximate relative molecular weights of their encoded proteins, including HSP10, HSP27, HSP40, HSP60, HSP70, HSP90 and HSP110 [26,27]. The cytoprotective properties of the HSPs are closely linked to their primary functions as molecular chaperones [26].

HSP70 and HSP90 families are principal holding proteins which bind to unfolded sequences in polypeptide substrates and show preference for hydrophobic regions [28]. HSP70 and HSP90 function in large complexes or 'chaperone machines' containing several accessory proteins or co-chaperones that bind the primary chaperone to mediate substrate selection and cycles of association with, and disassociation from, the substrate [29]. After completion of their molecular chaperone function, HSP70 and HSP90 are actively released from protein substrates by means of their intrinsic ATPase domains [26].

In addition to serving as molecular chaperones, HSPs also have key functions in controlling cellular metabolism. Cell regulation by molecular chaperones is mediated by the holding ability of HSP70 and HSP90, each of which can bind stably to several regulatory molecules [29]. By interacting with key regulatory proteins, HSP90 has a principal role in regulating mitogenesis and cell-cycle progression, whereas HSP70 is closely involved in guarding against programmed cell death (PCD). Numerous cellular proteins undergo synchronous unfolding owing to the chaotropic effects of heat, which can lead to the cellular catastrophe of protein aggregation. Such protein aggregation is deterred by engagement of the heat-shock response and the accompanying abundant expression of the HSP cohort, which recognizes denatured proteins through the holding properties of HSP27, HSP70 and HSP90, and subsequently refolds them with the aid of chaperonins [30]. In addition, because protein denaturation and aggregation are powerful triggers of PCD, HSPs have developed powerful anti-apoptotic properties that deter PCD [29] and thus permit a time window for subsequent repair of the proteome [31]. The massive upregulation of HSPs that occurs during heat shock involves facilitation of expression at different levels, including activation of the potent heat-shock transcription factor 1 (HSF1), stabilization of HSP mRNA, selective translation of HSPs, and stabilization of HSPs at the protein level [32].

4. HSP90 and cancer

HSP90 is a key member of molecular chaperones that promote the proper folding of nascent polypeptides and ensure that protein–protein interactions occur in a productive manner under basal conditions [33]. HSP90 is an ATP-dependent molecular chaperone that forms a constitutive dimer. The N-terminal domain of HSP90 contains a unique ATP-binding site termed the Bergerat fold [34], which is essential for the ATP-dependent function of the chaperone *in vitro* and *in vivo*. Compared to other chaperones, HSP90 binds to substrate proteins that are at a later stage of folding [35]. Another unique characteristic of HSP90 is that it targets a specific set of client proteins that are mainly involved in signal transduction pathways including wild-type and mutated AR, p53, HER2, and Akt [29,36–38].

The HSP90 complex consist of the chaperone HSP70 and its co-chaperone HSP40, adapter protein Hop/p60, protein p23, and other helper proteins. The interactions between HSP90 and many of its co-chaperones occur within the C-terminal domain [29]. The dynamic interactions of HSP90 with its co-chaperones and client proteins

Please cite this article in press as: Niu G, Chen X. From protein–protein interaction to therapy response: Molecular imaging of heat shock proteins. Eur J Radiol (2009), doi:10.1016/j.ejrad.2009.01.052

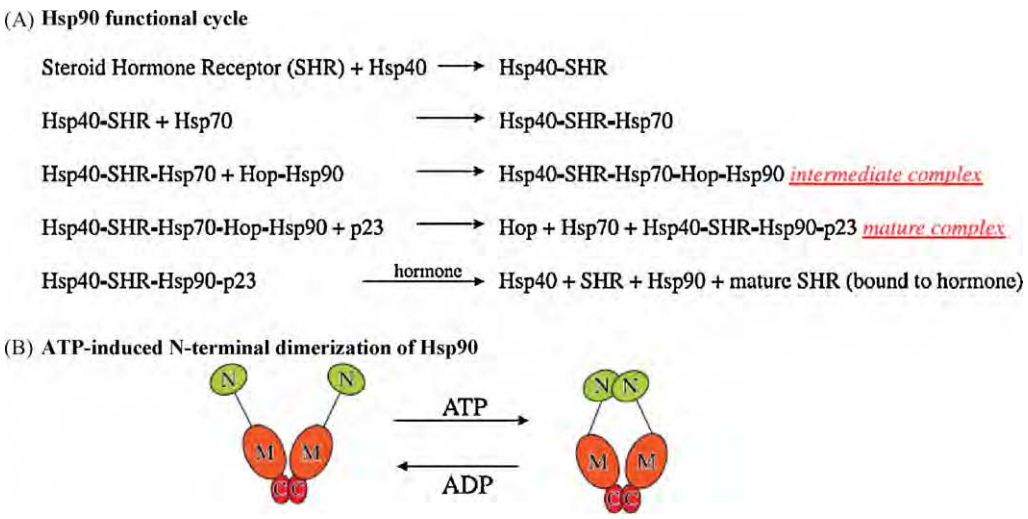

Fig. 2. HSP90 mechanism of function. (A) The maturation of steroid hormone receptor as mediated by HSP90. (B) The proposed nucleotide-dependent conformational changes in HSP90 [123].

are regulated via its intrinsic ATPase activity [39]. Repeated rounds of ATP hydrolysis promote and maintain proper client protein conformation; subsequently, clients can be released to perform their cellular duties. If the client protein fails to attain its proper conformation, or if it fails to encounter a requisite ligand or binding partner, it will be degraded via the 26S proteasome (Fig. 2) [40].

There is growing evidence that HSP90 plays an important role in the progress of the malignant disease. Elevated HSP90 levels have been observed in patients who suffer from various forms of cancer, including breast, brain, colon, and lung cancers [41,42]. Inhibition of extracellular HSP90α, which localizes to the extracellular space in aggressive melanoma cells, decreases both MMP2 activity and tumor invasiveness, evidence that HSP90 may directly influence the metastatic process in tumors [43]. In addition, HSP90 is more extensively engaged with multiprotein complexes in tumor cells as compared to their normal counterparts, which suggests that tumor cells require greater HSP90 activity [44]. One explanation of tumor cells' need for HSP90 is that tumor cells proliferate more rapidly, hence requiring more client proteins to be processed. In addition, tumors often exist in hostile, nutrient-poor environments that could promote protein unfolding [45]. Furthermore, tumors often harbor an enormous mutational load. Such mutations may lead to extensive protein mis-folding, thereby generating a higher concentration of client proteins that require assistance from HSP90, including natural binding partners and novel clients such as the unique fusion oncoproteins BCR-ABL and NPM-ALK [45,46]. Another intriguing possibility is that HSP90 might serve as a biochemical "buffer" in tumor cells, maintaining phenotypic normalcy in a highly stressful environment [47,48]. HSP90 might facilitate the ability of these cells to tolerate the accumulation of mutations during malignant transformation and progression.

5. Cancer treatment through inhibition of HSP90

ATP hydrolysis-dependent release of HSP90 from the complex is the last step in HSP90 client protein cycle. Occupancy of the HSP90 pocket by ansamycins results in an inactive HSP90-protein complex which is then degraded by a ubiquitin-dependent mechanism [49,50]. One of the inhibitors of HSP90 chaperone protein, 17-allyamino-17-demethoxygeldanamycin (17-AAG), is now in phase II clinical trial against melanoma, breast, prostate, and thyroid cancers. 17-AAG binds to HSP90 with high affinity in its N-terminal nucleotide binding pocket [51], promoting the destabilization of most HSP90 client proteins [52]. A problem in targeting HSP90 concerns the side effects of drugs that could impair normal cellular functions. Kamal et al. [44] have shown that HSP90 in tumor cells exists predominantly in multi-protein complexes, with a scant presence in normal cells. The complex, activated form of HSP90 in tumors was shown to possess a much higher affinity for 17-AAG; similarly, following systemic administration to mice, the drug appears to be selectively retained in their tumor burdens. Consistent with these findings, both preclinical and phase I studies of 17-AAG have shown that biologically relevant drug exposures can be achieved with a surprisingly modest toxicity [53,54].

The low micromolar binding affinity of geldanamycin (GA) and its derivatives with HSP90 *in vitro* [51] stands in stark contrast to the low nanomolar anti-proliferative activity that the drug exhibits *in vivo* [55]. Chiosis et al. [55] have proposed that the physicochemical properties of the ansamycins result in its intracellular accumulation in cell culture media, making highly potent antiproliferative activity possible [56]. Kamal and co-workers [44] provided biochemical evidence that HSP90 in cancer cells exists primarily in a multichaperone complex that has a higher affinity for GA compared to the HSP90 in normal cells, where the majority of the protein is *not* present in a high molecular mass complex, or purified HSP90. However, other studies suggest that HSP90 undergoes a slow conformational change upon binding of GA in a tight interaction. The slow, tight-binding of GA has been proposed as a possible explanation for the accumulation of GA in tumor cells due to the law of mass action, thereby increasing in the apparent affinity of tumor-specific HSP90 [57]. Another study has proposed that reduction of the quinine moiety in GA may have an important role in enhancing binding and selectivity [58]. The requirement of isomerization of GA before tight binding has been postulated as a possible reason behind the enhanced binding affinity of GA for HSP90 *in vivo* compared to its purified form *in vitro* [59]. A more recent study conducted by Onuoha et al. [60] confirmed that the reduced dihydroquinone form of the drug binds to HSP90 considerably more tightly than the non-reduced quinone species.

6. HSP90 activity measurement with fluorescent probes

During the development of new HSP90 inhibitors, it is critical to determine the binding affinity of potential compounds with HSP90, which is important for high throughout screen (HTS). Several direct and competitive assay methods have been used to gauge the interactions of ligands with the N-terminal domain of HSP90. These include the measurement of ATPase activity [61,62], binding of a flu-

Please cite this article in press as: Niu G, Chen X. From protein–protein interaction to therapy response: Molecular imaging of heat shock proteins. Eur J Radiol (2009), doi:10.1016/j.ejrad.2009.01.052

orescent ATP analog [63], displacement of HSP90 from immobilized GA [64,65], isothermal calorimetry measurement of the binding of radicicol or GA [51], and filter binding assay with ^{3}H labeled GM derivatives [66]. In this section we will focus on using fluorescent probes to measure HSP90 activity. Although these probes are currently used for *in vitro* test, they have the potential to be used *in vivo* for near-infrared fluorescence imaging.

When a fluorescent sample is excited with a polarized light, the emission is polarized. This phenomenon is called fluorescence polarization (FP). Small dye molecules are rapidly rotating molecules and the initially photoselected orientational distribution is randomized prior to emission, creating low fluorescence polarization. Llauger-Bufi et al. [63] linked two fluorescent dyes primarily used in FP assays, FITC and BODIPY, on the C17 position of GM because the methoxy group found at this position easily undergoes a Michael reaction while in the presence of primary amines. In a competitive displacement study of GM-BODIPY by HSP90 Inhibitors, a purine-based small molecule PU3 was found to be 30-fold weaker HSP90 inhibitor than the 17-AAG (EC_{50} = 3.2 μM *vs*. 110 nM). To avoid the interference from test compounds, the same group switched to a red-shifted dye (Cy3B) in labeling the FP ligand [67]. With the red-shifted cy3B-GM ligand, they evaluated the applicability of this tracer as a FP probe for HSP90. The EC_{50} for 17-AAG and ADP determined by this probe are 64.9 ± 3.8 nM and 120 μM, respectively. The difference between cy3B-GM and BODIPY-GM may be due to the reduced interference of fluorescent compounds as fewer library members emit at such long wavelengths as cy3B. Introduction of a red-shifted dye like cy3B may also help reduce false-positives resulted from light scattering caused by insoluble compounds.

By taking advantage of the high sensitivity of luminometer, thermally denatured firefly luciferase has been used to identify the active principles responsible for facilitating protein renaturation. The results indicated that refolding of heat-denatured luciferase is HSP90-dependent [68]. Using this strategy, the same group has developed a high-throughput assay to identify inhibitors that obstruct the chaperone activity of HSP90 either by directly binding to its N-terminal or C-terminal nucleotide binding sites or by interfering with the ability of the chaperone to switch conformations. More than 20,000 compounds were screened and 120 compounds that inhibited luciferase renaturation by greater than 70% at a concentration of 12.5 μg/mL were identified [69]. Though these fluorescent probes and HSP90 dependent luciferase were initially developed for *in vitro* screening of HSP90 inhibitors, they also can be further tailored for *in vivo* molecular imaging of HSP90 activity.

7. Imaging of protein–protein interaction in HSP complexes

Non-covalent interactions among proteins are vital for all aspects of cellular processes. A plethora of techniques have been developed to detect protein–protein interactions at extracellular and intracellular levels, including the yeast two-hybrid assay and the co-immunoprecipitation assay [70]. These assays usually need lengthy procedures that are influenced by parameters. The development of reporter-based *in vivo* protein–protein interaction assays, such as fluorescence resonance energy transfer (FRET) [71], bioluminescence resonance energy transfer (BRET) [72], and bimolecular fluorescence complementation (BiFC) [73] assays, has significantly advanced the measurement of protein–protein interactions *in vivo*. Using the "fluorescence recovery after photobleaching" (FRAP) technology, for instance, Picard [74] examined the dynamics of human p23, expressed as a fusion protein with the green fluorescent protein (GFP), in living human HeLa cells. When the HSP90 interaction was disrupted either by the HSP90 inhibitor GA or by introduction of point mutations into p23, the mobility of p23 was greatly accelerated [74]. A 2-color FRAP technique has also been developed by the same group to facilitate the analysis and to allow a direct comparison with p23, in which two test proteins are expressed as fusion proteins with the two spectrally separable fluorescent proteins, mCherry and enhanced green fluorescent protein (eGFP). Under this 2-color FRAP, it has been observed that HSP90 and p23 are virtually indistinguishable, consistent with the notion that they are both engaged in a multitude of large protein complexes. However, when HSP90-p23 complexes are disrupted by the HSP90 inhibitor GA, p23 moves by free diffusion while HSP90 maintains its low mobility because the latter remains bound in remodeled multicomponent complexes [75]. In these studies, the fluorescent signal was observed by a microscope, and imaging was still limited to cultured living cells.

In the recently improved firefly luciferase complementation imaging (LCI) assay, luciferase enzyme is divided into the N- and C-terminal halves that do not spontaneously reassemble and function. Luciferase activity occurs only when the two fused proteins interact, resulting in the reconstituted luciferase enzyme, which can be detected by a luminometer or a highly sensitive CCD camera. The assay measures dynamic changes in protein–protein interactions and can be used for both cell culture and whole animals [76,77]. Recently, Chan et al. [22] developed a HSP90/p23 interaction imaging system that could evaluate the importance of isoform-selective HSP90α/p23 and HSP90β/p23 interactions in determining the sensitivity to HSP90 by using 293T human kidney cancer cells that stably expressed split Renilla luciferase (RL) reporters. Interactions between HSP90α/p23 and HSP90β/p23 in the split RL reporters led to the complementation of RL activity, which was determined by bioluminescence imaging of intact cells in cell culture and living mice using a CCD camera. Through this novel genetically coded reporter gene strategy, RL activities have been correlated with the interactions of HSP90 and p23, thus allowing the function of HSP90 to be assessed after cells or animals were administered with different HSP90 inhibitors (e.g., three GA-based and seven purine-scaffold HSP90 inhibitors). Among them, the most potent HSP90 inhibitor, PU-H71, led to a 60% and 30% decrease in RL activity (14 h) in 293T xenografts expressing HSP90α/p23 and HSP90β/p23 split reporters, respectively, relative to carrier control-treated mice (Fig. 3) [22]. With molecular imaging, it is now possible to visualize the HSP90-p23 interactions non-invasively and longitudinally in living animals and eventually, humans. The success of this strategy will greatly improve the drug selection process for more potent and isoform-selectiveHSP90 inhibitors.

8. Molecular imaging of therapeutic response of HSP90 inhibitors

Early phases of clinical trials that investigate the effects of novel molecular-targeted agents such as 17-AAG and HSP90 must be designed very carefully as proof-of-principle, hypothesis-testing studies, with extensive use of pharmacodynamic endpoints and pharmacogenetic biomarkers [78]. Invasive biopsy and body fluid sampling have been the conventional methods for obtaining cellular and tissue samples for laboratory-based analysis of therapeutic endpoints. However, the difficulty and low yields of biopsy collection, as well as the low sensitivity of traditional immunohistochemical techniques that can only identify partial but not complete reductions in protein expression, significantly limit the feasibility of such studies. By contrast, non-invasive molecular imaging has evolved into a highly fruitful approach for monitoring suitable endpoints of molecular medicine interventions [79].

The downstream effects of HSP90 inhibition affect a wide range of signaling processes that are crucial for the malignant properties of cancer cells. Indeed, HSP90 inhibitors exhibit a broad spectrum of anticancer activities. In addition, analyses of treatment-induced changes in relevant HSP90 client proteins can be used as pharma-

Please cite this article in press as: Niu G, Chen X. From protein–protein interaction to therapy response: Molecular imaging of heat shock proteins. Eur J Radiol (2009), doi:10.1016/j.ejrad.2009.01.052

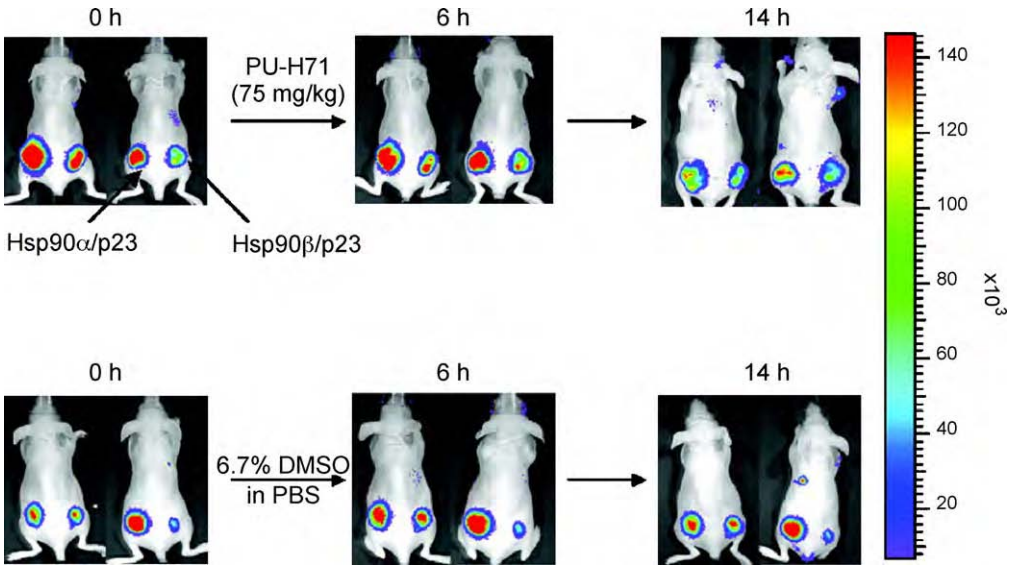

Fig. 3. Disruption of Hsp90α/p23 and Hsp90β/p23 interactions by Hsp90 inhibitors in living mice. 293T cells stably transfected with NRL(M185 V)-p23/Hsp90α2.2-CRL (*left*) or NRL(M185 V)-p23/Hsp90β2.2-CRL (*right*) were implanted subcutaneously in the lower flanks of each female nude mouse to allow xenograft establishment for 2 weeks, respectively. Mice were imaged at 0 h to determine the RL activities in the implanted cells by optical bioluminescence imaging using a cooled CCD camera with an acquisition time of 3 min immediately after tail vein injection of coelenterazine. Mice were subsequently i.p. injected with Hsp90 inhibitor PU-H71. Control mice were treated i.p. with equal volume of carrier control. RL activity was determined at 6 and 14 h posttreatment. Representative images from two mice from each treatment group at each time point are shown with the optical bioluminescence image superimposed on the visible light image [22].

codynamic endpoints for the evaluation of therapeutic response. For example, HER-2 has been established as a client of HSP90, and its stability is dependent upon HSP90 throughout the whole lifespan of the receptor, including the maturation process in the ER and during the residency of the receptor at the plasma membrane. (HER-2 is depleted within 2 h of HSP90 inactivation [80].) Much of the recent interest in HER-receptors is due to the role they play in human malignancies. Hyperactivation of HER signaling pathways, for instance, is implicated in driving the proliferation of many cancer cell types, and is often correlated with poor patient survival. The overexpression of HER-2 has been detected in up to 30% of breast and ovarian cancers and a high frequency of HER-2 overexpression has also been noted in other common types of cancers such as prostate cancer [81,82]. Multimodality imaging techniques, including optical imaging, SPECT, PET, MRI and ultrasound, have been used to target HER-2 with various probes, most of which were developed based on anti-HER-2 antibodies, antibody derivatives (e.g., scFv, antibody fragments and other engineered antibodies) and affibodies [83,84].

Smith-Jones et al. [85] labeled a $F(ab')_2$ fragment of trastuzumab (humanized antibody against HER-2) with a positron emitter ^{68}Ga ($t_{1/2}$ = 68 min) to assess the degradation of HER-2 by a HSP90 inhibitor, 17-AAG. Taking advantage of the fast blood clearance of $F(ab')_2$ and quick decay of ^{68}Ga, they repetitively imaged HER-2 expression at 24 h intervals. Based on the small-animal PET quantification, the HER-2 expression was reduced by almost 80% in the animals 24 h after 17-AAG treatment [85]. In a follow-up study, the tumor response to 17-AAG treatment was assessed by ^{68}Ga-DOTA-$F(ab')_2$-trastuzumab and ^{18}F-FDG PET. Within 24 h after treatment, a significant decrease in HER-2 was measured by HER-2 PET, whereas the ^{18}F-FDG PET uptake was virtually unchanged. The 17-AAG treated animals had a reduced uptake of ^{68}Ga-$F(ab')_2$-trastuzumab that lasted until 5 days after treatment, although notable growth inhibition occurred only by 11 days after treatment. The ^{18}F-FDG PET imaging data revealed no significant differences in ^{18}F-FDG metabolism between the treated and control group at any of the time points examined. This indicates that HER-2-PET with ^{68}Ga-DOTA-$F(ab')_2$-trastuzumab can provide accurate information for a tumor's early response to 17-AAG treatment [86]. It is worth noting that the detailed pharmacokinetic analysis performed in these studies is *not* feasible using previously traditional techniques. In future phase II studies, it will be crucial to identify the optimal dose and schedule for the usage of HSP90 inhibitors [87].

Of the four HER family members, EGFR and HER-2 have been established as clients of HSP90 [88,89]. However, HER-2 expression is typically much lower in tumors other than breast and ovarian tumors. Previously we reported the first quantitative PET imaging of EGFR expression in xenograft-bearing mice using ^{64}Cu ($t_{1/2}$ = 12.7 h)-labeled cetuximab (Erbitux; C255; ImClone and Bristol-Myers Squibb) [90], a mouse–human chimeric IgG_1 mAb that binds with high affinity to EGFR [91]. Using up to seven xenograft tumor models, the tumor uptake of ^{64}Cu-DOTA-cetuximab measured by PET had good linear correlation (r^2 = 0.80) with the EGFR expression level as quantified by Western blotting [90]. Small-animal PET imaging studies showed that ^{64}Cu-DOTA-cetuximab had increasing tumor activity accumulation over time in EGFR-positive tumors, but relatively low uptake in EGFR-negative tumors at all time points examined (< 5% injected dose per gram of tissue; %ID/g). The ability to quantitatively image EGFR expression by PET with ^{64}Cu-DOTA-cetuximab will enable the evaluation of EGFR expression level upon therapeutic intervention in the future. To determine whether ^{64}Cu-DOTA-cetuximab PET could be used to monitor the early response of EGFR degradation upon anti-HSP90 therapy by 17-AAG, we treated a human prostate cancer PC-3 xenograft model with 17-AAG and carried out ^{64}Cu-DOTA-cetuximab PET before and after treatment. Quantitative PET showed that ^{64}Cu-DOTA-cetuximab had prominent tumor activity accumulation in untreated tumors (14.6 ± 2.6%ID/g) but significantly lower uptake in 17-AAG-treated tumors (8.9 ± 1.6% ID/g) at 24 h post-injection. Both immunofluorescence staining and Western blot confirmed the significantly lower EGFR expression level in the tumor tissue upon 17-AAG treatment. The results demonstrated that the early response to anti-HSP90 therapy can be monitored by quantitative PET using ^{64}Cu-DOTA-cetuximab; therefore, this approach may be valuable in monitoring the therapeutic response to HSP90 inhibitor 17-AAG in EGFR-positive cancer patients (Fig. 4)

Please cite this article in press as: Niu G, Chen X. From protein–protein interaction to therapy response: Molecular imaging of heat shock proteins. Eur J Radiol (2009), doi:10.1016/j.ejrad.2009.01.052

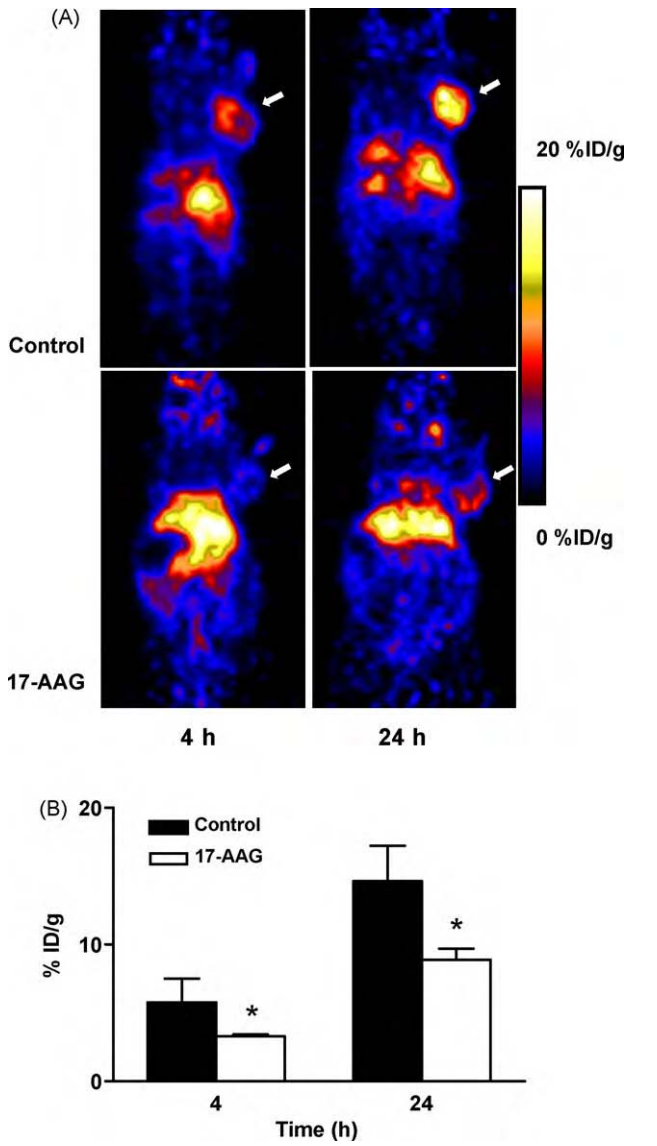

Fig. 4. (A) MicroPET images of PC-3 tumor-bearing nude mice at 4 h and 24 h after intravenous injection of ^{64}Cu-DOTA-cetuximab with or without 17-AAG treatment. Decay-corrected whole-body coronal images that contain the tumor were shown, and the tumors are indicated by white arrows. (B) PC-3 tumor uptake of ^{64}Cu-DOTA-cetuximab as quantified from microPET scans [92].

[92]. In addition to HER2 and EGFR, a wide range of HSP90 client proteins, including AR, Akt, and p53, may be targeted with specific small molecular probes to evaluate HSP90 therapy, though it is more problematic if the targets are not membrane proteins, due to the complexity for imaging and image analysis.

Given their excellent spatial resolution, CT and MRI are used extensively in routine clinical work and they can image tumor mass and volume in real-time manner. For example, non-invasive MRI has been applied to test the synergistic effects of HSP90 inhibitor and glycolysis inhibitor for pancreatic cancer therapy in a transgenic spontaneous pancreatic cancer mouse model [24].

9. Imaging of HSP70-related gene therapy

Heat shock protein promoters, particularly HSP70 promoters, have often been used for gene therapy strategies because they are both heat-inducible and efficient [93]. When eukaryotic cells are exposed to temperatures above their optimum for growth, they respond by inducing HSPs. Transcription is vigorously initiated at the HSP gene loci within minutes. Of the seven major HSPs, HSP70 is not only the most prominently induced but also always first to be repressed in step with restoration of normal synthesis. Thus, the sharp response pattern of HSP70 has attracted interest in the possible therapeutic use of its promoter as a molecular tool for gene therapy. Promoters from HSP70 genes are characterized by the presence of multiple adjacent inverse iterations of the pentanucleotide motif 5'-nGAAn-3', whose assemblies are called heat shock elements (HSEs) [94]. Heat shock promoter activation is mediated in large part by the interaction of heat shock factor 1 (HSF1) with HSEs. Physiological stresses (e.g., heat) induce HSF1 monomers to oligomerize as homotrimers, allowing translocation in the nucleus and binding to HSEs [93]. In humans, two HSP70 genes, HSP70-1 (HSP70A1A locus) and HSP70-2 (HSP70A1B locus), are found as a nearly identical tandem pair [95]. The HSP70B promoter contains three functionally important HSEs and an atypical TATA sequence. During the 24 h period following heat shock, the HSP70B minimal promoter can drive expression of reporter genes at levels comparable to those produced by the cytomegalovirus (CMV) immediate early promoter in human tumor cells [96].

Various attempts have been made to engineer HSP promoters in order to further increase their efficiency. A modified HSP70B promoter containing four additional HSE sequences has been constructed and was found to be more efficient than the original promoter [97]. However, absolute levels of expression as well as the enhancement produced by promoter modification varied in the different cell lines. Another attempt to enhance the efficiency of the HSP70 promoter employed a two-step molecular amplification system, in which the first transcriptional unit contained the HSP70B promoter that controlled the expression of a transcriptional factor, HIV Tat, whose factor transactivated a second promoter, the HIV2 LTR, located downstream on the same construct. The second promoter drives the gene of interest [98]. Using such a construct, heat induced human interleukin-2 has been expressed to 35–70-fold higher than achieved by using the HSP70 promoter alone, and 10–35-fold higher than the level achieved by using the CMV promoter.

In addition to their high efficiency, HSP70 promoters also provide a high level of control over therapeutic gene expression. A temperature-dependent increase of reporter expression was found using the human HSP70B promoter, while very low basal levels of reporter/therapeutic gene expression were reported [99]. Modulation by heat of the HSP70B promoter activity *in vitro* raised the possibility that expression of a therapeutic gene might be modulated *in vivo* by hyperthermia. The development of non-invasive methods such as focused ultrasound (FUS) that allow a precise control of both the thermal dose applied to tissues and the resulting elevation of temperature *in situ* facilitated the usage of the HSP70B promoter controlled therapeutic gene expression. By coupling FUS with MRI temperature mapping, the thermal dose could be precisely controlled, allowing the fine-tuning of reporter gene expression based on temperature [100,101].

Treating tumors by introducing into tumor cells a suicide gene such as those coding for thymidine kinase (TK) or cytosine deaminase (CD) under the control of an HSP promoter has been examined by numerous studies [102,103]. Braiden and co-workers [104] have developed a hyperthermic suicide gene (HSV-tk) therapy under the control of an HSP70 promoter for the eradication of breast cancer xenografts. By implanting breast cancer cells in subcutaneous and intraperitoneal models of BALB/c nude mice, significant tumor regression was observed in HSP-tk-transduced tumors following hyperthermic therapy and injection of ganciclovir (GCV). Using both CD and TK suicide genes controlled by HSP70 promoters, Brade et al. [105] demonstrated that a combined treatment approach can be highly effective against heat- and radiation-resistant breast tumor cells. A similar strategy was based on the Gibbon ape leukemia

Please cite this article in press as: Niu G, Chen X. From protein–protein interaction to therapy response: Molecular imaging of heat shock proteins. Eur J Radiol (2009), doi:10.1016/j.ejrad.2009.01.052

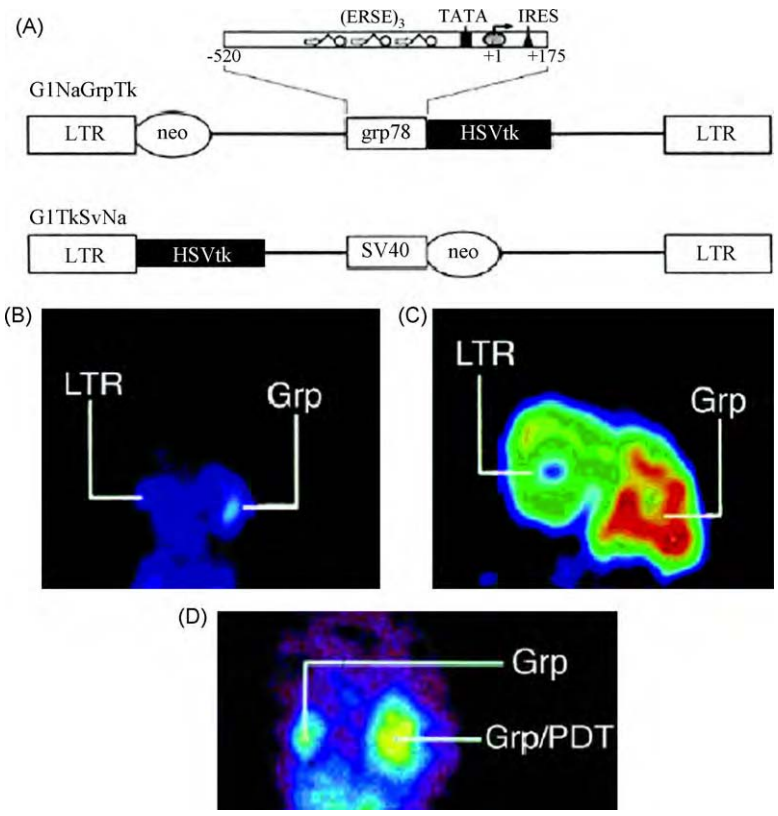

Fig. 5. Positron emission tomography (PET) imaging of transduced TSA tumors. (A) Schematic drawing of the retroviral vectors G1NaGrpTk and G1TkSvNa. (B and C) Comparison of ^{18}F-FHBG uptake in tumors transduced with G1NaGrpTk or G1TkSvNa. (D) Effect of PDT on ^{18}F-FHBG uptake in TSA tumors transduced with G1NaGrpTk [103].

virus env protein (GALV FMG), which mediates cell–cell fusion and results in formation of syncytia when expressed in tumor cells. The median survival time increased from 12.5 (in heated CI1 controls) to 52 days after a single heat treatment [25]. Another original strategy used an antisense RNA to reduce the viability of tumor cells through inhibition of a gene involved in cell repair processes. KU70 forms a heterodimeric complex with KU80 that binds to DNA double-strand breaks and activates DNA-dependent protein kinase involved in DNA repair. An adenovirus vector expressing an antisense KU70 RNA under the control of an HSP70 promoter was used to infect FSA-II tumors. The heat-shock-induced expression of the KU70 antisense RNA attenuated KU70 protein expression in the FSA-II tumors as well as significantly sensitized the tumors to ionizing radiation [106]. The efficiency of the heat-inducible gene therapy approach was also tested using an adenovirus containing a murine IL-12 gene (encoding an antiangiogenic protein) under the control of the HSP70B promoter. Growth of melanoma tumor cell line in C57BL/6 mice was used as the tumor model. Virus injections in combination with a moderate hyperthermia treatment significantly inhibited tumor growth [107]. Taken together, the studies described above have clearly demonstrated the usefulness of HSP promoters for gene therapy *in vivo*.

Nevertheless, the HSP promoter-based gene therapy is still plagued by some unresolved problems, including uncontrolled activation of HSP70 promoters, thermotolerance, and local control of dosage. Besides hyperthermia, HSP70 promoters also respond to other stresses such as oxidative stress, a variety of toxic compounds, hypoxia, ischemia, acidosis, energy depletion, cytokines, and UV radiation [108,109]. Even fever and inflammation may activate a heat shock protein response. Some of these stressors may come into play during the course of a gene therapy procedure and may thus induce unexpected expression of the therapeutic gene. Cells exposed to non-lethal, elevated temperatures become temporarily resistant to a subsequent heat shock. Known as "acquired thermotolerance", this phenomenon is transient in nature and depends on the severity of the initial heat stress. In addition, HSP70 promoter efficiency varies in different cell types. Lastly, differential growth conditions within a tumor could markedly affect expression of a reporter/therapeutic gene [96]. Due to these complications, accurate dosage delivery will be problematic.

For gene therapy to succeed, it requires extensive research to identify the molecular origin of the disease, develop new gene therapy delivery strategies, and improve gene transfer vehicles. Furthermore, precise control of both spatial and temporal expression of the therapeutic transgene is essential. Recent progress in molecular imaging, particularly in the field of imaging gene expression, may help fulfill some of the gene therapy requirements and will likely contribute to the success of this promising therapeutic modality [4]. Typically, the therapeutic gene with expressing vectors will be replaced by or fused with a reporter gene. The spatial and temporal expression of the reporter genes can be visualized and quantitated by non-invasive imaging modalities. Radionuclide-based SPECT or PET imaging and optical imaging are now commonly used imaging strategies for monitoring reporter gene expression.

As a well-established reporter, green fluorescent protein (GFP) has been utilized extensively to evaluate spatial and temporal control of gene expression driven by HSP70 promoters [96,100,107,110]. Under a microscope, in the heating stage that uses green fluorescent protein as a reporter, HSP70 expression kinetics can be visualized continuously in cultured bovine aortic endothelial cells (BAECs). The kinetic profile for HSP70-GFP fusion protein is consistent with the endogenous HSP70 [111]. Although non-invasive imaging in live mice can be achieved by fluorescent imaging, most of these studies still count on fluorescent microscope for more accurate measurement. Due to its low cost, high sensitivity, and excellent temporal

Please cite this article in press as: Niu G, Chen X. From protein–protein interaction to therapy response: Molecular imaging of heat shock proteins. Eur J Radiol (2009), doi:10.1016/j.ejrad.2009.01.052

feasibility, bioluminescent imaging using luciferases as reporter genes has been investigated. Expression of luciferase after local injection of the construct Ad-HSP-Luc (an adenoviral vector containing a transgene encoding firefly luciferase under the control of the human HSP70B promoter) has been induced by magnetic resonance imaging-monitored ultrasound. High levels of luciferase expression were observed only in areas exposed to ultrasonic heating [54]. In this study, the bioluminescent signal was measured by an illuminometer with tissue samples instead of non-invasive BLI imaging.

Nuclear medicine techniques employing different reporter genes and thymidine kinase and sodium iodide symporter (NIS) are among the most widely used PET reporter genes [112–114]. The expression of the reporter gene coding for thymidine kinase can be probed with substrate analogues, including pyrimidine nucleoside derivatives, such as 2′-deoxy-2′-fluoro-β-D-arabinofuranosyl-5-iodouracil (FIAU), and acycloguanosine derivatives, such as 9-[4-fluoro-3-(hydroxymethyl) butyl]guanine (FHBG). GRP78, a member of HSP70 family, is a stress-inducible calcium-binding chaperone protein with anti-apoptotic properties that is highly expressed in cancer cells [115]. The Grp78 promoter has been shown capable of eradicating tumors with murine cells in immunocompetent models by driving the expression of the HSV-tk suicide gene [116]. HSV-tk can be used not only as a therapeutic gene but also a reporter gene. Through the use of PET imaging, researchers have observed the spontaneous *in vivo* activation of the HSV-tk suicide gene driven by the Grp78 promoter in growing tumors and its activation by photodynamic therapy (PDT) in a controlled manner (Fig. 5) [103]. In this study, animals were injected with ^{18}F-FHBG and scanned with a small-animal PET scanner. The brightness of the images depicts HSV-TK activity as it metabolizes and traps the ^{18}F-FHBG substrate intracellularly.

NIS is responsible for the physiologic uptake of iodide. NIS is also able to concentrate pertechnetate (TcO_4^-), bromide (Br^-), and perrhenate (ReO_4^-). With corresponding radionuclides, NIS gene expression can be visualized by SPECT or PET imaging [112]. Che and co-workers [117] have constructed a retroviral vector pQHSP70/hNIS-IRES-eGFP (pQHNIG70) containing the hNIS-IRES-eGFP dual-reporter genes under the control of an inducible human HSP70 promoter. A 2.2- to 6.1-fold $^{131}I^-$, a 6.1- to 14.4-fold $^{99m}TcO_4^-$, and a 5.1- to 39-fold fluorescence increase above baseline were observed in response to graded hyperthermia (39-43 °C). A stable ratio of radiotracer uptake to eGFP fluorescence and to HSP70 protein was demonstrated over a wide range of expression levels, induced by different levels of heating. The local application of heat can effectively induce hNIS and eGFP gene expression *in vivo*; this expression can be efficiently visualized by fluorescence, scintigraphic, and PET imaging. The pQHNIG70 reporter system can be used to study stress and drug responses in transduced cells and tissues [117]. However, it is worth noting that the direct clinical application is limited for most of the reporter genes since this strategy typically requires artificially transduced cells or tissue, which is not feasible under clinical situation.

10. Other applications

Besides imaging transgene expression under control of HSP70 promoter in gene therapy, molecular imaging (especially optical imaging) has been applied to other related fields. For example, screening of microinjected embryos for transgene integration in blastocysts, prior to transfer, would help increase the percentage of positive transgenic fetuses. A luminescent screening system with scaffold attachment regions flanking the murine HSP70.1 promoter linked to firefly luciferase cDNA has been developed to select transgenic bovine embryos. By selecting luminescent blastocysts on the basis of both signal intensity and distribution, the number of recipient females required to produce transgenic offspring can be greatly reduced [118].

Another application is to quantify tissue damage, which has traditionally been evaluated under the macroscope by visual effects such as tissue mass removal, carbonization and melting. Bechham et al. [19] used HSP70 transcription to track cellular response to laser-induced injury. After thermal injury, the onset of bioluminescence in a stable cell line (NIH-3T3) containing the firefly luciferase reporter gene attached to the HSP promoter (murine HSP70a1) can be seen as early as 2 h after treatment and usually peaks at 8–12 h, depending on the severity of heat shock. Bioluminescence levels correlated well with actual HSP70 protein concentrations as determined by enzyme-linked immunosorbent assay (ELISA). Quantitative BLI in engineered tissue equivalents provides a powerful model that enables sequential gene expression studies. Such a model can be used as a high-throughput screening platform for laser-tissue interaction studies [119]. Lastly, compared with conventional organic dyes, quantum dots (QDs) have several advantages, including their narrow, symmetrical and tunable emission spectra, excellent photostablility, and broad absorption spectra [120]. Labeling Mortalin/mtHSP70 and HSP60 by quantum dots with different emission wavelengths, Kaul et al. [121] visualized minute differences in the subcellular niche of quantum dots labeled in normal and cancer cells.

11. Summary and perspectives

The HSP70 promoter-driven gene therapy and inhibition of HSP90 activity with small molecule inhibitors are two shining points in the newly developed cohort of cancer treatment. For HSP70 promoters, high efficiency and heat inducibility within a localized region make it very attractive to clinical translation. Initially, GFP was used as a reporter gene to analyze the pattern and efficiency of HSP70 promoter controlled transgene expression. Recently, bioluminescent and PET reporter genes have been introduced to provide better non-invasive and real time evaluation of this gene therapeutic strategy. These molecular imaging techniques will facilitate investigation of more powerful promoters, a new generation of carriers, and the localized hyperthermal dose delivery of HSP70 promoters controlled gene therapy. However, non-invasive imaging cannot yet fully replace the corresponding traditional research methods, though *in vivo* imaging can provide more comprehensive and longitudinal observation within an intact organism (usually whole body). For instance, in one of the aforementioned studies, luciferase activity was measured by an illuminometer with minced tissue samples instead of BLI imaging because BLI imaging could *not* provide enough spatial resolution to distinguish gene expression pattern among the different region within the organ (prostate gland in this case) [54].

HSP90 inhibitors exhibit a broad spectrum of anticancer activities because the downstream effects of HSP90 inhibition affect a wide range of signaling processes that are crucial for the malignant properties of cancer cells. Molecular imaging methods have been developed to screen drugs and monitor the therapeutic response of HSP90 inhibitors. However, most of these strategies are based on imaging changes of client proteins such as HER2 and EGFR. These proteins are on the cell surface, making them more accessible. A drawback of these imaging is that the availability, expression level, and response to HSP90 inhibitors of these client proteins can vary in different cancer types. One way to overcome this obstacle is to monitor several client proteins together, which will provide a more comprehensive evaluation of tumor's response to HSP90 inhibition. For example, androgen receptor (AR) is another client protein which is usually highly expressed in prostate cancer. The PET imaging probes targeting AR is now in development for *in vivo* imaging of tissue AR distribution [122]. In prostate cancers with low

Please cite this article in press as: Niu G, Chen X. From protein–protein interaction to therapy response: Molecular imaging of heat shock proteins. Eur J Radiol (2009), doi:10.1016/j.ejrad.2009.01.052

levels of HER2 expression, EGFR and AR can be imaged simultaneously or in a row to provide an early evaluation of HSP90 inhibition. Another promising alternative is to image HSP90 activity directly with small molecule probes that can penetrate the cell membrane and bind with HSP90. With optimized linker and radionuclides, PET can be applied to visualize and quantify HSP90 activity directly. In the coming years, these novel imaging techniques are expected to prove their worth in drug development, patient selection, and tumor response monitoring.

Acknowledgments

Research carried out in the authors' laboratory was supported, in part, by the NCI P50 CA114747 and a DOD Prostate Postdoctoral Fellowship from Department of Defense (G. Niu).

References

[1] Mankoff DA. A definition of molecular imaging. J Nucl Med 2007;48(6):18N–21N.
[2] Massoud TF, Gambhir SS. Molecular imaging in living subjects: seeing fundamental biological processes in a new light. Genes Dev 2003;17(5):545–80.
[3] Mather SJ. Design of radiolabelled ligands for the imaging and treatment of cancer. Mol Biosyst 2007;3(1):30–5.
[4] Wunderbaldinger P, Bogdanov A, Weissleder R. New approaches for imaging in gene therapy. Eur J Radiol 2000;34(3):156–65.
[5] Jones T. The imaging science of positron emission tomography. Eur J Nucl Med 1996;23(7):807–13.
[6] Chatziioannou AF. Instrumentation for molecular imaging in preclinical research: Micro-PET and Micro-SPECT. Proc Am Thorac Soc 2005;2(6):533–6, 10–11.
[7] Pathak AP, Gimi B, Glunde K, Ackerstaff E, Artemov D, Bhujwalla ZM. Molecular and functional imaging of cancer: advances in MRI and MRS. Methods Enzymol 2004;386:3–60.
[8] Wink MH, Wijkstra H, De La Rosette JJ, Grimbergen CA. Ultrasound imaging and contrast agents: a safe alternative to MRI? Minim Invasive Ther Allied Technol 2006;15(2):93–100.
[9] Bloch SH, Dayton PA, Ferrara KW. Targeted imaging using ultrasound contrast agents, progress and opportunities for clinical and research applications. IEEE Eng Med Biol Mag 2004;23(5):18–29.
[10] Cosgrove D. Ultrasound contrast agents: an overview. Eur J Radiol 2006;60(3):324–30.
[11] Hjorth-Sorensen B, Hoffmann ER, Lissin NM, Sewell AK, Jakobsen BK. Activation of heat shock transcription factor in yeast is not influenced by the levels of expression of heat shock proteins. Mol Microbiol 2001;39(4):914–23.
[12] Mortele KJ, McTavish J, Ros PR. Current techniques of computed tomography. Helical CT, multidetector CT, and 3D reconstruction. Clin Liver Dis 2002;6(1):29–52.
[13] Jain RK, Munn LL, Fukumura D. Dissecting tumour pathophysiology using intravital microscopy. Nat Rev Cancer 2002;2(4):266–76.
[14] Zipfel WR, Williams RM, Webb WW. Nonlinear magic: multiphoton microscopy in the biosciences. Nat Biotechnol 2003;21(11):1369–77.
[15] Papaconstantinou AD, Fisher BR, Umbreit TH, Goering PL, Lappas NT, Brown KM. Effects of beta-estradiol and bisphenol A on heat shock protein levels and localization in the mouse uterus are antagonized by the antiestrogen ICI 182 780. Toxicol Sci 2001;63(2):173–80.
[16] Kunneke S, Janshoff A. Visualization of molecular recognition events on microstructured lipid-membrane compartments by in situ scanning force microscopy. Angew Chem Int Ed Engl 2002;41(2):314–6.
[17] Mazlumzadeh M, Lowe VJ, Mullan BP, Fabry DA, McDonald TJ, Matteson EL. The utility of positron emission tomography in the evaluation of autoimmune hearing loss. Otol Neurotol 2003;24(2):201–4.
[18] van Roessel P, Brand AH. Imaging into the future: visualizing gene expression and protein interactions with fluorescent proteins. Nat Cell Biol 2002;4(1):E15–20.
[19] Beckham JT, Mackanos MA, Crooke C, et al. Assessment of cellular response to thermal laser injury through bioluminescence imaging of heat shock protein 70. Photochem Photobiol 2004;79(1):76–85.
[20] Lipshutz GS, Flebbe-Rehwaldt L, Gaensler KM. Reexpression following readministration of an adenoviral vector in adult mice after initial in utero adenoviral administration. Mol Ther 2000;2(4):374–80.
[21] Szwaya J, Bruseo C, Nakuci E, et al. A novel platform for accelerated pharmacodynamic profiling for lead optimization of anticancer drug candidates. J Biomol Screen 2007;12(2):159–66.
[22] Chan CT, Paulmurugan R, Gheysens OS, Kim J, Chiosis G, Gambhir SS. Molecular imaging of the efficacy of heat shock protein 90 inhibitors in living subjects. Cancer Res 2008;68(1):216–26.
[23] De A, Gambhir SS. Noninvasive imaging of protein–protein interactions from live cells and living subjects using bioluminescence resonance energy transfer. FASEB J 2005;19(14):2017–9.
[24] Cao X, Jia G, Zhang T, et al. Non-invasive MRI tumor imaging and synergistic anticancer effect of HSP90 inhibitor and glycolysis inhibitor in RIP1-Tag2 transgenic pancreatic tumor model. Cancer Chemother Pharmacol 2008.
[25] Shi Y, Mosser DD, Morimoto RI. Molecular chaperones as HSF1-specific transcriptional repressors. Genes Dev 1998;12(5):654–66.
[26] Bukau B, Horwich AL. The Hsp70 and Hsp60 chaperone machines. Cell 1998;92(3):351–66.
[27] Bukau B, Weissman J, Horwich A. Molecular chaperones and protein quality control. Cell 2006;125(3):443–51.
[28] Wegele H, Muller L, Buchner J. Hsp70 and Hsp90—a relay team for protein folding. Rev Physiol Biochem Pharmacol 2004;151:1–44.
[29] Pratt WB, Toft DO. Regulation of signaling protein function and trafficking by the hsp90/hsp70-based chaperone machinery. Exp Biol Med (Maywood) 2003;228(2):111–33.
[30] Hut HM, Kampinga HH, Sibon OC. Hsp70 protects mitotic cells against heat-induced centrosome damage and division abnormalities. Mol Biol Cell 2005;16(8):3776–85.
[31] Beere HM. Stressed to death: regulation of apoptotic signaling pathways by the heat shock proteins. Sci STKE 2001;2001(93):RE1.
[32] Calderwood SK. Regulatory interfaces between the stress protein response and other gene expression programs in the cell. Methods 2005;35(2):139–48.
[33] Nollen EA, Morimoto RI. Chaperoning signaling pathways: molecular chaperones as stress-sensing 'heat shock' proteins. J Cell Sci 2002;115(Pt 14):2809–16.
[34] Dutta R, Inouye M. GHKL, an emergent ATPase/kinase superfamily. Trends Biochem Sci 2000;25(1):24–8.
[35] Jakob U, Lilie H, Meyer I, Buchner J. Transient interaction of Hsp90 with early unfolding intermediates of citrate synthase, implications for heat shock in vivo. J Biol Chem 1995;270(13):7288–94.
[36] Solit DB, Zheng FF, Drobnjak M, et al. 17-Allylamino-17-demethoxygeldanamycin induces the degradation of androgen receptor and HER-2/neu and inhibits the growth of prostate cancer xenografts. Clin Cancer Res 2002;8(5):986–93.
[37] Basso AD, Solit DB, Munster PN, Rosen N. Ansamycin antibiotics inhibit Akt activation and cyclin D expression in breast cancer cells that overexpress HER2. Oncogene 2002;21(8):1159–66.
[38] Blagosklonny MV, Toretsky J, Bohen S, Neckers L. Mutant conformation of p53 translated in vitro or in vivo requires functional HSP90. Proc Natl Acad Sci USA 1996;93(16):8379–83.
[39] Nadeau K, Das A, Walsh CT. Hsp90 chaperonins possess ATPase activity and bind heat shock transcription factors and peptidyl prolyl isomerases. J Biol Chem 1993;268(2):1479–87.
[40] Neckers L, Ivy SP. Heat shock protein 90. Curr Opin Oncol 2003;15(6):419–24.
[41] Clarke PA, Hostein I, Banerji U, et al. Gene expression profiling of human colon cancer cells following inhibition of signal transduction by 17-allylamino-17-demethoxygeldanamycin, an inhibitor of the hsp90 molecular chaperone. Oncogene 2000;19(36):4125–33.
[42] Burrows F, Zhang H, Kamal A. Hsp90 activation and cell cycle regulation. Cell Cycle 2004;3(12):1530–6.
[43] Eustace BK, Sakurai T, Stewart JK, et al. Functional proteomic screens reveal an essential extracellular role for hsp90 alpha in cancer cell invasiveness. Nat Cell Biol 2004;6(6):507–14.
[44] Kamal A, Thao L, Sensintaffar J, et al. A high-affinity conformation of Hsp90 confers tumour selectivity on Hsp90 inhibitors. Nature 2003;425(6956):407–10.
[45] Mosser DD, Morimoto RI. Molecular chaperones and the stress of oncogenesis. Oncogene 2004;23(16):2907–18.
[46] Nimmanapalli R, O'Bryan E, Bhalla K. Geldanamycin and its analogue 17-allylamino-17-demethoxygeldanamycin lowers Bcr-Abl levels and induces apoptosis and differentiation of Bcr-Abl-positive human leukemic blasts. Cancer Res 2001;61(5):1799–804.
[47] Rutherford SL, Lindquist S. Hsp90 as a capacitor for morphological evolution. Nature 1998;396(6709):336–42.
[48] Sollars V, Lu X, Xiao L, Wang X, Garfinkel MD, Ruden DM. Evidence for an epigenetic mechanism by which Hsp90 acts as a capacitor for morphological evolution. Nat Genet 2003;33(1):70–4.
[49] Schneider C, Sepp-Lorenzino L, Nimmesgern E, et al. Pharmacologic shifting of a balance between protein refolding and degradation mediated by Hsp90. Proc Natl Acad Sci USA 1996;93(25):14536–41.
[50] Whitesell L, Cook P. Stable and specific binding of heat shock protein 90 by geldanamycin disrupts glucocorticoid receptor function in intact cells. Mol Endocrinol 1996;10(6):705–12.
[51] Roe SM, Prodromou C, O'Brien R, Ladbury JE, Piper PW, Pearl LH. Structural basis for inhibition of the Hsp90 molecular chaperone by the antitumor antibiotics radicicol and geldanamycin. J Med Chem 1999;42(2):260–6.
[52] An WG, Schulte TW, Neckers LM. The heat shock protein 90 antagonist geldanamycin alters chaperone association with p210bcr-abl and v-src proteins before their degradation by the proteasome. Cell Growth Differ 2000;11(7):355–60.
[53] Kelland LR, Sharp SY, Rogers PM, Myers TG, Workman P. DT-Diaphorase expression and tumor cell sensitivity to 17-allylamino, 17-demethoxygeldanamycin, an inhibitor of heat shock protein 90. J Natl Cancer Inst 1999;91(22):1940–9.
[54] Silcox CE, Smith RC, King R, et al. MRI-guided ultrasonic heating allows spatial control of exogenous luciferase in canine prostate. Ultrasound Med Biol 2005;31(7):965–70.

Please cite this article in press as: Niu G, Chen X. From protein–protein interaction to therapy response: Molecular imaging of heat shock proteins. Eur J Radiol (2009), doi:10.1016/j.ejrad.2009.01.052

[55] Chiosis G, Huezo H, Rosen N, Mimnaugh E, Whitesell L, Neckers L. 17AAG: low target binding affinity and potent cell activity—finding an explanation. Mol Cancer Ther 2003;2(2):123–9.
[56] Kim J, Felts S, Llauger L, et al. Development of a fluorescence polarization assay for the molecular chaperone Hsp90. J Biomol Screen 2004;9(5):375–81.
[57] Gooljarsingh LT, Fernandes C, Yan K, et al. A biochemical rationale for the anticancer effects of Hsp90 inhibitors: slow, tight binding inhibition by geldanamycin and its analogues. Proc Natl Acad Sci USA 2006;103(20):7625–30.
[58] Maroney AC, Marugan JJ, Mezzasalma TM, et al. Dihydroquinone ansamycins: toward resolving the conflict between low in vitro affinity and high cellular potency of geldanamycin derivatives. Biochemistry 2006;45(17):5678–85.
[59] Lee YS, Marcu MG, Neckers L. Quantum chemical calculations and mutational analysis suggest heat shock protein 90 catalyzes trans–cis isomerization of geldanamycin. Chem Biol 2004;11(7):991–8.
[60] Onuoha SC, Mukund SR, Coulstock ET, et al. Mechanistic studies on Hsp90 inhibition by ansamycin derivatives. J Mol Biol 2007;372(2):287–97.
[61] Panaretou B, Prodromou C, Roe SM, et al. ATP binding and hydrolysis are essential to the function of the Hsp90 molecular chaperone in vivo. EMBO J 1998;17(16):4829–36.
[62] Obermann WM, Sondermann H, Russo AA, Pavletich NP, Hartl FU. In vivo function of Hsp90 is dependent on ATP binding and ATP hydrolysis. J Cell Biol 1998;143(4):901–10.
[63] Llauger-Bufi L, Felts SJ, Huezo H, Rosen N, Chiosis G. Synthesis of novel fluorescent probes for the molecular chaperone Hsp90. Bioorg Med Chem Lett 2003;13(22):3975–8.
[64] Whitesell L, Mimnaugh EG, De Costa B, Myers CE, Neckers LM. Inhibition of heat shock protein HSP90-pp60v-src heteroprotein complex formation by benzoquinone ansamycins: essential role for stress proteins in oncogenic transformation. Proc Natl Acad Sci USA 1994;91(18):8324–8.
[65] Chiosis G, Lucas B, Shtil A, Huezo H, Rosen N. Development of a purine-scaffold novel class of Hsp90 binders that inhibit the proliferation of cancer cells and induce the degradation of Her2 tyrosine kinase. Bioorg Med Chem 2002;10(11):3555–64.
[66] Carreras CW, Schirmer A, Zhong Z, Santi DV. Filter binding assay for the geldanamycin-heat shock protein 90 interaction. Anal Biochem 2003;317(1):40–6.
[67] Moulick K, Clement CC, Aguirre J, et al. Synthesis of a red-shifted fluorescence polarization probe for Hsp90. Bioorg Med Chem Lett 2006;16(17):4515–8.
[68] Thulasiraman V, Matts RL. Effect of geldanamycin on the kinetics of chaperone-mediated renaturation of firefly luciferase in rabbit reticulocyte lysate. Biochemistry 1996;35(41):13443–50.
[69] Galam L, Hadden MK, Ma Z, et al. High-throughput assay for the identification of Hsp90 inhibitors based on Hsp90-dependent refolding of firefly luciferase. Bioorg Med Chem 2007;15(5):1939–46.
[70] Piehler J. New methodologies for measuring protein interactions in vivo and in vitro. Curr Opin Struct Biol 2005;15(1):4–14.
[71] Ha T, Enderle T, Ogletree DF, Chemla DS, Selvin PR, Weiss S. Probing the interaction between two single molecules: fluorescence resonance energy transfer between a single donor and a single acceptor. Proc Natl Acad Sci USA 1996;93(13):6264–8.
[72] Xu Y, Piston DW, Johnson CH. A bioluminescence resonance energy transfer (BRET) system: application to interacting circadian clock proteins. Proc Natl Acad Sci USA 1999;96(1):151–6.
[73] Hu CD, Chinenov Y, Kerppola TK. Visualization of interactions among bZIP and Rel family proteins in living cells using bimolecular fluorescence complementation. Mol Cell 2002;9(4):789–98.
[74] Picard D. Intracellular dynamics of the Hsp90 co-chaperone p23 is dictated by Hsp90. Exp Cell Res 2006;312(2):198–204.
[75] Picard D, Suslova E, Briand PA. 2-color photobleaching experiments reveal distinct intracellular dynamics of two components of the Hsp90 complex. Exp Cell Res 2006;312(19):3949–58.
[76] Luker KE, Smith MC, Luker GD, Gammon ST, Piwnica-Worms H, Piwnica-Worms D. Kinetics of regulated protein–protein interactions revealed with firefly luciferase complementation imaging in cells and living animals. Proc Natl Acad Sci USA 2004;101(33):12288–93.
[77] Chen H, Zou Y, Shang Y, et al. Firefly luciferase complementation imaging assay for protein–protein interactions in plants. Plant Physiol 2008;146(2):368–76.
[78] Workman P, Kaye SB. Translating basic cancer research into new cancer therapeutics. Trends Mol Med 2002;8(4 Suppl):S1–9.
[79] Massoud TF, Gambhir SS. Integrating noninvasive molecular imaging into molecular medicine: an evolving paradigm. Trends Mol Med 2007;13(5):183–91.
[80] Citri A, Alroy I, Lavi S, et al. Drug-induced ubiquitylation and degradation of ErbB receptor tyrosine kinases: implications for cancer therapy. EMBO J 2002;21(10):2407–17.
[81] Traish AM, Wotiz HH. Prostatic epidermal growth factor receptors and their regulation by androgens. Endocrinology 1987;121(4):1461–7.
[82] Hofer DR, Sherwood ER, Bromberg WD, Mendelsohn J, Lee C, Kozlowski JM. Autonomous growth of androgen-independent human prostatic carcinoma cells: role of transforming growth factor alpha. Cancer Res 1991;51(11):2780–5.
[83] Niu G, Cai W, Chen X. Molecular imaging of human epidermal growth factor receptor 2 (HER-2) expression. Front Biosci 2008;13:790–805.
[84] Cai W, Niu G, Chen X. Multimodality imaging of the HER-kinase axis in cancer. Eur J Nucl Med Mol Imaging 2008;35(1):186–208.
[85] Smith-Jones PM, Solit DB, Akhurst T, Afroze F, Rosen N, Larson SM. Imaging the pharmacodynamics of HER2 degradation in response to Hsp90 inhibitors. Nat Biotechnol 2004;22(6):701–6.
[86] Smith-Jones PM, Solit D, Afroze F, Rosen N, Larson SM. Early tumor response to Hsp90 therapy using HER2 PET: comparison with 18F-FDG PET. J Nucl Med 2006;47(5):793–6.
[87] Solit DB, Rosen N. Hsp90: a novel target for cancer therapy. Curr Top Med Chem 2006;6(11):1205–14.
[88] Murakami Y, Mizuno S, Uehara Y. Accelerated degradation of 160 kDa epidermal growth factor (EGF) receptor precursor by the tyrosine kinase inhibitor herbimycin A in the endoplasmic reticulum of A431 human epidermoid carcinoma cells. Biochem J 1994;301(Pt 1):63–8.
[89] Sakagami M, Morrison P, Welch WJ. Benzoquinoid ansamycins (herbimycin A and geldanamycin) interfere with the maturation of growth factor receptor tyrosine kinases. Cell Stress Chaperones 1999;4(1):19–28.
[90] Cai W, Chen K, He L, Cao Q, Koong A, Chen X. Quantitative PET of EGFR expression in xenograft-bearing mice using ^{64}Cu-labeled cetuximab, a chimeric anti-EGFR monoclonal antibody. Eur J Nucl Med Mol Imaging 2007;34(6):850–8.
[91] Ciardiello F, Damiano V, Bianco R, et al. Antitumor activity of combined blockade of epidermal growth factor receptor and protein kinase A. J Natl Cancer Inst 1996;88(23):1770–6.
[92] Niu G, Cai W, Chen K, Chen X. Non-invasive PET imaging of EGFR degradation induced by a heat shock protein 90 inhibitor. Mol Imaging Biol 2008;10(2):99–106.
[93] Rome C, Couillaud F, Moonen CT. Spatial and temporal control of expression of therapeutic genes using heat shock protein promoters. Methods 2005;35(2):188–98.
[94] Fernandes M, Xiao H, Lis JT. Binding of heat shock factor to and transcriptional activation of heat shock genes in Drosophila. Nucleic Acids Res 1995;23(23):4799–804.
[95] Milner CM, Campbell RD. Structure and expression of the three MHC-linked HSP70 genes. Immunogenetics 1990;32(4):242–51.
[96] Borrelli MJ, Schoenherr DM, Wong A, Bernock LJ, Corry PM. Heat-activated transgene expression from adenovirus vectors infected into human prostate cancer cells. Cancer Res 2001;61(3):1113–21.
[97] Brade AM, Ngo D, Szmitko P, Li PX, Liu FF, Klamut HJ. Heat-directed gene targeting of adenoviral vectors to tumor cells. Cancer Gene Ther 2000;7(12):1566–74.
[98] Yang ZF, Poon RT, Luo Y, et al. Up-regulation of vascular endothelial growth factor (VEGF) in small-for-size liver grafts enhances macrophage activities through VEGF receptor 2-dependent pathway. J Immunol 2004;173(4):2507–15.
[99] Gerner EW, Hersh EM, Pennington M, et al. Heat-inducible vectors for use in gene therapy. Int J Hyperthermia 2000;16(2):171–81.
[100] Guilhon E, Quesson B, Moraud-Gaudry F, et al. Image-guided control of transgene expression based on local hyperthermia. Mol Imaging 2003;2(1):11–7.
[101] Guilhon E, Voisin P, de Zwart JA, et al. Spatial and temporal control of transgene expression in vivo using a heat-sensitive promoter and MRI-guided focused ultrasound. J Gene Med 2003;5(4):333–42.
[102] Blackburn RV, Galoforo SS, Corry PM, Lee YJ. Adenoviral-mediated transfer of a heat-inducible double suicide gene into prostate carcinoma cells. Cancer Res 1998;58(7):1358–62.
[103] Dong D, Dubeau L, Bading J, et al. Spontaneous and controllable activation of suicide gene expression driven by the stress-inducible grp78 promoter resulting in eradication of sizable human tumors. Hum Gene Ther 2004;15(6):553–61.
[104] Braiden V, Ohtsuru A, Kawashita Y, et al. Eradication of breast cancer xenografts by hyperthermic suicide gene therapy under the control of the heat shock protein promoter. Hum Gene Ther 2000;11(18):2453–63.
[105] Brade AM, Szmitko P, Ngo D, Liu FF, Klamut HJ. Heat-directed suicide gene therapy for breast cancer. Cancer Gene Ther 2003;10(4):294–301.
[106] Li GC, He F, Shao X, et al. Adenovirus-mediated heat-activated antisense Ku70 expression radiosensitizes tumor cells in vitro and in vivo. Cancer Res 2003;63(12):3268–74.
[107] Huang Q, Hu JK, Lohr F, et al. Heat-induced gene expression as a novel targeted cancer gene therapy strategy. Cancer Res 2000;60(13):3435–9.
[108] Freeman ML, Borrelli MJ, Syed K, Senisterra G, Stafford DM, Lepock JR. Characterization of a signal generated by oxidation of protein thiols that activates the heat shock transcription factor. J Cell Physiol 1995;164(2):356–66.
[109] Kregel KC. Heat shock proteins: modifying factors in physiological stress responses and acquired thermotolerance. J Appl Physiol 2002;92(5):2177–86.
[110] Vekris A, Maurange C, Moonen C, et al. Control of transgene expression using local hyperthermia in combination with a heat-sensitive promoter. J Gene Med 2000;2(2):89–96.
[111] Wang S, Xie W, Rylander MN, Tucker PW, Aggarwal S, Diller KR. HSP70 kinetics study by continuous observation of HSP-GFP fusion protein expression on a perfusion heating stage. Biotechnol Bioeng 2008;99(1):146–54.
[112] Niu G, Gaut AW, Ponto LL, et al. Multimodality noninvasive imaging of gene transfer using the human sodium iodide symporter. J Nucl Med 2004;45(3):445–9.
[113] Niu G, Krager KJ, Graham MM, Hichwa RD, Domann FE. Noninvasive radiological imaging of pulmonary gene transfer and expression using the human sodium iodide symporter. Eur J Nucl Med Mol Imaging 2005;32(5):534–40.

Please cite this article in press as: Niu G, Chen X. From protein–protein interaction to therapy response: Molecular imaging of heat shock proteins. Eur J Radiol (2009), doi:10.1016/j.ejrad.2009.01.052

[114] Liang Q, Nguyen K, Satyamurthy N, et al. Monitoring adenoviral DNA delivery, using a mutant herpes simplex virus type 1 thymidine kinase gene as a PET reporter gene. Gene Ther 2002;9(24):1659–66.
[115] Lee YJ, Curetty L, Hou ZZ, Kim SH, Kim JH, Corry PM. Effect of pH on quercetin-induced suppression of heat shock gene expression and thermotolerance development in HT-29 cells. Biochem Biophys Res Commun 1992;186(2):1121–8.
[116] Luna MC, Chen X, Wong S, et al. Enhanced photodynamic therapy efficacy with inducible suicide gene therapy controlled by the grp promoter. Cancer Res 2002;62(5):1458–61.
[117] Che J, Doubrovin M, Serganova I, et al. HSP70-inducible hNIS-IRES-eGFP reporter imaging: response to heat shock. Mol Imaging 2007;6(6):404–16.
[118] Menck M, Mercier Y, Campion E, et al. Prediction of transgene integration by noninvasive bioluminescent screening of microinjected bovine embryos. Transgenic Res 1998;7(5):331–41.
[119] Wilmink GJ, Opalenik SR, Beckham JT, Davidson JM, Jansen ED. Assessing laser-tissue damage with bioluminescent imaging. J Biomed Opt 2006;11(4):041114.
[120] Bruchez M, Moronne M, Gin P, Weiss S, Alivisatos AP. Semiconductor nanocrystals as fluorescent biological labels. Science 1998;281(5385):2013–6.
[121] Densmore JC, Signorino PR, Ou J, et al. Endothelium-derived microparticles induce endothelial dysfunction and acute lung injury. Shock 2006;26(5):464–71.
[122] Garg S, Doke A, Black KW, Garg PK. In vivo biodistribution of an androgen receptor avid PET imaging agent 7-alpha-fluoro-17 alpha-methyl-5-alpha-dihydrotestosterone ([(18)F]FMDHT) in rats pretreated with cetrorelix, a GnRH antagonist. Eur J Nucl Med Mol Imaging 2008;35(2):379–85.
[123] Zhao R, Houry WA. Hsp90: a chaperone for protein folding and gene regulation. Biochem Cell Biol 2005;83(6):703–10.

Please cite this article in press as: Niu G, Chen X. From protein–protein interaction to therapy response: Molecular imaging of heat shock proteins. Eur J Radiol (2009), doi:10.1016/j.ejrad.2009.01.052

Eur J Nucl Med Mol Imaging
DOI 10.1007/s00259-009-1158-1

ORIGINAL ARTICLE

Monitoring therapeutic response of human ovarian cancer to 17-DMAG by noninvasive PET imaging with ^{64}Cu-DOTA-trastuzumab

Gang Niu · Zibo Li · Qizhen Cao · Xiaoyuan Chen

Received: 9 February 2009 / Accepted: 17 April 2009
© Springer-Verlag 2009

Abstract
Purpose 17-Dimethylaminoethylamino-17-demethoxygeldanamycin (17-DMAG), a heat-shock protein 90 (Hsp90) inhibitor, has been intensively investigated for cancer therapy and is undergoing clinical trials. Human epidermal growth factor receptor 2 (HER-2) is one of the client proteins of Hsp90 and its expression is decreased upon 17-DMAG treatment. In this study, we aimed to noninvasively monitor the HER-2 response to 17-DMAG treatment in xenografted mice.
Methods The sensitivity of human ovarian cancer SKOV-3 cells to 17-DMAG in vitro was measured by MTT assay. HER-2 expression in SKOV-3 cells was determined by flow cytometry. Nude mice bearing SKOV-3 tumors were treated with 17-DMAG and the therapeutic efficacy was evaluated by tumor size measurement. Both treated and control mice were imaged with microPET using ^{64}Cu-DOTA-trastuzumab and ^{18}F-FDG. Biodistribution studies and immunofluorescence staining were performed to validate the microPET results.
Results SKOV-3 cells are sensitive to 17-DMAG treatment, in a dose-dependent manner, with an IC_{50} value of 24.72 nM after 72 h incubation. The tumor growth curve supported the inhibition effect of 17-DMAG on SKOV-3 tumors. Quantitative microPET imaging showed that ^{64}Cu-DOTA-trastuzumab had prominent tumor accumulation in untreated SKOV-3 tumors, which was significantly reduced in 17-DMAG-treated tumors. There was no uptake difference detected by FDG PET. Immunofluorescence staining confirmed the significant reduction in tumor HER-2 level upon 17-DMAG treatment.
Conclusion The early response to anti-Hsp90 therapy was successfully monitored by quantitative PET using ^{64}Cu-DOTA-trastuzumab. This approach may be valuable in monitoring the therapeutic response in HER-2-positive cancer patients under 17-DMAG treatment.

Keywords Human epidermal growth factor receptor (HER-2) · Positron emission tomography (PET) · Heat-shock protein 90 (Hsp90) · 17-dimethylaminoethylamino-17-demethoxygeldanamycin (17-DMAG) · Trastuzumab

Introduction

The chaperone heat-shock protein 90 (Hsp90) has recently emerged as a promising target for cancer therapy [1]. The unique characteristic of Hsp90 lies in the fact that it targets a specific set of client proteins that are mainly involved in signal transduction pathways [2]. Hsp90 has been reported to play an important role in the progress of malignant disease, and elevated Hsp90 levels have been observed in a variety of cancers, including breast, brain, colon, and lung [3, 4]. Hsp90 inhibitors, such as the benzoquinone ansamycin antibiotic geldanamycin (GA), inhibit the activity of Hsp90 and further disrupt the proper conformation of the client proteins of Hsp90, including epidermal growth factor receptor 2 (HER-2), epidermal growth factor

G. Niu · Z. Li · Q. Cao · X. Chen (✉)
The Molecular Imaging Program at Stanford (MIPS),
Department of Radiology and Bio-X Program,
Stanford University School of Medicine,
1201 Welch Rd, P095,
Stanford, CA 94305-5484, USA
e-mail: shawchen@stanford.edu

Z. Li
USC Molecular Imaging Center, Department of Radiology,
Keck School of Medicine,
Los Angeles, CA, USA

Published online: 14 May 2009

receptor (EGFR), Akt, and wild-type and mutated androgen receptors (AR) [5–7].

HER-2, also known as ErbB-2 (erythroblastic leukemia viral oncogene homolog 2), is a cell membrane surface-bound receptor tyrosine kinase [8]. Overexpression of HER-2 increases cell proliferation, anchorage-independent cell growth, cell migration, and invasiveness [9–11]. HER-2 overexpression is detected in up to 30% of breast and ovarian cancers [12]. Overexpression of HER-2 has been correlated with invasive and poor prognostic features [13]. HER-2 is dependent upon Hsp90 for its stability throughout the whole life span of the receptor, including the maturation process in the ER, and during the residency of the receptor at the plasma membrane [14]. Consequently, the degradation of HER-2 upon inactivation of Hsp90 occurs from both the ER and the plasma membrane [15].

17-Allylamino-17-demthoxygeldanamycin (17-AAG) is an Hsp90 inhibitor derived from GA. Both preclinical and phase I clinical studies of 17-AAG have shown that biologically relevant drug exposures can be achieved with surprisingly modest toxicity [16, 17]. However, the water solubility of 17-AAG is very poor, only around 50 μg /ml. Thus, it requires the addition of organic excipients such as dimethyl sulfoxide (DMSO) or polyoxyl castor oil (Cremophor) [18]. Clinical trials with 17-AAG in these excipients may confound the true maximum tolerated dose of 17-AAG and identification of the optimal dosing regimen in patients. Indeed, with low doses of 17-AAG in DMSO, there was no objective antitumor responses observed in several phase II trials including melanoma, hormone-refractory prostate cancer, and renal cell carcinoma [19, 20]. By modifying the side group, a more water-soluble analog, 17-dimethylaminoethylamino-17-demethoxygeldanamycin (17-DMAG), has been developed and shown antitumor activity in human tumor xenograft models [21, 22]. 17-DMAG is currently in phase I/II clinical trials [23].

The assessment of early response to anticancer therapy can improve patient care by identifying the only responding patients to continue the treatment. Those who do not respond and therefore may not benefit from the therapy will be able to avoid unnecessary toxic side effects and switch to different, more effective therapeutic approaches in a timely manner [24]. Since HER-2 is a key client protein of Hsp90, analyzing the expression status of HER-2 will be of great help in antitumor therapy with Hsp90 inhibitors including 17-DMAG. Traditionally, analyzing HER-2 overexpression in surgical specimens is most commonly accomplished by either immunohistochemical (IHC) staining or fluorescence in situ hybridization (FISH) testing [25, 26]. Despite the preselection for HER-2 overexpression based on IHC staining or FISH of a tumor biopsy, only 11–35% of patients in phase II trials responded to trastuzumab when it was given as a single agent [27]. Alternatively, various noninvasive molecular imaging modalities are under intensive investigation to provide the comprehensive diagnostic information that can improve patient management [28].

Trastuzumab is a recombinant humanized anti-HER-2 monoclonal antibody developed by inserting the complementary determining regions (CDRs) of mAb 4D5 into the framework of a consensus human IgG [29, 30]. Trastuzumab has been labeled with various isotopes, chromophores, and paramagnetic nanoparticles for multimodality imaging of HER-2 expression [31, 32]. With ^{111}In-labeled trastuzumab, HER-2-positive SKOV-3 tumor was clearly visualized on gamma camera scintigram imaged 72 h after injection [33]. In this study, we treated the human ovarian cancer SKOV-3 xenograft model with 17-DMAG. After treatment, ^{64}Cu-DOTA-trastuzumab PET imaging was performed to monitor HER-2 degradation. The goal of this study was to determine whether PET imaging with ^{64}Cu-DOTA-trastuzumab, a HER-2 targeted tracer, could be used to evaluate the expression level of HER-2 and to further monitor the early response of HER-2 degradation upon anti-Hsp90 therapy with 17-DMAG.

Materials and methods

All commercially available chemical reagents were used without further purification. 1,4,7,10-Tetraazadodecane-N,N′,N″,N‴-tetraacetic acid (DOTA) was purchased from Macrocyclics, Inc. (Dallas, TX, USA) and Chelex 100 resin (50–100 mesh) was purchased from Aldrich (St. Louis, MO, USA). Water and all buffers were passed through a Chelex 100 column (1×15 cm) before use in radiolabeling procedures to ensure that the aqueous buffer is heavy metal free. PD-10 desalting columns were purchased from GE Healthcare (Piscataway, NJ, USA). Athymic nude mice were obtained from Harlan (Indianapolis, IN, USA) at 4–6 weeks of age. ^{64}Cu was provided by the University of Wisconsin-Madison. The human ovarian cancer SKOV-3 cell line was obtained from the American Type Culture Collection (ATCC) and maintained in DMEM medium supplemented with 10% fetal bovine serum (FBS), 1% glutamine, 100 U/ml penicillin, and 100 mg/ml streptomycin (Invitrogen, Carlsbad, CA, USA).

MTT assay

The toxicity of 17-DMAG to SKOV-3 cells was determined by MTT assay. All studies were performed with triplicate samples and repeated at least three times. Briefly, cells were harvested by trypsinization, resuspended in DMEM medium, and plated in a 96-well plate at 3,000 cells per well. At 72 h after treatment with different doses of 17-DMAG (ranging from 0.1 nM to 0.5 μM) in 0.1% DMSO (Sigma, St. Louis,

MO, USA), the culture medium was replaced and 50 μl of 1.0 mg/ml sterile filtered 3-(4, 5-dimethylthiazol-2-yl)-2, 5-diphenyl tetrazolium bromide (MTT, Sigma, St. Louis, MO, USA) was added to each well. The unreacted dye was removed after 4 h and the insoluble formazan crystals were dissolved in 150 μl of DMSO. The absorbance at 570 nm (reference wavelength: 630 nm) was measured with a Tecan microplate reader (Tecan, San Jose, CA, USA).

Flow cytometry

Twenty-four hours after 17-DMAG treatment, SKOV-3 cells were harvested and washed with phosphate-buffered saline (PBS) containing 0.5% bovine serum albumin (BSA). Upon blockade by 2% BSA in PBS, the cells were incubated with trastuzumab (10 μg/ml in PBS containing 2% BSA). Fluorescein isothiocyanate (FITC)-conjugated donkey anti-human IgG was then added and allowed to incubate for 1 h at room temperature. After washing, the cells were analyzed using an LSR flow cytometer (Beckman Coulter, Fullerton, CA, USA). The FITC signal intensity was analyzed using the Cell-Quest software (version 3.3, Becton Dickinson, Franklin Lakes, NJ, USA).

Western blot

At 8 and 24 h after treatment with 200 nM 17-DMAG, SKOV-3 cells were collected. Total protein was extracted using radioimmunoprecipitation assay (RIPA) buffer (Pierce Biotechnology, Rockford, IL, USA) plus 1 mM ethylenediaminetetraacetate (EDTA), 1% Triton 100, 10% glycerol, and protease inhibitors. The concentration of total protein was determined using a microBCA protein assay kit (Pierce Biotechnology, Rockford, IL, USA). After sodium dodecyl sulfate polyacrylamide gel electrophoresis (SDS-PAGE) separation of 40 μg of total protein, it was transferred to a polyvinylidene fluoride membrane (Invitrogen, Carlsbad, CA, USA) and incubated at room temperature with 5% nonfat milk blocking buffer. The blots were then incubated overnight at 4°C with trastuzumab followed by incubation at room temperature for 1 h with horseradish peroxidase (HRP)-conjugated antihuman antibody and anti-rabbit antibody (GE Healthcare, Piscataway, NJ, USA). The bands were detected using an ECL Western blotting detection system (GE Healthcare, Piscataway, NJ, USA) with α-tubulin as loading control.

Tumor model and treatment protocol

All animal experiments were performed under a protocol approved by the Stanford University Administrative Panel on Laboratory Animal Care (A-PLAC).

Subcutaneous SKOV-3 tumor models were established in 4- to 6-week-old female athymic nude mice. Typically, 5×10^6 cells suspended in 100 μl of serum-free DMEM medium were injected into the right front flank of the mice. The mice were subjected to microPET imaging studies when the tumor volume reached 200–400 mm^3 (3–4 weeks after inoculation). Animals in one group each received a total of 150 mg/kg of 17-DMAG dissolved in 10% DMSO and 10% ethanol over 24 h in three doses of 50 mg/kg each. The control animals were each injected with equal amounts of DMSO/ethanol without 17-DMAG. For therapy study, a dose of 50 mg/kg of 17-DMAG was given by tail vein injection for 3 consecutive days. Tumor growth was monitored by caliper measurement and tumor

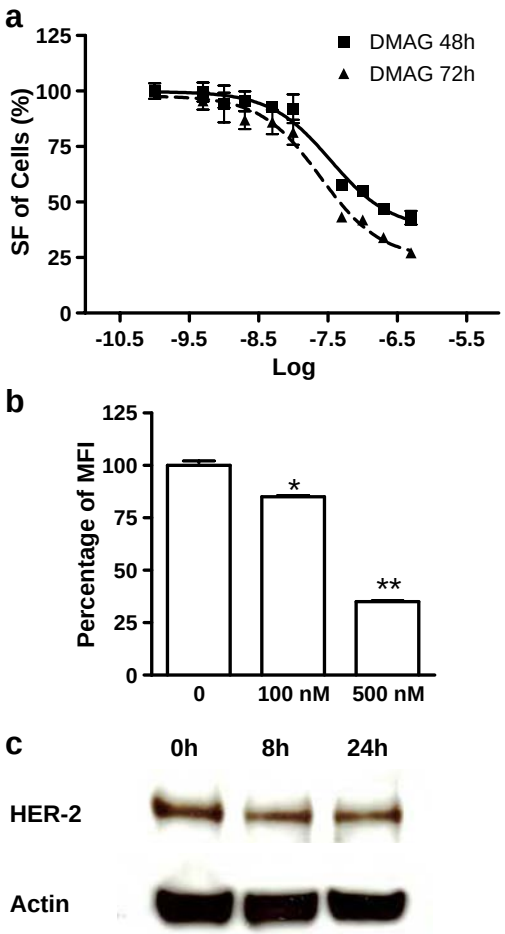

Fig. 1 **a** The cytotoxic effect of 17-DMAG on SKOV-3 human ovarian cancer cells. SKOV-3 cells were treated with serial concentrations of 17-DMAG. At 48 and 72 h after treatment, the cell proliferation was determined by MTT assay. **b** Flow cytometric analysis of HER-2 expression on SKOV-3 cells after being treated with different concentrations of 17-DMAG. Trastuzumab was used as the primary antibody and FITC-conjugated donkey antihuman IgG as the secondary antibody. The mean value of FITC signal intensity (*MFI*) of the three measurements are also shown (mean±SD). **c** Western blot of HER-2 in SKOV-3 cells treated or untreated with 200 nM of 17-DMAG. Trastuzumab was used as the primary mAb. *$p<0.05$; **$p<0.01$

volume was calculated by the equation: tumor volume (mm^3)=long diameter×(short diameter) ^{2}/2.

MicroPET and image analysis

Detailed procedures for DOTA conjugation were performed as previously described [34]. ^{64}Cu-DOTA-trastuzumab was purified by PD-10 column using PBS as the mobile phase. PET of tumor-bearing mice was performed on a microPET R4 rodent model scanner (Siemens Medical Solutions USA, Inc., Malvern, PA, USA). Twenty-four hours after 17-DMAG treatment, the mice were intravenously injected with ^{64}Cu-DOTA-trastuzumab (7-8 MBq/mouse) and static scans were acquired at 4 and 24 h post-injection (p.i.). For each microPET scan, three-dimensional regions of interest (ROIs) were drawn over the tumor, liver, heart, and muscle on decay-corrected whole-body coronal images. The average radioactivity concentration within a tumor or an organ was obtained from the mean pixel values within the ROI volume, which were converted to counts/ml per min by using a conversion factor. Assuming a tissue density of 1 g/ml, the counts/ml per min were converted to counts/g per min and then divided by the injected dose (ID) to obtain an imaging ROI-derived %ID/g.

For FDG imaging, after fasting for 6 h, 3.7 MBq of ^{18}F-FDG in 150 μl of PBS was injected via tail vein. A 7-min prone acquisition scan was performed approximately 60 min after injection. Mice were maintained under isoflurane anesthesia during the injection, accumulation, and scanning periods and the body temperature was maintained by a heating lamp. PET images were analyzed and quantified as described above.

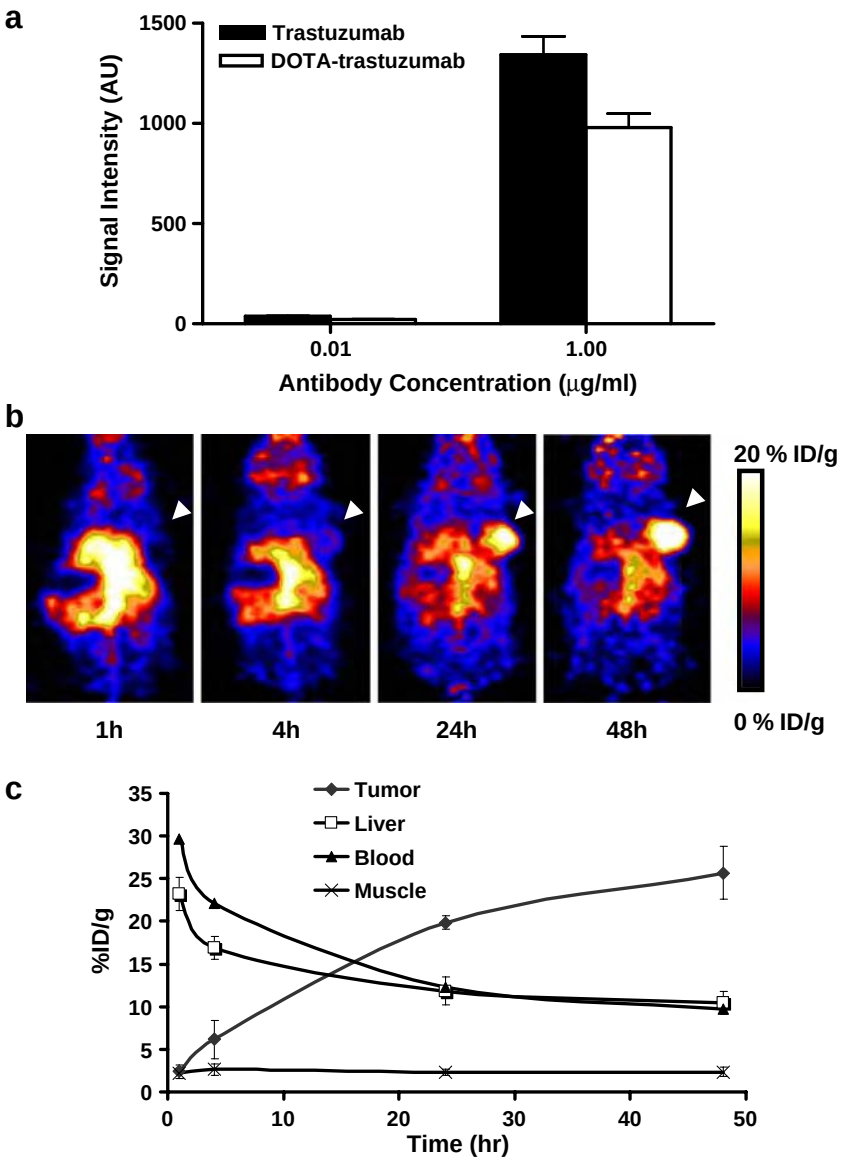

Fig. 2 **a** Flow cytometric analysis of HER-2 expression on SKOV-3 cells with DOTA-conjugated trastuzumab as the primary antibody. The mean value of FITC signal intensity (MFI) of the three measurements are also shown (mean± SD). **b** MicroPET images of SKOV-3 tumor-bearing nude mice at different time points after intravenous injection of ^{64}Cu-DOTA-trastuzumab (n=4/group). Decay-corrected whole-body coronal images are shown and the tumors are indicated by *white arrowheads*. **c** SKOV-3 tumor and major organ uptake of ^{64}Cu-DOTA-trastuzumab as quantified from microPET scans (n=4/group)

Biodistribution studies

After microPET imaging, mice bearing SKOV-3 tumor xenografts were sacrificed and dissected. Blood, tumor, and major organs and tissues were collected and wet weighed. The radioactivity in each tissue was measured using a gamma counter (Packard Instrument) and the results were presented as %ID/g. For each mouse, the radioactivity of the tissue samples was calibrated against a known aliquot of the injectate and normalized to a body mass of 25 g. Values were expressed as mean±SD for a group of four animals.

Immunofluorescence staining

Frozen SKOV-3 tumor sections (5 μm thick) were warmed to room temperature, fixed with ice-cold acetone for 10 min, and dried in the air for 30 min. The sections were rinsed in PBS for 2 min and blocked in 10% donkey serum for 1 h at room temperature. The sections were incubated with trastuzumab (10 μg/ml) for 1 h at room temperature and visualized with FITC-conjugated donkey antihuman secondary antibody (1:200, Jackson ImmunoResearch Laboratories, West Grove, PA, USA) under a microscope (Carl Zeiss Axiovert 200 M, Carl Zeiss USA, Thornwood, NY, USA). Images were acquired under the same conditions and displayed at the same scale.

Statistical analysis

Quantitative data were expressed as mean±SD. Means were compared using one-way analysis of variance (ANOVA) and Student's *t* test; p values<0.05 were considered statistically significant.

Results

17-DMAG inhibits SKOV-3 cell proliferation and induces HER-2 degradation

The effect of 17-DMAG on the proliferation of SKOV-3 cells was assessed by MTT colorimetric assay. We found that 17-DMAG inhibited cell proliferation in a dose-dependent manner (Fig. 1a). The IC_{50} value was about 34.58 nM at the 48-h time point and 24.72 nM at the 72-h time point.

17-DMAG has been reported to downregulate HER-2 expression through the inhibition of Hsp90 function [35, 36]. Next we performed flow cytometry analysis using trastuzumab as the primary antibody to assess the effect of 17-DMAG on HER-2 expression level in SKOV-3 cells. As shown in Fig. 1b, 17-DMAG significantly decreased HER-2 expression in a dose-dependent manner. The HER-2 level dropped by 15% after incubation with 100 nM of 17-DMAG for 24 h and by 65% with 500 nM of 17-DMAG. Western results (Fig. 1c) showed that as early as 8 h after treated with 17-DMAG HER-2 protein level began to decrease, indicating that it is possible to detect the early response of SKOV-3 cells to 17-DMAG treatment by monitoring HER-2 degradation.

Imaging HER-2 expression with microPET

^{64}Cu-DOTA-trastuzumab was determined to have around 20 DOTA residues per trastuzumab [37]. Flow cytometry analysis with DOTA-trastuzumab showed that after DOTA conjugation, the antibody still keeps relatively high binding affinity with HER-2 (Fig. 2a). The specific activity of

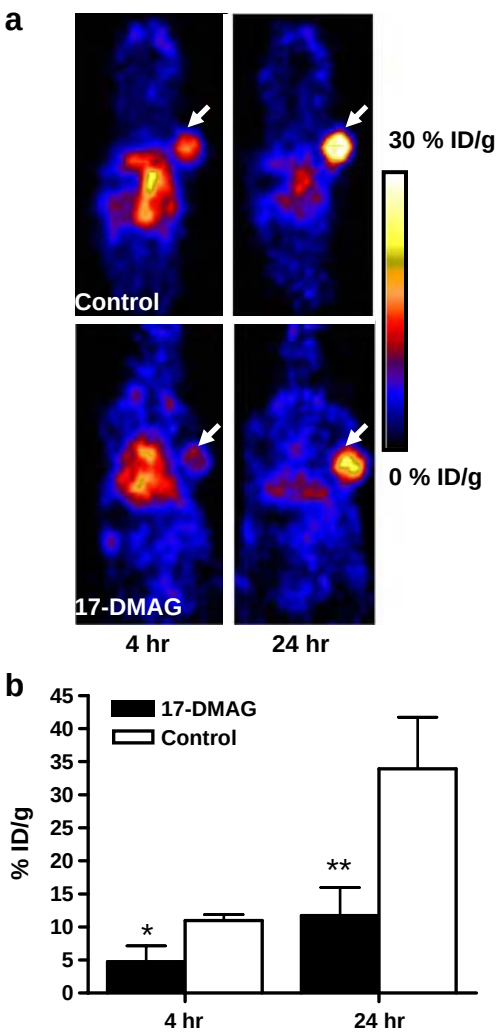

Fig. 3 **a** MicroPET images of SKOV-3 tumor-bearing nude mice treated with or without 17-DMAG at 4 and 24 h after intravenous injection of ^{64}Cu-DOTA-trastuzumab (n=4/group). Decay-corrected whole-body coronal images are shown and the tumors are indicated by *white arrows*. **b** SKOV-3 tumor uptake of ^{64}Cu-DOTA-trastuzumab as quantified from microPET scans (n=4/group)

^{64}Cu-DOTA-trastuzumab was 1.36±0.15 GBq/mg mAb and the radiolabeling yield was around 85%. PET scans were performed at different time points after i.v. injection of 3.7 MBq of ^{64}Cu-DOTA-trastuzumab to SKOV-3 tumor-bearing nude mice. As seen in Fig. 2b, the SKOV-3 tumor uptake of ^{64}Cu-DOTA-trastuzumab was increased with time and almost reached a plateau at about 24 h p.i. The tumor uptake was 2.39±0.76, 6.13±2.30, 19.85±0.83, and 25.69±3.10 %ID/g at 1, 4, 24, and 48 h p.i., respectively. ^{64}Cu-DOTA-trastuzumab exhibited high uptake in the heart (due to the blood pool activity) and liver at early time points, whereas the tracer uptake in all the other organs was at the background level (Fig. 2b). As shown in Fig. 2c, the tracer uptake in both the heart and the liver dropped steadily over time. For the heart, the uptake was 29.68±4.05, 22.15±6.11, 12.34±5.54, and 9.72±6.58 %ID/g at 1, 4, 24, and 48 h p.i., respectively. For the liver, the uptake was 23.25±1.92, 16.91±1.33, 11.81±1.64, and 10.45±1.38 %ID/g at 1, 4, 24, and 48 h p.i., respectively.

MicroPET imaging of HER-2 degradation

In order to image the HER-2 changes after 17-DMAG treatment, PET scans were performed in SKOV-3 tumor-bearing animals 24 h after a single dose of 17-DMAG treatment. The decay-corrected whole-body coronal images containing the tumors are shown in Fig. 3a. After being treated with 150 mg/kg of 17-DMAG for 24 h, the SKOV-3 tumor uptake of ^{64}Cu-DOTA-trastuzumab was much lower at both early and late time points as compared with the untreated group. Quantitative data based on ROI analysis are shown in Fig. 3b. In untreated mice, the SKOV-3 tumor uptake of ^{64}Cu-DOTA-trastuzumab was 10.96±0.93 %ID/g and 33.90±7.82 %ID/g at 4 and 24 h p.i., respectively. The uptake in 17-DMAG-treated tumors was significantly lower, with 4.75±2.41 %ID/g and 11.74±4.23 %ID/g at 4 and 24 h p.i., respectively ($p<0.05$ at both time points). There were no significant differences in ^{64}Cu-DOTA-trastuzumab uptake in other major organs between the 17-DMAG-treated and untreated animals.

Biodistribution studies

After microPET imaging at 24 h p.i., the animals were sacrificed for biodistribution studies and the results are shown in Fig. 4a. The untreated SKOV-3 tumors had a high tracer uptake of 33.43±8.93 %ID/g, consistent with the noninvasive microPET imaging results. After 17-DMAG

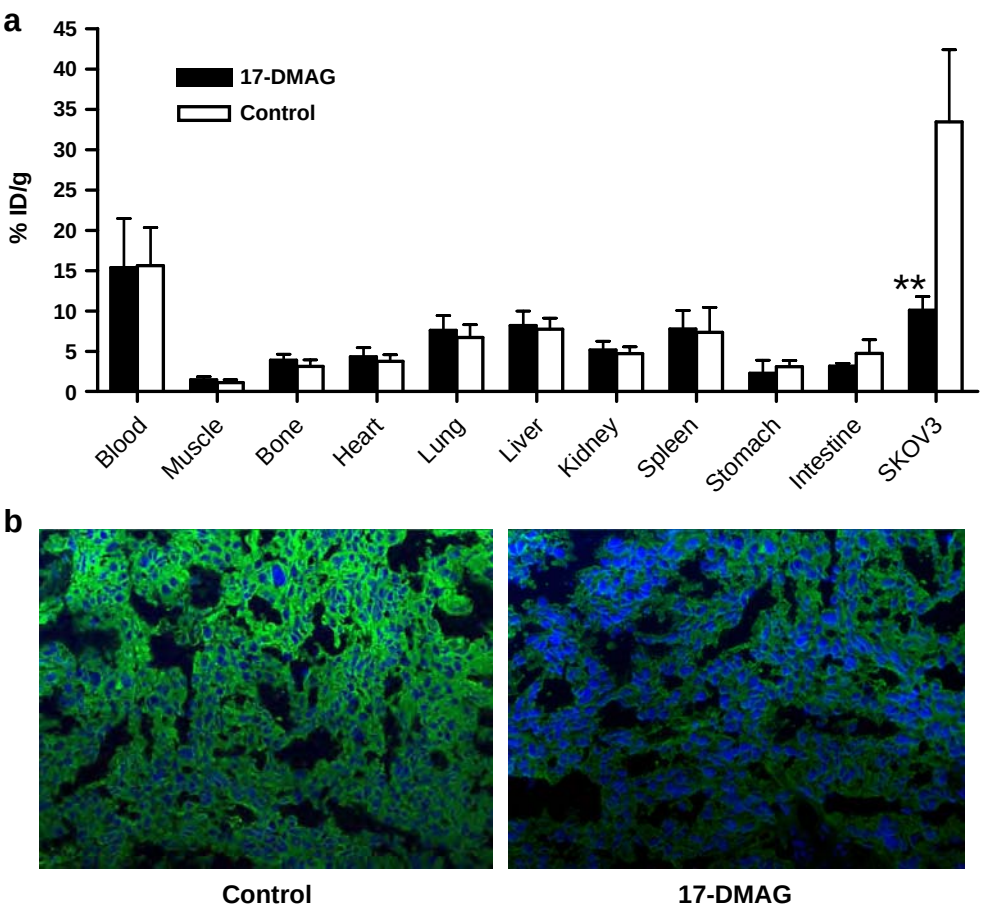

Fig. 4 **a** Biodistribution of ^{64}Cu-DOTA-trastuzumab (with or without 17-DMAG treatment) in SKOV-3 tumor-bearing mice at 24 h post-injection (n=4/group). **b** Immunofluorescence staining of HER-2 in 17-DMAG-treated and untreated SKOV-3 tumor tissues. Images were obtained under the same conditions and displayed at the same magnification and scale (200×). *$p<0.05$; **$p<0.01$

treatment, the uptake decreased significantly to 10.08±0.71 %ID/g ($p<0.01$). Blood activity concentration was 15.38±6.09 and 15.61±4.71 %ID/g in 17-DMAG-treated and control group, indicating the relatively long circulation half-life of the antibody. The liver also had prominent radioactivity accumulation, with an uptake of 8.17±1.79 and 7.71±1.40 %ID/g at 24 h p.i., due to both the hepatic clearance of antibody-based tracer and possible transchelation. The spleen also had uptake similar to the liver.

Immunofluorescence staining

To further confirm that 17-DMAG induces HER-2 degradation in vivo, we performed immunofluorescence staining using trastuzumab as the primary antibody and FITC-conjugated donkey antihuman IgG as the secondary antibody. Images were taken under the same conditions and displayed at the same scale to make sure that the relative brightness observed in the images reflected the difference in HER-2 expression level. In the untreated SKOV-3 tumor, HER-2 expression was very high as indicated by the strong pseudo-colored green signal in the tissue. After being treated with 17-DMAG, HER-2 expression was apparently lower with a much weaker fluorescence signal (Fig. 4b). Both the biodistribution and immunofluorescence staining studies confirmed that the decrease in tumor HER-2 expression level upon 17-DMAG treatment can be noninvasively monitored by ^{64}Cu-DOTA-trastuzumab PET.

17-DMAG inhibits SKOV-3 tumor growth

The effects of 17-DMAG on both the tumor volume and body weight are shown in Fig. 5a and Fig. 5b, respectively. 17-DMAG is relatively nontoxic as there was no significant difference in mouse body weight between the control and treated animals. After treatment with 17-DMAG, the tumor growth was delayed and the tumor size was significantly smaller than the control group by day 12 ($p<0.01$). The tumors in the control animals continued to grow exponentially with an apparent doubling time of 5.1 days and increased in size by a factor of 6.1 by day 16. In comparison, the 17-DMAG-treated animals were only increased in size by a factor of 3.3 by day 16 (Fig. 5a).

Imaging of HER-2 changes during the therapeutic process

At day 7 after the first dose of 17-DMAG, i.e., day 3 after the last dose, the animals were scanned with ^{18}F-FDG and ^{64}Cu-DOTA-trastuzumab in tandem (Fig. 6). All tumors showed relatively high uptake of FDG. However, there was no significant difference between the therapeutic group (4.85±0.73 %ID/g) and the control group (4.95±0.82 %ID/g). In contrast, control tumors showed much higher accumulation

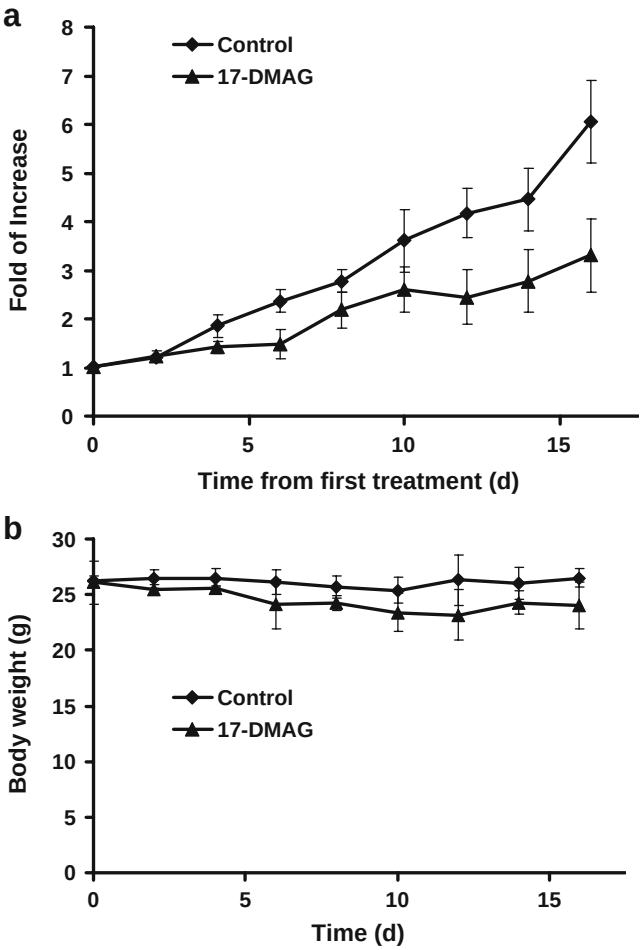

Fig. 5 **a** Comparison of SKOV-3 tumor growth in nude mice treated with 17-DMAG vs control animals. **b** Comparison of body mass of nude mice treated with 17-DMAG vs control animals. Animals were treated with 17-DMAG (50 mg/kg per day) for 3 consecutive days

of ^{64}Cu-DOTA-trastuzumab (25.68±5.33 %ID/g) at 24 h p.i. than that of the 17-DMAG-treated group (12.86±2.41 %ID/g). The tumors showed low ^{64}Cu-DOTA-IgG uptake (5.34±1.24 %ID/g), further confirming the specificity of ^{64}Cu-DOTA-trastuzumab and low nonspecific targeting of antibodies in SKOV-3 tumor models.

Discussion

It has been reported that the Hsp90 inhibitor 17-DMAG is a more effective cytotoxic agent than 17-AAG in gynecologic cancer cells by affecting multiple downstream pathways including EGFR/HER-2 and Akt/PTEN [38]. The antitumor efficacy of 17-DMAG has also been confirmed in human breast and melanoma tumor models [39]. In this study, we treated SKOV-3 human ovarian cancer model with 17-DMAG and both in vitro and in vivo data supported that 17-DMAG is a potent anticancer agent. During the therapeutic

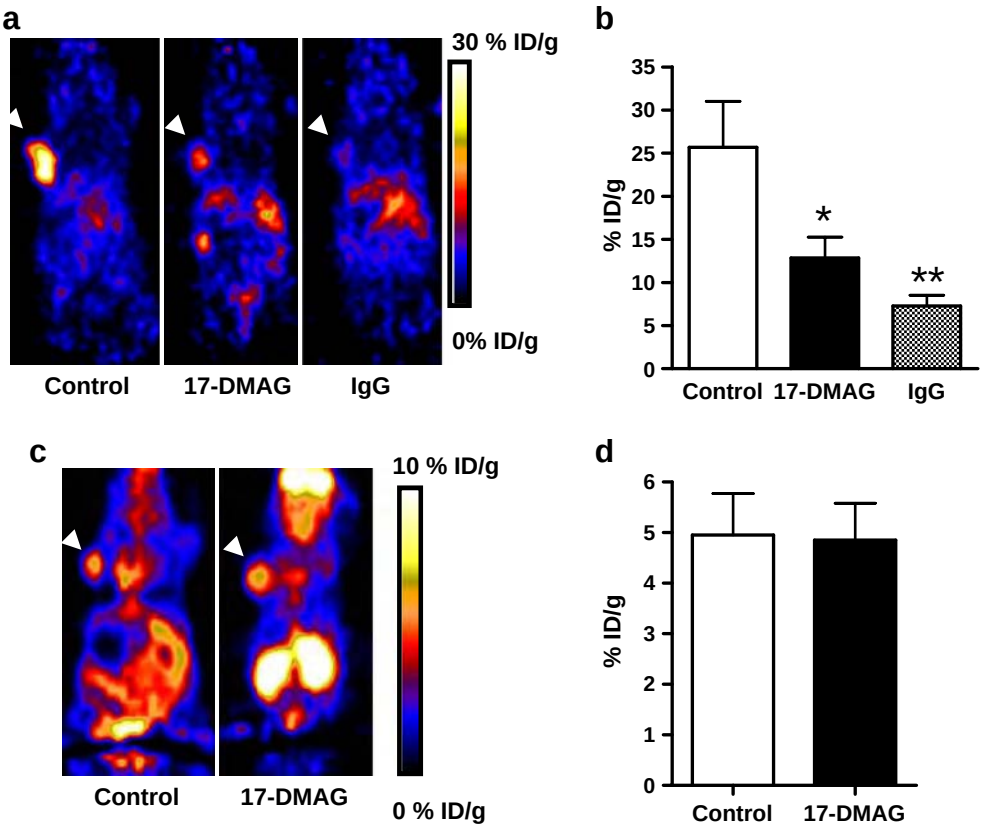

Fig. 6 **a** MicroPET images of SKOV-3 tumor-bearing nude mice with ^{64}Cu-DOTA-trastuzumab at day 5 after being treated with 17-DMAG (n=4–7/group). Decay-corrected whole-body coronal images are shown and the tumors are indicated by *white arrowheads*. **b** SKOV-3 tumor uptake of ^{64}Cu-DOTA-trastuzumab as quantified from microPET scans (n=4–7/group). **c** MicroPET images of SKOV-3 tumor-bearing nude mice with ^{18}F-FDG at day 5 after treatment with 17-DMAG (n=4–7/group). Decay-corrected whole-body coronal images are shown and the tumors are indicated by *white arrowheads*. **d** SKOV-3 tumor uptake of ^{18}F-FDG as quantified from microPET scans (n=4–7/group). *p<0.05; **p<0.01

process, we performed microPET imaging with ^{64}Cu-labeled anti-HER-2 mAb trastuzumab for the noninvasive monitoring of HER-2 expression and degradation.

Accurate evaluation of the HER-2 status in tumors by noninvasive molecular imaging will be critical for HER-2-related therapies. HER-2 itself is an intensively investigated therapeutic target and trastuzumab is the first monoclonal antibody approved by the Food and Drug Administration (FDA). Guidelines of the American Society of Clinical Oncology (ASCO) recommend evaluation of HER-2 expression on every primary breast cancer either at the time of diagnosis or at the time of recurrence [40]. Moreover, as a key component in promoting cell proliferation, HER-2 is closely related to other therapeutics such as Hsp90 inhibitors as performed in this study or histone deacetylase (HDAC) inhibitors [41, 42]. Through monitoring the status of HER-2, the early response to certain drugs or potential drug candidates can be assessed. In this study, a series of imaging studies were carried out to evaluate HER-2 expression level. First, ^{64}Cu-DOTA-trastuzumab accumulation was clearly visualized on untreated SKOV-3 tumors, reaching a plateau from 24 to 48 h p.i. Second, the tumor accumulation of ^{64}Cu-DOTA-trastuzumab quantified from PET ROI analysis was significantly lower in 17-DMAG-treated animals (3 × 50 mg/kg 17-DMAg administered within 24 h) than in untreated animals (11.74±4.23 %ID/g vs 33.90±7.82 %ID/g 24 h p.i.), which corroborates the direct tissue sampling biodistribution studies of the same animals after the microPET scans. The HER-2 degradation was further confirmed by ex vivo immunofluorescent staining. Finally, we treated the animals with 3×50 mg/kg 17-DMAG for 3 consecutive days and measured the tumor size to observe the therapeutic efficacy of 17-DMAG. ^{18}F-FDG PET was performed at day 4 since the start of the treatment and ^{64}Cu-DOTA-trastuzumab PET at day 5. Again, tumor accumulation of ^{64}Cu-DOTA-trastuzumab was significantly lower in the 17-DMAG-treated group than that in the control group as reflected on the quantitative microPET images. In contrast, FDG PET was unable to differentiate the treated from untreated. Smith-Jones et al. previously imaged HER-2 level in a 17-AAG-treated BT-474 human breast cancer model and found that the decrease of HER-2 level lasted for at least 7 days [43]. The results from our experiment are consistent with their findings.

Despite the high affinity for HER-2 antigen and high accumulation in HER-2-positive tumors, ^{64}Cu-DOTA-trastuzumab has relatively slow clearance that makes it unsuitable for multiple scans within short time intervals. The imaging studies were done in a subcutaneous ovarian cancer model. It is not clear whether ^{64}Cu-DOTA-trastuzumab will be as useful in orthotopic ovarian cancer models since this antibody probe has relatively high uptake in the liver and lower abdomen. For such purposes, suitably labeled small molecules, peptides, antibody fragments, or affibodies

might have an advantage over intact monoclonal antibodies [44, 45]. Overall, antibodies are still the best established class of binding molecules for tumor diagnosis and therapy [23, 46]. Compared with antibody fragments and affibodies, whole antibodies are superior in both affinity and specificity to the targets. In addition, much lower kidney accumulation may be an add-on for ovarian cancer localization and evaluation. Finally, ^{64}Cu-DOTA-trastuzumab PET imaging will be more appropriate to the situation in which Hsp90 inhibitors were combined with trastuzumab for synergistic tumor control. Since HER-2 is one of the most sensitive client proteins of Hsp90 [6], it is not surprising to see synergistic effect when combining Hsp90 inhibition and anti-HER-2 therapy. Indeed, it has been reported that the combination of trastuzumab and 17-AAG induced enhanced HER-2 degradation and cytotoxicity in HER-2 overexpressing breast cancer cells [47]. More importantly, the synergistic growth arrest and cell death was not observed in cancer cells with low HER-2 expression. This synergistic effect was further substantiated by a phase I/II trial which showed multiple partial responses in HER-2-positive metastatic breast cancer patients using 17-AAG plus trastuzumab [48]. It is worth mentioning that the same dose and schedule of 17-AAG was used in this trial as the other failed clinical trials described earlier [19]. With ^{64}Cu-DOTA-trastuzumab PET imaging, more comprehensive information can be retrieved noninvasively including HER-2 expression status, antibody delivery and distribution, and early response to the combined treatment.

Conclusion

We describe here the use of quantitative HER-2 PET imaging with ^{64}Cu-DOTA-trastuzumab for monitoring the early therapeutic response upon 17-DMAG treatment in a SKOV-3 human ovarian cancer model. The quantification of HER-2 degradation during 17-DMAG treatment using PET imaging is consistent with the in vitro and ex vivo measurements. This approach may be clinically translated to monitor the therapeutic response in HER-2-positive cancer patients under 17-DMAG treatment and to select patients for 17-DMAG and trastuzumab combination therapy.

Acknowledgement This work was supported by the National Cancer Institute (NCI) P50 CA114747 and a DOD Prostate Postdoctoral Fellowship from Department of Defense (to G. Niu).

References

1. Jakob U, Lilie H, Meyer I, Buchner J. Transient interaction of Hsp90 with early unfolding intermediates of citrate synthase. Implications for heat shock in vivo. J Biol Chem. 1995;270:7288–94. doi:10.1074/jbc.270.13.7288.
2. Blagosklonny MV, Toretsky J, Bohen S, Neckers L. Mutant conformation of p53 translated in vitro or in vivo requires functional HSP90. Proc Natl Acad Sci U S A. 1996;93:8379–83. doi:10.1073/pnas.93.16.8379.
3. Clarke PA, Hostein I, Banerji U, Stefano FD, Maloney A, Walton M, et al. Gene expression profiling of human colon cancer cells following inhibition of signal transduction by 17-allylamino-17-demethoxygeldanamycin, an inhibitor of the hsp90 molecular chaperone. Oncogene 2000;19:4125–33. doi:10.1038/sj.onc.1203753.
4. Burrows F, Zhang H, Kamal A. Hsp90 activation and cell cycle regulation. Cell Cycle 2004;3:1530–6.
5. Solit DB, Zheng FF, Drobnjak M, Münster PN, Higgins B, Verbel D, et al. 17-Allylamino-17-demethoxygeldanamycin induces the degradation of androgen receptor and HER-2/neu and inhibits the growth of prostate cancer xenografts. Clin Cancer Res. 2002;8:986–93.
6. Basso AD, Solit DB, Munster PN, Rosen N. Ansamycin antibiotics inhibit Akt activation and cyclin D expression in breast cancer cells that overexpress HER2. Oncogene 2002;21:1159–66. doi:10.1038/sj.onc.1205184.
7. Pratt WB, Toft DO. Regulation of signaling protein function and trafficking by the hsp90/hsp70-based chaperone machinery. Exp Biol Med (Maywood) 2003;228:111–33.
8. Schechter AL, Hung MC, Vaidyanathan L, Weinberg RA, Yang-Feng TL, Francke U, et al. The neu gene: an erbB-homologous gene distinct from and unlinked to the gene encoding the EGF receptor. Science 1985;229:976–8. doi:10.1126/science.2992090.
9. Tan M, Yao J, Yu D. Overexpression of the c-erbB-2 gene enhanced intrinsic metastasis potential in human breast cancer cells without increasing their transformation abilities. Cancer Res. 1997;57:1199–205.
10. Bacus SS, Ruby SG, Weinberg DS, Chin D, Ortiz R, Bacus JW. HER-2/neu oncogene expression and proliferation in breast cancers. Am J Pathol. 1990;137:103–11.
11. Wiercioch R, Balcerczak E, Byszewska E, Mirowski M. Uptake of radiolabelled herceptin by experimental mammary adenocarcinoma. Nucl Med Rev Cent East Eur. 2003;6:99–103.
12. Traish AM, Wotiz HH. Prostatic epidermal growth factor receptors and their regulation by androgens. Endocrinology 1987;121:1461–7.
13. Fischer U, Kopka L, Brinck U, Korabiowska M, Schauer A, Grabbe E. Prognostic value of contrast-enhanced MR mammography in patients with breast cancer. Eur Radiol. 1997;7:1002–5. doi:10.1007/s003300050240.
14. Citri A, Alroy I, Lavi S, Rubin C, Xu W, Grammatikakis N, et al. Drug-induced ubiquitylation and degradation of ErbB receptor tyrosine kinases: implications for cancer therapy. EMBO J. 2002;21:2407–17. doi:10.1093/emboj/21.10.2407.
15. Murakami Y, Mizuno S, Uehara Y. Accelerated degradation of 160 kDa epidermal growth factor (EGF) receptor precursor by the tyrosine kinase inhibitor herbimycin A in the endoplasmic reticulum of A431 human epidermoid carcinoma cells. Biochem J. 1994;301(Pt 1):63–8.
16. Kelland LR, Sharp SY, Rogers PM, Myers TG, Workman P. DT-Diaphorase expression and tumor cell sensitivity to 17-allylamino, 17-demethoxygeldanamycin, an inhibitor of heat shock protein 90. J Natl Cancer Inst. 1999;91:1940–9. doi:10.1093/jnci/91.22.1940.
17. Silcox CE, Smith RC, King R, McDannold N, Bromley P, Walsh K, et al. MRI-guided ultrasonic heating allows spatial control of exogenous luciferase in canine prostate. Ultrasound Med Biol. 2005;31:965–70. doi:10.1016/j.ultrasmedbio.2005.03.009.
18. Sausville EA, Tomaszewski JE, Ivy P. Clinical development of 17-allylamino, 17-demethoxygeldanamycin. Curr Cancer Drug Targets 2003;3:377–83. doi:10.2174/1568009033481831.

19. Solit DB, Osman I, Polsky D, Panageas KS, Daud A, Goydos JS, et al. Phase II trial of 17-allylamino-17-demethoxygeldanamycin in patients with metastatic melanoma. Clin Cancer Res. 2008; 14:8302–7. doi:10.1158/1078-0432.CCR-08-1002.
20. Ronnen EA, Kondagunta GV, Ishill N, Sweeney SM, Deluca JK, Schwartz L, et al. A phase II trial of 17-(allylamino)-17-demethoxygeldanamycin in patients with papillary and clear cell renal cell carcinoma. Invest New Drugs 2006;24:543–6. doi:10.1007/s10637-006-9208-z.
21. Barzilay E, Ben-Califa N, Supino-Rosin L, Kashman Y, Hirschberg K, Elazar Z, et al. Geldanamycin-associated inhibition of intracellular trafficking is attributed to a co-purified activity. J Biol Chem. 2004;279:6847–52. doi:10.1074/jbc.M312799200.
22. Lang SA, Klein D, Moser C, Gaumann A, Glockzin G, Dahlke MH, et al. Inhibition of heat shock protein 90 impairs epidermal growth factor-mediated signaling in gastric cancer cells and reduces tumor growth and vascularization in vivo. Mol Cancer Ther. 2007;6:1123–32. doi:10.1158/1535-7163.MCT-06-0628.
23. Smith MA, Morton CL, Phelps DA, Kolb EA, Lock R, Carol H, et al. Stage 1 testing and pharmacodynamic evaluation of the HSP90 inhibitor alvespimycin (17-DMAG, KOS-1022) by the pediatric preclinical testing program. Pediatr Blood Cancer 2008;51:34–41. doi:10.1002/pbc.21508.
24. Niu G, Chen X. Has molecular and cellular imaging enhanced drug discovery and drug development? Drugs R D 2008;9:351–68. doi:10.2165/0126839-200809060-00002.
25. McManus DT, Patterson AH, Maxwell P, Humphreys MW, Anderson NH. Fluorescence in situ hybridisation detection of erbB2 amplification in breast cancer fine needle aspirates. Mol Pathol. 1999;52:75–7. doi:10.1136/mp. 52.2.75.
26. Stomper PC, Budnick RM, Stewart CC. Use of specimen mammography-guided FNA (fine-needle aspirates) for flow cytometric multiple marker analysis and immunophenotyping in breast cancer. Cytometry 2000;42:165–73. doi:10.1002/1097-0320(20000615) 42:3<165::AID-CYTO2>3.0.CO;2-7.
27. Tokunaga E, Oki E, Nishida K, Koga T, Egashira A, Morita M, et al. Trastuzumab and breast cancer: developments and current status. Int J Clin Oncol. 2006;11:199–208. doi:10.1007/s10147-006-0575-4.
28. Thrall JH. Personalized medicine. Radiology 2004;231:613–16. 10.1148/radiol.2313040323.
29. Shepard HM, Lewis GD, Sarup JC, Fendly BM, Maneval D, Mordenti J, et al. Monoclonal antibody therapy of human cancer: taking the HER2 protooncogene to the clinic. J Clin Immunol. 1991;11:117–27. doi:10.1007/BF00918679.
30. Carter P, Presta L, Gorman CM, Ridgway JB, Henner D, Wong WL, et al. Humanization of an anti-p185HER2 antibody for human cancer therapy. Proc Natl Acad Sci U S A. 1992;89:4285–9. doi:10.1073/pnas.89.10.4285.
31. Bulte JWM, Kraitchman DL. Iron oxide MR contrast agents for molecular and cellular imaging. NMR Biomed. 2004;17:484–99. doi:10.1002/nbm.924.
32. Lee JH, Huh YM, Jun YW, Seo JW, Jang JT, Song HT, et al. Artificially engineered magnetic nanoparticles for ultra-sensitive molecular imaging. Nat Med. 2007;13:95–9. doi:10.1038/nm1467.
33. Lub-de Hooge MN, Kosterink JG, Perik PJ, Nijnuis H, Tran L, Bart J, et al. Preclinical characterisation of 111In-DTPA-trastuzumab. Br J Pharmacol. 2004;143:99–106. doi:10.1038/sj.bjp.0705915.
34. Niu G, Cai W, Chen K, Chen X. Non-invasive PET imaging of EGFR degradation induced by a heat shock protein 90 inhibitor. Mol Imaging Biol. 2008;10:99–106. doi:10.1007/s11307-007-0123-2.
35. Konecny GE, Pegram MD, Venkatesan N, Finn R, Yang G, Rahmeh M, et al. Activity of the dual kinase inhibitor lapatinib (GW572016) against HER-2-overexpressing and trastuzumab-treated breast cancer cells. Cancer Res. 2006;66:1630–9. doi:10.1158/0008-5472.CAN-05-1182.
36. Lang W, Caldwell GW, Li J, Leo GC, Jones WJ, Masucci JA. Biotransformation of geldanamycin and 17-allylamino-17-demethoxygeldanamycin by human liver microsomes: reductive versus oxidative metabolism and implications. Drug Metab Dispos. 2007;35:21–9. doi:10.1124/dmd.106.009639.
37. Cai W, Wu Y, Chen K, Cao Q, Tice DA, Chen X. In vitro and in vivo characterization of 64Cu-labeled Abegrin, a humanized monoclonal antibody against integrin alpha v beta 3. Cancer Res. 2006;66:9673–81. doi:10.1158/0008-5472.CAN-06-1480.
38. Gossett DR, Bradley MS, Jin X, Lin J. 17-Allyamino-17-demethoxygeldanamycin and 17-NN-dimethyl ethylene diamine-geldanamycin have cytotoxic activity against multiple gynecologic cancer cell types. Gynecol Oncol. 2005;96:381–8. doi:10.1016/j.ygyno.2004.10.009.
39. Hollingshead M, Alley M, Burger AM, Borgel S, Pacula-Cox C, Fiebig HH, et al. In vivo antitumor efficacy of 17-DMAG (17-dimethylaminoethylamino-17-demethoxygeldanamycin hydrochloride), a water-soluble geldanamycin derivative. Cancer Chemother Pharmacol. 2005;56:115–25. doi:10.1007/s00280-004-0939-2.
40. Bast RC Jr, Ravdin P, Hayes DF, Bates S, Fritsche H Jr, Jessup JM, et al. 2000 update of recommendations for the use of tumor markers in breast and colorectal cancer: clinical practice guidelines of the American Society of Clinical Oncology. J Clin Oncol. 2001;19:1865–78.
41. Strahl BD, Allis CD. The language of covalent histone modifications. Nature 2000;403:41–5. doi:10.1038/47412.
42. Turner BM. Cellular memory and the histone code. Cell 2002;111:285–91. doi:10.1016/S0092-8674(02) 01080-2.
43. Smith-Jones PM, Solit DB, Akhurst T, Afroze F, Rosen N, Larson SM. Imaging the pharmacodynamics of HER2 degradation in response to Hsp90 inhibitors. Nat Biotechnol 2004;22:701–6. doi:10.1038/nbt968.
44. Smith-Jones PM, Solit D, Afroze F, Rosen N, Larson SM. Early tumor response to Hsp90 therapy using HER2 PET: comparison with 18F-FDG PET. J Nucl Med. 2006;47:793–6.
45. Orlova A, Tolmachev V, Pehrson R, Lindborg M, Tran T, Sandström M, et al. Synthetic affibody molecules: a novel class of affinity ligands for molecular imaging of HER2-expressing malignant tumors. Cancer Res. 2007;67:2178–86. doi:10.1158/0008-5472.CAN-06-2887.
46. Bernier J. Drug insight: cetuximab in the treatment of recurrent and metastatic squamous cell carcinoma of the head and neck. Nat Clin Pract Oncol. 2008;5:705–13.
47. Raja SM, Clubb RJ, Bhattacharyya M, Dimri M, Cheng H, Pan W, et al. A combination of trastuzumab and 17-AAG induces enhanced ubiquitinylation and lysosomal pathway-dependent ErbB2 degradation and cytotoxicity in ErbB2-overexpressing breast cancer cells. Cancer Biol Ther. 2008;7:1630–40. doi:10.1158/1535-7163.MCT-07-2409.
48. Modi S, Stopeck AT, Gordon MS, Mendelson D, Solit DB, Bagatell R, et al. Combination of trastuzumab and tanespimycin (17-AAG, KOS-953) is safe and active in trastuzumab-refractory HER-2 overexpressing breast cancer: a phase I dose-escalation study. J Clin Oncol. 2007;25:5410–7. doi:10.1200/JCO.2007.11.7960.

Provided for non-commercial research and education use.
Not for reproduction, distribution or commercial use.

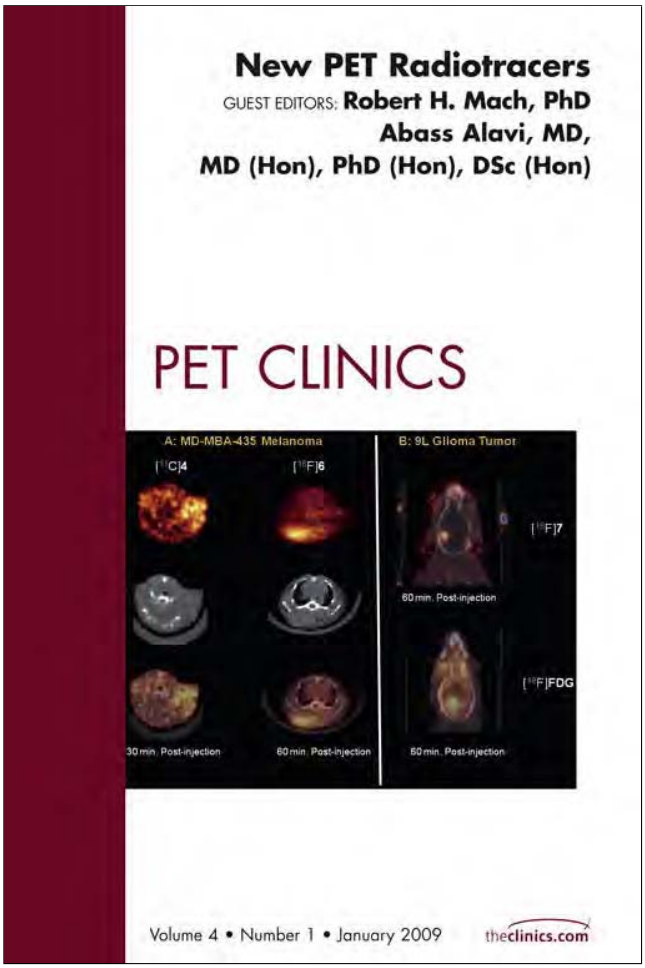

This article appeared in a journal published by Elsevier. The attached copy is furnished to the author for internal non-commercial research and education use, including for instruction at the authors institution and sharing with colleagues.

Other uses, including reproduction and distribution, or selling or licensing copies, or posting to personal, institutional or third party websites are prohibited.

In most cases authors are permitted to post their version of the article (e.g. in Word or Tex form) to their personal website or institutional repository. Authors requiring further information regarding Elsevier's archiving and manuscript policies are encouraged to visit:

http://www.elsevier.com/copyright

Author's personal copy

PET Imaging of Angiogenesis

Gang Niu, PhD, Xiaoyuan Chen, PhD*

KEYWORDS

• Angiogenesis • Molecular imaging
• Integrin • VEGFR • MMP

Angiogenesis refers to the process by which new blood vessels are formed and is involved in various physiologic as well as pathologic processes, including physical development, wound repair, reproduction, response to ischemia, arthritis, psoriasis, retinopathies, solid tumor growth, and metastatic tumor spread.[1] Angiogenesis is a highly controlled process that is dependent on the intricate balance of both promoting and inhibiting factors.

Antiangiogenic and antivascular agents are intensively investigated for tumor therapy and can be potentially used to control eye diseases and arthritis. Proangiogenic therapy are also undergoing clinical trials in human patients suffering from ischemic heart disease, peripheral vascular disease, chronic wounds, or stroke.[2] A comprehensive understanding of the molecular mechanisms that regulate angiogenesis has resulted in the design of new and more effective therapeutic strategies.[3] Although preclinical animal studies have demonstrated the benefit of proangiogenic therapy, recent clinical trials focused on the stimulation of myocardial or peripheral angiogenesis by the local delivery of growth factors were somewhat disappointing, showing no clear benefit over placebo in subjects with severe ischemia.[4] Most of these studies evaluated angiogenesis by using standard clinical endpoints or by looking for a physiologic improvement (ie, improvement in perfusion). These approaches may have insufficient sensitivity to detect a therapeutic benefit.

For tumor therapy, bevacizumab, a humanized monoclonal antibody directed against vascular endothelial growth factor (VEGF), is the first drug developed as an inhibitor of angiogenesis approved by the Food and Drug Administration (FDA).[5–7] Sorafenib and sunitinib that target multiple receptor tyrosine kinases (VEGF receptors and platelet-derived growth factor—PDGF—receptors), have also been approved by the FDA as antiangiogenic drugs.[8] Traditionally, the gold standard to evaluate therapeutic response is tumor volume change. Clinical trials with conventional cytotoxic chemotherapeutic agents have mainly used morphologic imaging to provide indices of therapeutic response, mostly CT or MR imaging according to the Response Evaluation Criteria in Solid Tumors introduced in 2000.[9] However, antiangiogenic agents are typically cytostatic rather than cytotoxic and lead to a stop or delay of tumor progression rather than tumor shrinkage. Thus, it is not sensitive to use tumor volume as an indicator for therapeutic efficacy evaluation and it might take months or years to assess.

Both the success and setback in angiogenesis-related therapies spur the need for the development of noninvasive imaging strategies for the direct noninvasive evaluation of molecular events associated with angiogenesis. Imaging is

Some of the research presented in this article was supported in part by the National Institute of Biomedical Imaging and Bioengineering (R21 EB001785), National Cancer Institute (R21 CA102123, P50 CA114747, U54 CA119367, and R24 CA93862), Department of Defense (W81XWH-04-1-0697, W81XWH-06-1-0665, W81XWH-06-1-0042, and DAMD17-03-1-0143), and a Department of Defense Prostate Postdoctoral Fellowship from Department of Defense (to G.N.)

The Molecular Imaging Program at Stanford, Department of Radiology and Bio-X Program, Stanford University School of Medicine, 1201 Welch Road, P095, Stanford, CA 94305-5484, USA
* Corresponding author.
E-mail address: shawchen@stanford.edu (X. Chen).

PET Clin 4 (2009) 17–38
doi:10.1016/j.cpet.2009.04.011
1556-8598/09/$ – see front matter © 2009 Elsevier Inc. All rights reserved.

Author's personal copy

expected to provide a novel approach to noninvasively monitor angiogenesis, to optimize the dose of new antiangiogenic agents, and to assess the efficacy of therapies directed at modulation of the angiogenic process.[10–13] This article, after brief introduction of angiogenesis biology and structure and functional imaging of angiogenesis with various imaging modalities, focuses on the application of PET in angiogenesis imaging at both the functional and molecular level.

BIOLOGY OF ANGIOGENESIS

The whole angiogenesis process involves several steps, including the growth of endothelial sprouts from pre-existing postcapillary venules and following the growth and remodeling process of the primitive network into a complex network.[14] The cellular and molecular mechanisms of angiogenesis differ in various tissues and physiologic or pathologic angiogenesis.[15] This section gives a brief introduction of tumor angiogenesis.

Each solid malignancy starts as a small population of transformed cells that do not initially have a blood supply of their own. Tumor cells are initially supplied by diffusion and tumor growth is limited by the lack of access to growth factors, circulating oxygen, and nutrients.[16] Without angiogenesis, the growth of solid tumors remains restricted to 2 mm to 3 mm in diameter.[17] Tumor angiogenesis occurs as a series of events.[18,19] First, diseased tissues produce and release angiogenic growth factors that diffuse into the nearby tissues in response to tumor hypoxia, such as the VEGF, the acidic and basic fibroblast growth factors (aFGF, bFGF), and the platelet-derived endothelial cell growth factor.[20] When the angiogenic growth factors bind to their corresponding specific receptors located on the endothelial cells of pre-existing blood vessels, various signal transduction pathways are activated, for example phosphorylation of tyrosine kinases, protein kinases, and MAP kinases, and consequently to the activation of endothelial cells.[21,22] Consequently, the original vessels undergo characteristic morphologic changes, including enlargement of the diameter, basement membrane degradation, a thinned endothelial cell lining, increased endothelial number, decreased pericyte number, and pericyte detachment.[23] In the next step, several different mechanisms may lead to the formation of new tumor blood vessels.[24,25] The original vessels may retain their large diameter and evolve into medium-sized arteries and veins by acquiring a smooth muscle and internal elastica. Alternatively, the endothelium of a mother vessel may form smaller, separate, well-differentiated vessel channels by projecting cytoplasmic structures into the lumen, which form translumenal bridges. A third process is called "intussusception" and involves focal invagination of connective tissue pillars from within the mother vessel. Finally, endothelial cell-sprouting may occur, which requires the focal dissolution of the basement membrane surrounding mother vessels.[26] This is achieved by a number of proteolytic enzymes, including matrix metalloproteinases (MMPs) and plasminogen activator, which enable endothelial cells to exit the vessel. Activated angiogenic endothelial cells proliferate rapidly and migrate into the extracellular matrix toward the angiogenic stimulus.[27] Cell surface-adhesion molecules, such as integrins, play an important role in endothelial cell migration and in contact with the extracellular tumor matrix, facilitate cell survival.[28,29] At the sprouting tips of growing vessels, endothelial cells secrete MMPs that facilitate degradation of the extracellular matrix and cell invasion.[30] Next, a lumen within an endothelial cell tubule has to be formed, which requires interactions between the extracellular matrix and cell-associated surface proteins, among them are galectin-2, PECAM-1, and VE-cadherin.[31] Finally, newly formed vessels are stabilized through the recruitment of smooth muscle cells and pericytes.

STRUCTURAL IMAGING OF VASCULATURE/ ANGIOGENESIS

All imaging modalities can provide structural information, although they have different spatial resolution. The old-fashioned way for vascular structure imaging is X-ray angiography. However, it is difficult to provide microvasculature information. Following the steps of improvement of imaging equipments, contrast agents, and data acquisition and analysis techniques, more detailed vascular structure was deciphered. Several modalities are available for tumor microvascular imaging, including intravital microscope, CT angiography, contrast-enhanced ultrasound (US), and high-resolution MR angiography.[32] Ex vivo structural imaging of tumor vasculature can be achieved by various techniques, such as vascular casts,[33,34] immunohistochemic staining of endothelial cell markers such as CD31 and von Willebrand factor,[35,36] labeling the endothelial cells by fluorescent reporters expressed in transgenic mice,[37,38] and intravital labeling.[39,40] Tumor macrovasculature imaging can be performed clinically by various imaging modalities, such as CT,[41,42] MR imaging,[43,44] and US.[45] However, visualization of the microvasculature is very challenging even after administration of intravascular contrast agents.

Author's personal copy

Scanners dedicated to small-animal imaging studies, such as microCT, have better spatial resolution in preclinical models but with poor temporal resolution and large radiation exposure.[46]

Intravital microscopy of tumors growing in window chambers in animal models can directly investigate tumor angiogenesis and vascular response to treatment, in terms of both the morphology of the vascular networks and the function of individual vessels.[47] This technique allows for repeated measurements of the same tumor with very high resolution (down to submicrometer level). Multiphoton fluorescence microscopy techniques have also been applied to these model systems to obtain three-dimensional images of the tumor vasculature.[47]

FUNCTIONAL IMAGING OF VASCULATURE

The major consequence of angiogenesis is to perfuse and oxygenate surrounding tissue; therefore, the angiogenic process can be assessed by the evaluation of standard physiologic parameters, such as regional perfusion, function, and metabolism. During antiangiogenic or proangiogenic therapies, the changes in hemodynamic parameters can also be promising biomarkers for evaluating the therapeutic effect along with morphologic changes. Traditionally, tumor angiogenesis and antiangiogenic therapy have been evaluated by methods such as measurement of circulating angiogenic markers and histologic estimate of microvascular density. Various imaging modalities, including dynamic contrast-enhanced (DCE) MR imaging, US, PET (especially with [^{15}O]water), and DCE-CT are currently employed to provide functional information of the vasculature.[48]

DCE-MR imaging has been well established to investigate angiogenesis within tumors, and in particular the response to antiangiogenic therapy. DCE-MR imaging works by tracking the pharmacokinetics of injected contrast agents as they pass through the tumor vasculature, which represents a complex summation of vascular permeability, blood flow, vascular surface area, and interstitial pressure.[49,50]

DCE-MR imaging can be performed with low-molecular-weight contrast media (LMCM) such as Gd-diethylenetriamine pentaacetic acid (Gd-DTPA) or macromolecular contrast media (MMCM), such as Gd conjugated human serum albumin.[51] It has been shown that DCE-MR imaging can detect responses to PTK/ZK (a VEGF receptor-tyrosine kinase inhibitor) therapy as early as 2 days after therapy with significant reductions in area under gadolinium-contrast-medium curve[52] or permeability parameters,[53] which also predict subsequent response. LMCM DCE-MR imaging has also shown significant reductions in permeability values in patients treated with the antivascular agents AG-013,736 (an inhibitor of the VEGF, PDGF, and c-Kit receptor tyrosine kinases) and SU5416 (a selective inhibitor of VEGFR-2 tyrosine kinase) activity.[54] Although consensus is still lacking on the exact kinetic model to be used in analyzing DCE-MR imaging data, the differences among the various methods are often marginal. Therefore, DCE-MR imaging is rapidly emerging as the imaging technique of choice for monitoring clinical response in trials of new antiangiogenic and antivascular therapies. Unlike LMCM, the increased size of MMCMs makes them less diffusible, and K^{trans} values may reflect permeability within tumors more accurately.[55] MMCMs can also give more accurate estimates of tumor blood volume because they are excellent blood-pool agents. For example, SU6668 is an oral, small-molecule inhibitor of angiogenic receptor tyrosine kinases, such as VEGFR-2 (Flk-1/KDR), PDGFR, and FGF receptor. DCE-MR imaging clearly detected the early effect (after 24 hours of treatment) of SU6668 on tumor vasculature as a 51% and 26% decrease in the average vessel permeability measured in the tumor rim and core, respectively. A substantial decrease was also observed in average fractional plasma volume in the rim (59%) and core (35%) of the tumor.[56,57] In addition to DCE-MR imaging, other MR imaging techniques have also been developed to retrieve functional information of the vasculature. In arterial spin labeling, water molecules can be labeled for MR imgaging by inverting the nuclear spin of their hydrogen atoms with a radiofrequency pulse directed at the arterial blood before it enters the regions of interest (ROIs).[58,59] An absolute value of blood flow is determined by the change in the MR signal as the labeled water in the arterial bloodstream arrives in the ROI.[60] Blood-oxygen-level dependent MR imaging can detect the changes in oxygen saturation of the blood and this effect can be enhanced by increasing the amount of oxygen in the breathed air.[61,62]

US is also well established as a means of measuring blood flow or, more precisely, blood velocity using the Doppler principle or microbubbles as contrast agent.[63–66] Power Doppler can be quantified to give an estimate of the relative fractional vascular volume, while microbubbles can show blood flow down to the microcirculation level by raising the signal from smaller vessels.[67,68] Specialized contrast-specific US techniques have been developed for improving image qualities, such as pulse inversion[69,70] and power

Author's personal copy

modulation.[71] Given the fundamental assumption that the relation between microbubble-concentration video intensity is linear up to the achievement of a plateau phase,[72] in animal models contrast-enhanced US can quantify tumor vascularity determined by neoangiogenesis.[73,74] The use of US contrast agents and nonlinear processing provide access to the bulk properties of the microvascular compartment but they do not offer sufficient resolution to observe the morphology and detailed flow characteristics of the microvasculature. With high-frequency US, it is possible to achieve resolution ranging from 15 μm to 100 μm in the 20-MHz to 100-MHz range.[45] However, it is subject to an inherent trade-off between image resolution and imaging depth.[75] US (particularly microbubble contrast-enhanced US) is a valuable imaging modality to determine the tumor microvascular-blood volume and blood velocity.[76] DCE-US allows repeated examinations and provides both morphologic and functional analyses. US modes, based on the second harmonic signal generated by the nonlinear properties of contrast agents, have provided access to tumor blood flow with the quantification of the contrast-uptake kinetics within tumors after a bolus injection of contrast agent.[77] Several quantitative parameters considered as indicators of tumor flow, such as the peak intensity or time-to-peak intensity, can be extracted from the time-intensity curves of contrast uptake.[78] Using DCE-US, the antitumor efficacy of AVE8062, a tumor vasculature-disruptive agent, has been assessed in melanoma-bearing nude mice.[79]

Many other imaging modalities can also reveal the functional properties of the vasculature. DCE-CT is analogous to DCE-MR imaging.[80,81] To minimize the exposure to ionizing radiation and the nephrotoxicity of CT contrast agents, DCE-CT studies are typically quite brief, using only a low dose of contrast agent. Optical imaging can also be applied to evaluate important functional indexes of blood vessels, such as vascular permeability, vessel size, and blood flow.[82] Multiphoton microscopy in combination with fluorescently labeled molecules can be used to quantify the permeability of individual tumor blood vessels noninvasively deep inside living animals.[83] Fluorescence-mediated tomography has been applied to measure angiogenesis in superficial tissue by using fluorescent nanoparticles.[84] However, optical imaging is still limited to tissue and animal models.

PET IMAGING

So far, PET is the most sensitive and specific technique for imaging molecular pathways in vivo in humans.[85] PET radiotracers are physiologically and pharmacologically relevant compounds labeled with positron-emitting radioisotopes (such as fluoride-18 or carbon-11). After internalization by injection or inhalation, the tracer reaches the target and the location and the quantity is then detected with a PET scanner. With a ring-shaped array of photoelectric crystals, PET detectors capture "coincidentally" a pair of 511 keV photons at almost 180° separation emitted by interaction of a positron with negatively charged electrons. The raw PET-scan data are the set of coincidental photoelectric events, logged for time and location, which indicate the position of the molecule spatiotemporally. Using reconstruction algorithms, images can then be constructed tomographically and regional time activities can be derived.[86]

The inherent sensitivity and specificity of PET is the major strength of this technique. Isotopes can be detected down to the 100-picomolar level in the target tissues. At this low level, the compounds often have little or no physiologic effect on the patient or the test animal, which permits studying the mechanism of action or biodistribution independent of any physiologic consequences.[87,88] The spatial resolution of PET down to the millimeter level permits applications not only to human beings for diagnosis and drug development but also to animals for preclinical studies. The ability of PET to translate studies from animals to human beings adds to its appeal.

Compared with single-photon emission computed tomography (SPECT), PET offers increased spatial information and permits more accurate attenuation correction. Many PET radiotracers have a short half-life, which allows for repetitive imaging over time. However, the anatomic resolution of PET (approximately 4 mm^3–8 mm^3 in clinical and 1 mm^3–2 mm^3 in small-animal imaging systems) is noticeably poorer than that achieved by CT or MR imaging.[89] The variable movement of positrons before annihilation, and the deviation of the generated 511 keV photons from the exact 180° angular separation, can limit the resolution. To overcome this limitation, hybrid systems such as PET-CT have been introduced.[90] The CT component of the hybrid system is used to improve anatomic definition of the ROIs for analysis and to create radiation-attenuation maps to correct for nonuniform attenuation.[91] With the development of microPET or microPET/CT scanners dedicated to small-animal imaging studies, PET can provide a similar in vivo imaging capability in mice, rats, monkeys, and human beings, so one can readily transfer knowledge and molecular measurements between species.[92,93] Initial experiments with PET/MR imaging prototypes also showed very promising

Author's personal copy

results, indicating its great potential for clinical and preclinical imaging.[94]

Functional Imaging of Angiogenesis with PET

A major advantage of the nuclear medicine techniques especially using PET tracers is that they are truly quantitative and that the tissue concentration C_t can be measured noninvasively.[95] ^{133}Xe has been used to measure regional cerebral blood flow[96] and ^{11}C-microspheres of approximately 10-μm diameter have been used as the gold standard for perfusion measurements or for validation of new imaging methods for perfusion measurement.[97]

Today, most PET-perfusion measurements are performed using ^{15}O-H_2O, using either static or dynamic PET imaging.[98] ^{15}O-H_2O satisfies all the requirements for a perfusion tracer in Fick's model[99] (1) because it is biologically and metabolically inert, and freely diffusible into and out of tissue water.

$$C_t = P^* \int (C_i - C_e) d_t \quad \textbf{(1)}$$

C_t = tissue concentration, mol*ml_{tissue}^{-1}; C_i = Influx concentration, mol*$ml_{carrier}^{-1}$

C_e = eflux concentration, mol*$ml_{carrier}^{-1}$; P = Perfusion, $ml_{carrier}$ * min^{-1}* ml_{tissue}^{-1}

Thus, "tissue water" can be modeled as a single compartment including both tissue and its draining fluids (lymphatics and veins). Two methods can be used for measuring perfusion with [^{15}O]H_2O, the steady-state method, and the ^{15}O-dynamic water method.[100,101] The latter is currently used most often for perfusion studies because of improved PET scanner technology. The tracer is administered by inhalation or by peripheral venous bolus injection. Continuous arterial data are obtained either by image-based arterial input functions (a large vessel like the aorta or the left ventricle) or by peripheral sampling to a well-counter device. The data are compatible with those from diseases investigated with other methods, and the values reported by PET for tumors are within the reported range for PET in other tissues.[102,103] In locally advanced breast cancer, first results with dynamic ^{15}O-H_2O PET are promising, as tumor blood flow decreased in the responder group after chemotherapy, whereas it increased in the nonresponder group.[104]

PET imaging can also be used to derive data on blood volume and vascular permeability. Blood volume imaging with PET uses ^{15}O-CO or ^{11}C-CO carbon monoxide. ^{15}O-CO binds irreversibly with hemoglobin to form ^{15}O-CO-Hb carboxyhemoglobin.[86] Because ^{15}O-CO-Hb remains exclusively within the vasculature, it can be used as a tracer of vascular volume. A tissue concentration dataset is obtained over a further 5 to 6 minutes and an arterial ^{15}O-CO-Hb concentration curve is derived from a series of arterial blood samples over the same interval. Another method for blood volume imaging is labeling red blood cells or albumin with radionuclides, because both are too large to leave normal blood vessels and are retained in the blood pool. In tumor vessels, leakage of these contrast agents into the tumor will occur, but this effect can be used to calculate the tumor vessel permeability when dynamic imaging is performed. For PET, the tracer ^{68}Ga-DOTA-albumin has been developed and showed favorable results in first animal studies.[105]

Imaging of Molecular Markers of Vasculature

Even though structural and functional imaging of the vasculature can reveal potentially useful information before, during, and after therapeutic intervention, they do not convey enough knowledge about the biologic changes upon therapy at the molecular level, which may occur long before any structural or functional changes can be detected. While techniques such as DCE-MR imaging and ^{15}O-H_2O PET for the assessment of hemodynamic parameters are widely used, the interpretation of the results with regard to their physiologic meaning often remains difficult. Therefore, more specific markers of angiogenic activity are necessary for pretherapeutic assessment of angiogenesis and response evaluation during therapy. One approach is to identify molecular markers of angiogenesis—such as receptors, enzymes, or extracellular matrix proteins—and to use specific ligands to these targets conjugated with imaging probes for PET, SPECT, MR imaging, optical imaging, or US.[106–108] Several molecular imaging makers including integrins, VEGF/VEGFR, MMPs, and Hypoxia/HIF1 are angiogenesis-related and PET imaging targeting to these markers is discussed in the following sections.

PET imaging of integrins

Integrins, a family of cell-adhesion molecules, are involved in a wide range of cell-extracellular matrix and cell-cell interactions.[28,109] Integrins are heterodimeric transmembrane glycoproteins consisting of different α- and β-subunits, which play an important role in cell-cell- and cell-matrix-interactions.[110] In mammals, 18-α and 8-β subunits assemble into at least 24 different receptors.[111] Integrins expressed on endothelial cells modulate cell migration and survival during angiogenesis, while

Author's personal copy

integrins expressed on carcinoma cells potentiate metastasis by facilitating invasion and movement across the blood vessels. The $\alpha_v\beta_3$ integrin, which binds to Arginine-Glycine-Aspartic acid (RGD)-containing components of the interstitial matrix, such as vitronectin, fibronectin, and thrombospondin,[112,113] is expressed in a number of tumor types, such as melanoma, late-stage glioblastoma, ovarian, breast, and prostate cancer.[114–116] The critical role of integrin $\alpha_v\beta_3$ in tumor invasion and metastasis arises from its ability to recruit and activate MMP-2 and plasmin, which can degrade components of the basement membrane and interstitial matrix.[117] Among all 24 integrins discovered to date, integrin $\alpha_v\beta_3$ is the most intensively studied, though many other integrins, such as $\alpha_v\beta_1$, $\alpha_v\beta_5$, $\alpha_5\beta_1$, and $\alpha_4\beta_1$ also play important roles in regulating angiogenesis.[29,118–121]

Several extracellular matrix proteins like vitronectin, fibrinogen, and fibronectin interact via the RGD tripeptide sequence with the integrins.[113] Based on these findings, linear as well as cyclic RGD peptides have been introduced and showed high affinity and selectivity for $\alpha_v\beta_3$.[122,123] The first in vivo application of radioiodinated RGD peptides revealed the receptor-specific tumor uptake but also predominantly hepatobiliary elimination, resulting in high activity concentration in the liver and small intestine.[124] Consequently, several strategies to improve the pharmacokinetics of radiohalogenated peptides have been studied, including conjugation with sugar moieties, hydrophilic amino acids and polyethylene glycol (PEG).[125–128] Besides radiohalogenated RGD peptides, a variety of radiometalated tracers have been developed as well, including peptides labeled with ^{111}In, ^{99m}Tc, ^{64}Cu, ^{90}Y, ^{188}Re, and ^{68}Ga.[129–132] Most of them are based on the cyclic pentapeptide and are conjugated via the γ-amino function of a lysine with different chelator systems, like DTPA, the tetrapeptide sequence H-Asp-Lys-Cys-Lys-OH, 1, 4, 7, 10-tetraazacyclododecane-N-N″-N″-N‴-tetraacetic acid (DOTA), and 1,4,7-triazacyclononane-1,4,7-triacetic acid. While all these compounds have shown high receptor affinity and selectivity and specific tumor accumulation, the pharmacokinetics of most of them still have to be improved.[133] Among them, the compound ^{99m}Tc-NC100692 by GE Healthcare has been used for SPECT imaging in preclinical and clinical studies.[134]

In a human melanoma M21 model, ^{18}F-Galacto-RGD showed a tumor uptake of 1.5%ID/g at 120 minutes after injection.[135,136] Integrin receptor-specific accumulation was demonstrated by blocking experiments injecting c(RGDfV) 10 minutes before tracer injection, which reduced tumor accumulation to approximately 35% of control. A correlation between integrin expression and tracer accumulation was observed in imaging studies with mice bearing melanoma tumors with increasing amounts of $\alpha_v\beta_3$-positive cells.[137] These data demonstrate that noninvasive determination of $\alpha_v\beta_3$ expression and quantification with radiolabeled RGD peptides is feasible with PET scans. ^{18}F-Galacto-RGD has also been applied to patients and successfully imaged $\alpha_v\beta_3$ expression in human tumors with good tumor-background ratios.[138] Rapid clearance of ^{18}F-Galacto-RGD from the blood pool and primarily renal excretion was confirmed by following biodistribution and dosimetry studies. Background activity in lung and muscle tissue was low and the calculated effective dose is very similar to an ^{18}F-FDG scan (**Fig. 1**).[138] Results from dynamic emission scans over 60 minutes and kinetic modeling studies suggested that standardized uptake values (SUVs) derived from static emission scans at approximately 60 minutes after injection can be used for the assessment of $\alpha_v\beta_3$ receptor density with reasonable accuracy.[139] SUVs and tumor-blood ratios based on PET imaging using ^{18}F-Galacto-RGD were also found to correlate with the intensity of immunohistochemical staining of $\alpha_v\beta_3$ expression, as well as with the microvessel density.[140] Good tumor-background ratios with ^{18}F-Galacto-RGD PET also have been demonstrated in squamous cell carcinoma of the head and neck with a widely varying intensity of tracer uptake. Immunohistochemistry demonstrated predominantly vascular $\alpha_v\beta_3$ expression, thus in squamous cell carcinoma of the head and neck, ^{18}F-Galacto-RGD PET might be used as a surrogate parameter of angiogenesis.[141] Moreover, there was no obvious correlation between the tracer uptake of ^{18}F-FDG and ^{18}F-Galacto-RGD in patients with various tumors, indicating that $\alpha_v\beta_3$ expression and glucose metabolism are not closely correlated in tumor lesions and that consequently ^{18}F-FDG cannot provide similar information as ^{18}F-Galacto-RGD.[142]

Within physiologic ^{18}F-Galacto-RGD uptake areas, such as liver, spleen, and intestine, lesion identification is still problematic. Therefore, multimeric RGD peptides have been developed to provide more effective antagonists with better targeting capability and higher cellular uptake through the integrin-dependent binding.[143] The underlying rationale is that the interaction between integrin $\alpha_v\beta_3$ and RGD-containing extracellular matrix-proteins involves multivalent binding sites with clustering of integrins. A series of multimeric RGD peptides labeled with ^{18}F or ^{64}Cu for PET imaging to improve the tumor-targeting

Author's personal copy

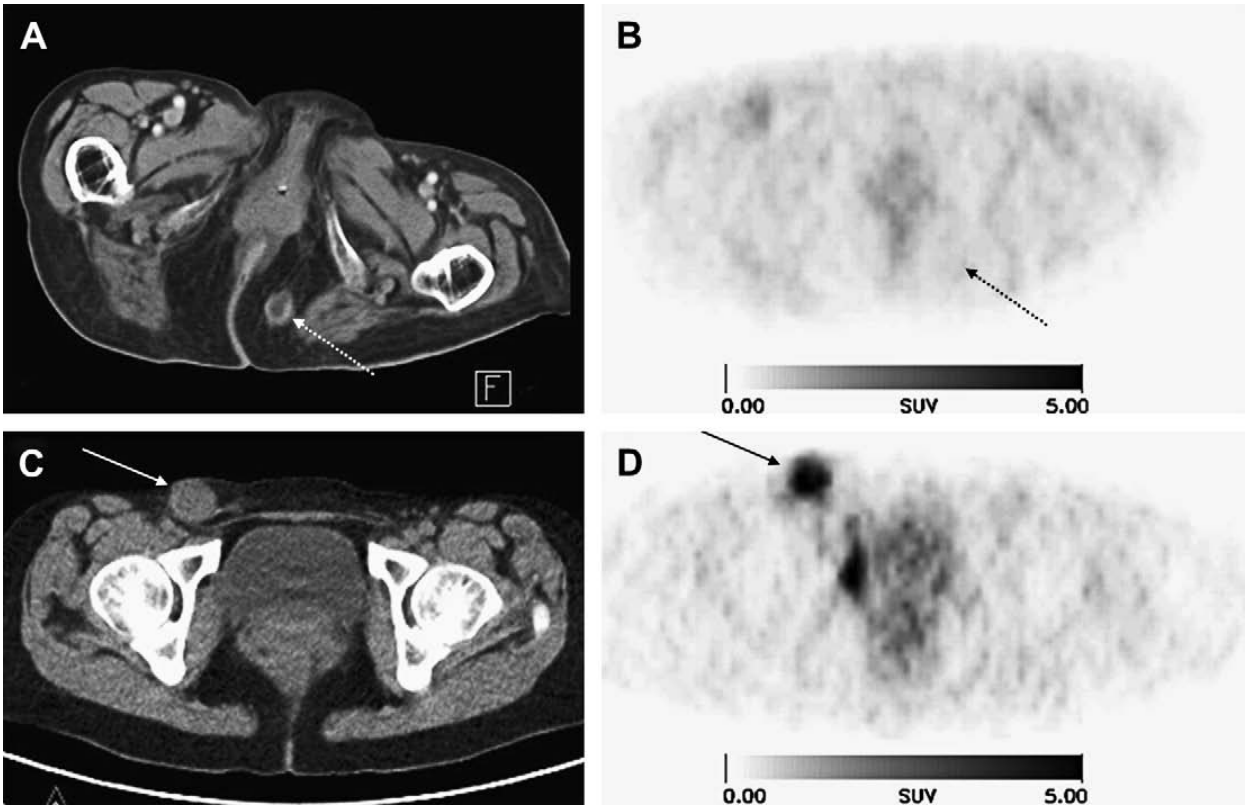

Fig. 1. ^{18}F-Galacto-RGD scans of two patients with metastases from malignant melanoma and different tracer uptake. (*Upper row*) An 89-year-old female patient with metastasis in subcutaneous fat in gluteal area on left side (*arrow with dotted line*). Tumor can be clearly delineated in CT scan (*A*), whereas it shows no significant uptake in ^{18}F-Galacto-RGD PET scan (*B*) (60 minutes after injection). (*Lower row*) A 36-year-old female patient with lymph node metastasis in right groin (*arrow*). Again, tumor is clearly visualized in CT scan (*C*) but also shows intense tracer uptake in ^{18}F-Galacto-RGD PET scan (*D*) (89 minutes after injection; SUV, 6.8). (*From* Beer AJ, Haubner R, Goebel M, et al. Biodistribution and pharmacokinetics of the $\alpha_v\beta_3$-selective tracer ^{18}F-galacto-RGD in cancer patients. J Nucl Med 2005;46(8):1340; with permission.)

efficacy and pharmacokinetics have been reported.[130,144–148] ^{18}F-FB-E[c(RGDyK)]$_2$ (abbreviated as ^{18}F-FRGD2) showed predominantly renal excretion and almost twice as much tumor uptake in the same animal model when compared with the monomeric tracer ^{18}F-FB-c(RGDyK).[144,145] Tumor uptakes quantified by microPET scans in six tumor xenograft models correlated well with integrin $\alpha_v\beta_3$ expression level measured by sodium dodecyl sulfate-polyacrylamide gel electrophoresis autoradiography. The tetrameric RGD peptide-based tracer, ^{18}F-E[E[c(RGDfK)]$_2$]$_2$, showed significantly higher receptor binding affinity than the corresponding monomeric and dimeric RGD analogs and demonstrated rapid blood clearance, high metabolic stability, predominant renal excretion, and significant receptor-mediated tumor uptake with good contrast in xenograft-bearing mice (**Fig. 2**).[148] Therefore, ^{18}F-E[E[c(RGDfK)]$_2$]$_2$ is a promising agent for peptide receptor radionuclide imaging as well as targeted internal radiotherapy of integrin $\alpha_v\beta_3$-positive tumors. Compared with tetramer, RGD octamer further increased the integrin avidity by another threefold. In vivo microPET imaging showed that ^{64}Cu-DOTA-RGD octamer had slightly higher initial tumor uptake and much longer tumor retention in U87MG tumor that express high levels of integrin.[149] However, compared with tetramers, higher renal uptake of the octamer was observed, which was attributed mainly to the integrin positivity of the kidneys. Wester and Kessler groups have also synthesized a series of monomeric, dimeric, tetrameric, and octameric RGD peptides. These compounds contain different numbers of c(RGDfE) peptides connected via PEG linker and lysine moieties, which are used as branching units.[150,151]

Besides RGD peptides, in vivo imaging using etaracizumab, a humanized monoclonal antibody against human integrin $\alpha_v\beta_3$, has been performed after DOTA conjugation and ^{64}Cu labeling. MicroPET studies revealed that ^{64}Cu-DOTA-etaracizumab had a high tumor-activity accumulation up to 49.41% plus or minus 4.54% injected dose per gram at 71 hours after injection for U87MG tumors.[152] Not only in malignant diseases: the integrin expression after myocardial infarction has also been monitored with ^{18}F-Galacto-RGD

Author's personal copy

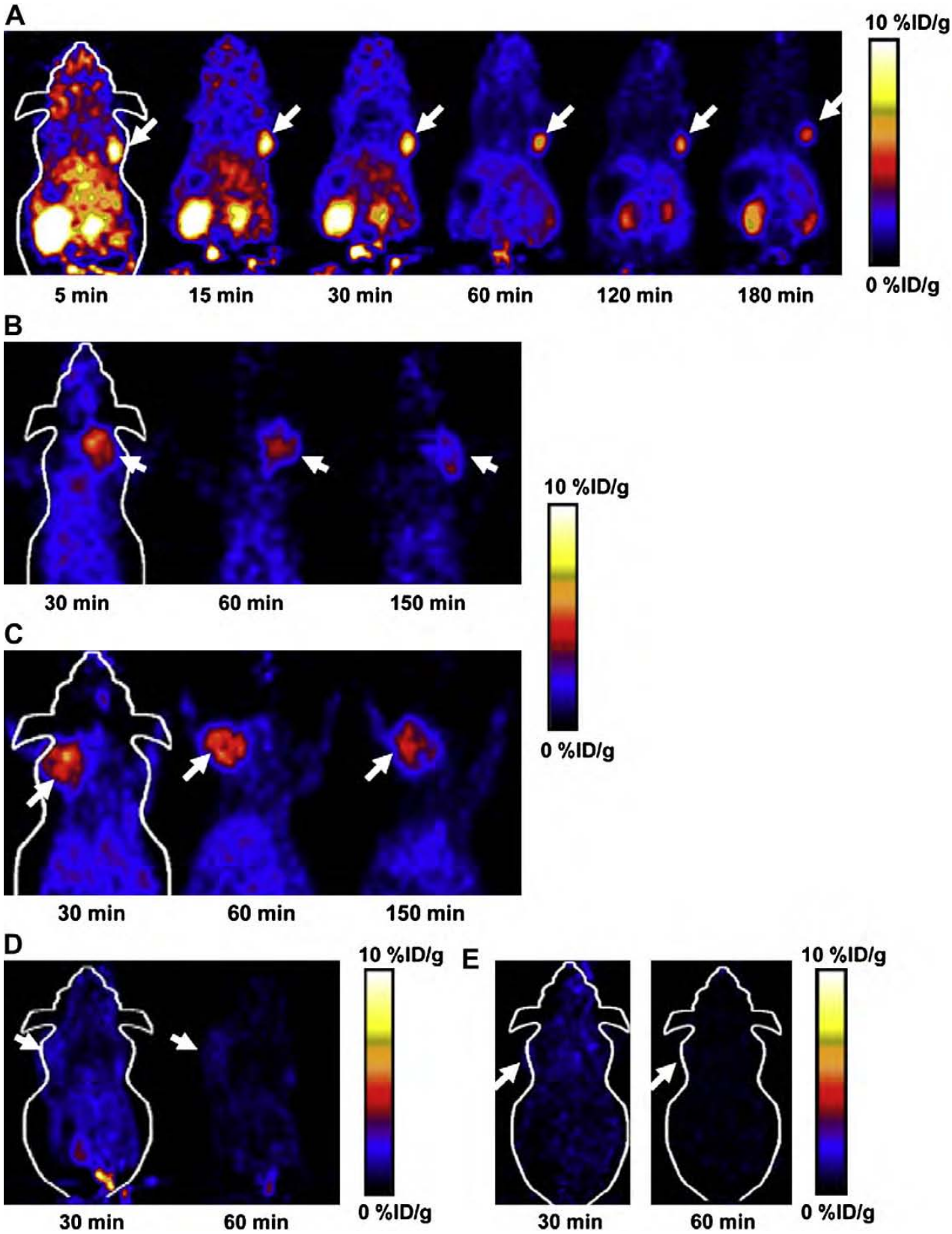

Fig. 2. (*A*) Decay-corrected whole-body coronal microPET images of athymic female nude mice bearing U87MG tumor at 5, 15, 30, 60, 120, and 180 minutes after injection of ^{18}F-FPRGD4 [3.7 MBq (100 μCi)]. (*B*) Decay-corrected whole-body coronal microPET images of c-neu oncomice at 30, 60, and 150 minutes (5-minute static image) after intravenous injection of ^{18}F-FPRGD4. (*C*) Decay-corrected whole-body coronal microPET images of orthotopic MDA-MB-435 tumor-bearing mouse at 30, 60, and 150 minutes after intravenous injection of ^{18}F-FPRGD4. (*D*) Decay-corrected whole-body coronal microPET images of DU-145 tumor-bearing mouse (5-minute static image) after intravenous injection of ^{18}F-FPRGD4. (*E*) Coronal microPET images of a U87MG tumor-bearing mouse at 30 and 60 minutes after coinjection of ^{18}F-FPRGD4 and a blocking dose of c(RGDyK). Arrows indicate tumors in all cases. (*From* Wu Z, Li ZB, Chen K, et al. MicroPET of tumor integrin $\alpha_v\beta_3$ expression using ^{18}F-labeled PEGylated tetrameric RGD peptide (^{18}F-FPRGD4). J Nucl Med 2007;48(9):1540; with permission.)

Author's personal copy

in a Wister rat model. PET imaging and autoradiography revealed focal accumulation in the infarct area started at day 3, peaked between 1 and 3 weeks, and decreased to day 3 level at 6 months after reperfusion. The time course of focal tracer uptake paralleled vascular density as measured by CD31 immunohistochemical analysis, indicating that ^{18}F-Galacto-RGD is promising for the monitoring of myocardial repair processes.[153] The results from this study encourage the application of RGD-PET imaging to monitor the angiogenesis in other noncancer diseases.

PET imaging of VEGF and its receptors

VEGF, a potent mitogen in embryonic and somatic angiogenesis, plays a pivotal role in both normal vascular tissue development and many disease processes.[154,155] The VEGF family is composed of seven members with a common VEGF homology domain: VEGF-A, -B, -C, -D, -E, -F, and placenta growth factor.[5] VEGF-A is a dimeric, disulfide-bound glycoprotein existing in at least seven homodimeric isoforms, consisting of 121, 145, 148, 165, 183, 189, or 206 amino acids. Besides the difference in molecular weight, these isoforms also differ in their biologic properties such as the ability to bind to cell-surface heparin-sulfate proteoglycans.[5]

The angiogenic actions of VEGF are mainly mediated via two endothelium-specific receptor tyrosine kinases, Flt-1 (VEGFR-1) and Flk-1/KDR (VEGFR-2).[156] Both VEGFRs are largely restricted to vascular endothelial cells and all VEGF-A isoforms bind to both VEGFR-1 and VEGFR-2. It is now generally accepted that VEGFR-1 is critical for physiologic and developmental angiogenesis and its function varies with the stages of development, the states of physiologic and pathologic conditions, and the cell types in which it is expressed.[5,155] VEGFR-2 is the major mediator of the mitogenic, angiogenic, and permeability-enhancing effects of VEGF. Over-expression of VEGF and VEGFRs has been implicated as poor prognostic markers in various clinical studies.[5] Agents that prevent VEGF-A binding to its receptors,[157] antibodies that directly block VEGFR-2[158,159] and small molecules that inhibit the kinase activity of VEGFR-2 and thereby block growth factor signaling,[65,160,161] are all currently under active development. The critical role of VEGF-A in cancer progression has been highlighted by the approval of the humanized anti-VEGF monoclonal antibody bevacizumab for first-line cancer treatment.[162] Development of VEGF- or VEGFR-targeted molecular imaging probes could serve as a new paradigm for the assessment of anti-angiogenic therapeutics and for better understanding the role and expression profile of VEGF/VEGFR in many angiogenesis-related diseases. VEGF/VEGFR has been imaged by various imaging modalities, though PET is the dominant technique for direct VEGF/VEGFR imaging.[163] In the clinical setting, the right timing can be critical for VEGFR-targeted cancer therapy and noninvasive imaging of VEGF/VEGFR can help in determining whether to start and when to start VEGFR-targeted treatment. With the development of new tracers with better targeting efficacy and desirable pharmacokinetics, clinical translation will be critical for the maximum benefit of VEGF-based imaging agents.

VEGF imaging has been investigated, especially with radiolabeled-specific antibodies.[164] VG76e, an IgG1 monoclonal antibody that binds to human VEGF, was labeled with ^{124}I for PET imaging of solid tumor xenografts in immune-deficient mice.[165] Whole-animal PET imaging studies revealed a high tumor-to-background contrast. Although VEGF specificity in vivo was demonstrated in this report, the poor immunoreactivity (< 35%) of the radiolabeled antibody limits the potential use of this tracer. HuMV833, the humanized version of a mouse monoclonal anti-VEGF antibody MV833, was also labeled with ^{124}I and the distribution and biologic effects of HuMV833 in patients in a phase I clinical trial were investigated.[166] Patients with progressive solid tumors were treated with various doses of HuMV833, and PET imaging using ^{124}I-HuMV833 was performed to measure the antibody distribution in and clearance from tissues. It was found that antibody distribution and clearance were quite heterogeneous not only between and within patients but also between and within individual tumors. Bevacizumab, a humanized monoclonal antibody against VEGF, has been labeled with ^{111}In to image VEGF-A expression in nude mice models or patients with colorectal liver metastases.[167] Although enhanced uptake of ^{111}In-bevacizumab in the liver metastases was observed in 9 of the 12 patients, there was no correlation between the level of ^{111}In-antibody accumulation and the level of VEGF-A expression in the tissue, as determined by in situ hybridization and ELISA.[167]

Bevacizumab has also been labeled with the PET isotope ^{89}Zr for noninvasive in vivo VEGF visualization and quantification. On small-animal PET images, radiolabeled bevacizumab showed higher uptake compared with radiolabeled human IgG in a human SKOV-3 ovarian tumor xenograft. Tracer uptake in other organs was seen primarily in the liver and spleen (**Fig. 3**).[164] A recent study showed that there was a significant ^{18}F-FDG kinetics correlation between k1 (the transport coefficient) and VEGF-A mRNA level determined

Author's personal copy

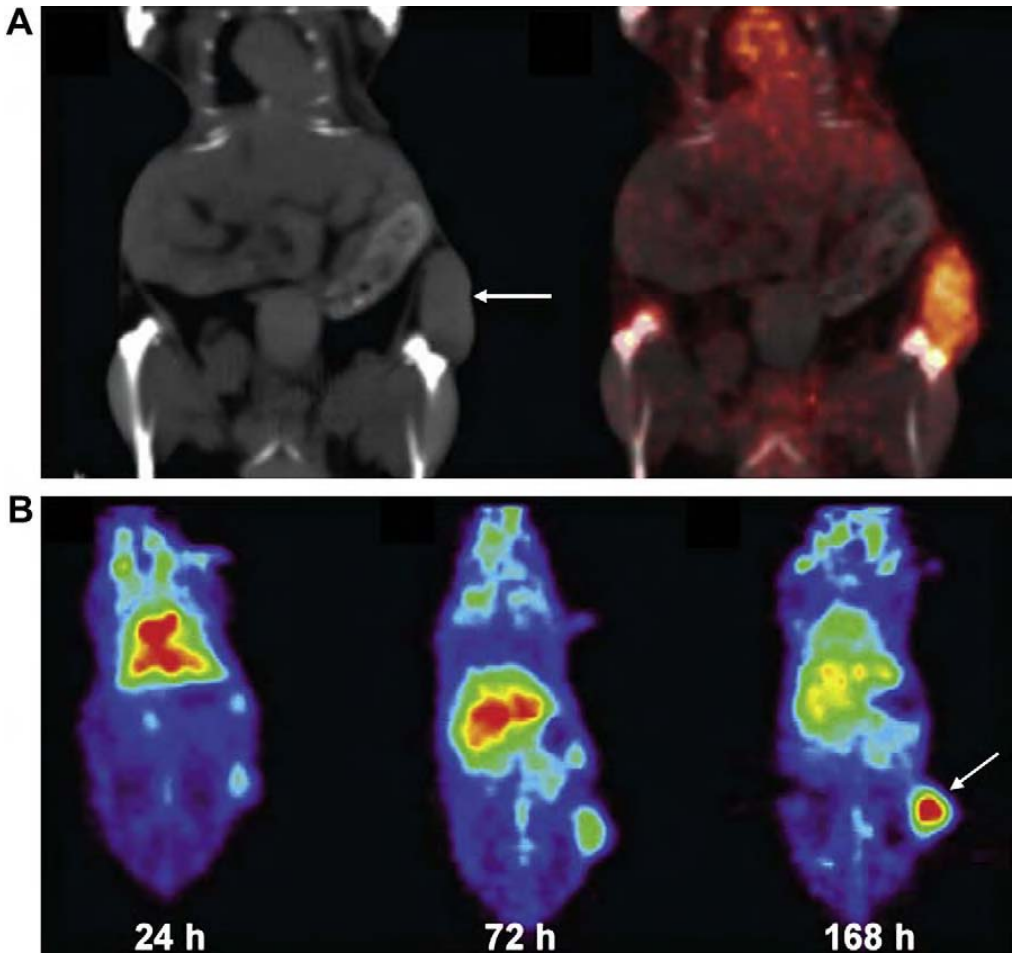

Fig. 3. (*A*) Coronal CT image and fusion of microPET and CT images (168 hours after injection) enables adequate quantitative measurement of ^{89}Zr-bevacizumab in the tumor. (*B*) Coronal planes of microPET images after injection of ^{89}Zr-bevacizumab. *Arrows* indicate SKOV-3 tumors. (*Reproduced from* Nagengast WB, de Vries EG, Hospers GA, et al. In vivo VEGF imaging with radiolabeled bevacizumab in a human ovarian tumor xenograft. J Nucl Med 2007;48(8):1316; with permission.)

by gene chip assay ($r = 0.51$), indicating the possibility to predict the gene expression of VEGF-A with the regression functions from the FDG-PET parameters.[168]

VEGF/VEGFR interactions is one of the most extensively studied angiogenesis-related signaling pathways.[163] The alternative to overcome the difficulty induced by the soluble and more dynamic nature of VEGF is to image VEGFRs, other indicators of angiogenesis that have superior accessibility. VEGF isoforms exist in nature and have very strong binding affinity and specificity to VEGFRs.[163,169] Therefore, a generic strategy is to label these VEGF isoforms with radionuclides to image VEGFR expression. $VEGF_{121}$ is a soluble, nonheparin-binding variant that exists in solution as a disulfide-linked homodimer containing the full biologic and receptor-binding activity of the larger variants.[5] $VEGF_{121}$ has been labeled with ^{64}Cu ($t_{1/2}$ = 12.7 hours) for PET imaging of tumor angiogenesis and VEGFR expression.[170] DOTA-$VEGF_{121}$ exhibited nanomolar receptor-binding affinity (comparable to $VEGF_{121}$) in vitro. MicroPET imaging revealed rapid, specific, and prominent uptake of ^{64}Cu-DOTA-$VEGF_{121}$ (10%～15%ID/g) in highly vascularized small U87MG tumor (60 mm^3) with high VEGFR-2 expression but significantly lower and sporadic uptake (～3%ID/g) in large U87MG tumor (1,200 mm^3) with low VEGFR-2 expression (**Fig. 4**). Western blotting of tumor tissue lysate, immunofluorescence staining, and blocking studies with unlabeled $VEGF_{121}$ confirmed that the tumor uptake is VEGFR-specific. This was the first report on PET imaging of VEGFR expression. This study also demonstrated the dynamic nature of VEGFR expression during tumor progression in that even for the same tumor model, VEGFR expression level can be dramatically different at different stages. Successful demonstration of the ability of ^{64}Cu-DOTA-$VEGF_{121}$ to visualize VEGFR expression in vivo should allow for clinical translation of this tracer to image tumor angiogenesis and to guide VEGFR-targeted cancer therapy.[170]

Author's personal copy

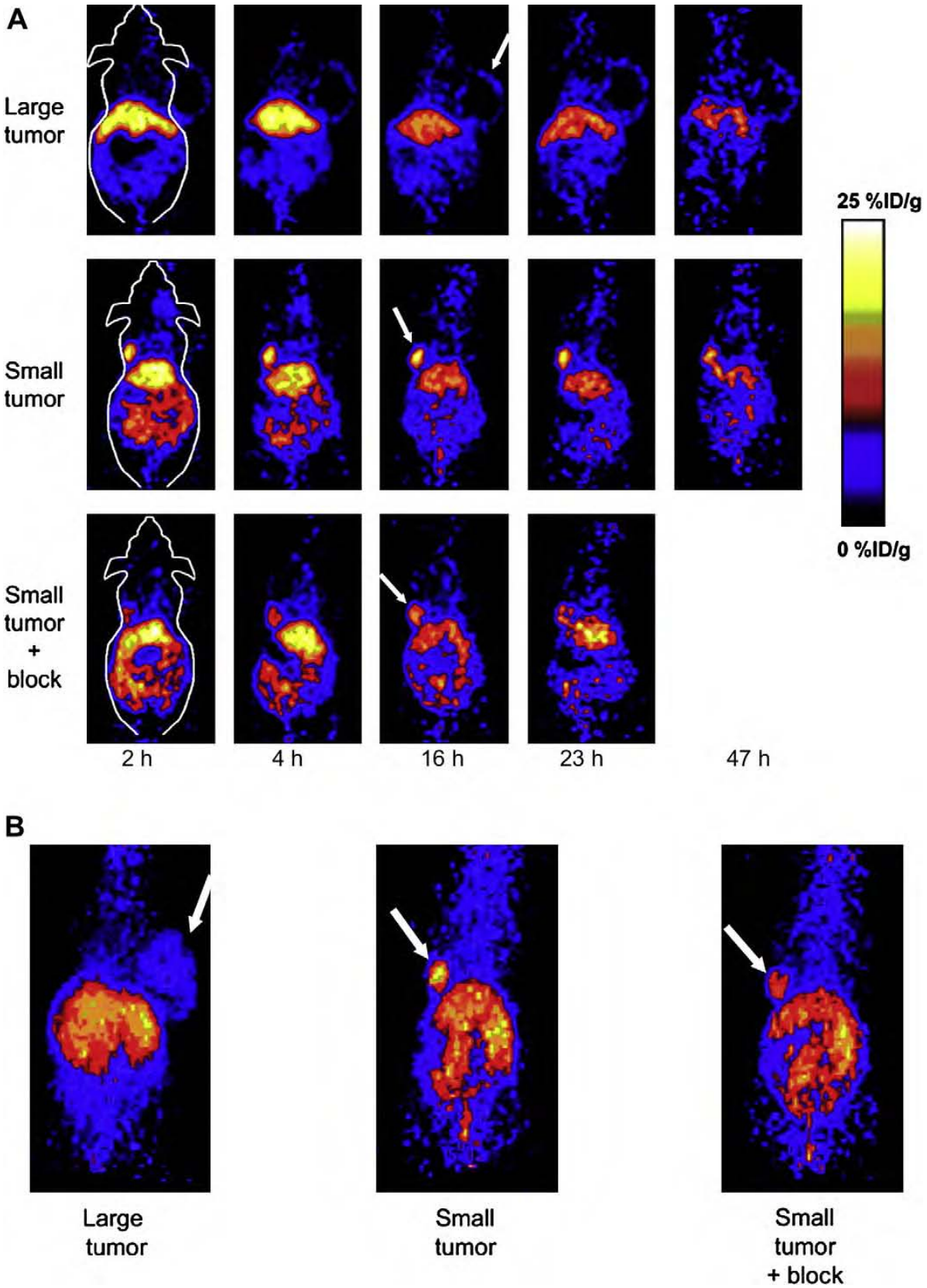

Fig. 4. MicroPET of ^{64}Cu-DOTA-VEGF$_{121}$ in U87MG tumor-bearing mice. (*A*) Serial microPET scans of large and small U87MG tumor-bearing mice injected intravenously with 5 MBq to 10 MBq of ^{64}Cu-DOTA-VEGF$_{121}$. Mice injected with ^{64}Cu-DOTA-VEGF$_{121}$ 30 minutes after injection of 100 μg VEGF$_{121}$ are also shown (denoted as "small tumor + block"). (*B*) Two-dimensional whole-body projection of the three mice shown in (*A*) at 16 hours after injection of ^{64}Cu-DOTA-VEGF$_{121}$. Tumors are indicated by arrows. (*Reproduced from* Cai W, Chen K, Mohamedali KA, et al. PET of vascular endothelial growth factor receptor expression. J Nucl Med 2006;47(12):2052; with permission.)

Author's personal copy

Further studies showed that the uptake of ^{64}Cu-DOTA-VEGF$_{121}$ in the tumor peaked when the tumor size was about 100 mm^3 to 250 mm^3. Both small and large tumors had lower tracer uptake, indicating a narrow range of tumor size with high VEGFR-2 expression.[171] In another follow-up study, a VEGFR-specific fusion toxin VEGF$_{121}$/rGel (composed of VEGF$_{121}$ linked with a G$_4$S tether to recombinant plant toxin gelonin) was used to treat orthotopic glioblastoma in a mouse model.[169] Before initiation of treatment, microPET imaging with ^{64}Cu-labeled VEGF$_{121}$/rGel was performed to evaluate the tumor targeting efficacy and the pharmacokinetics. It was found that ^{64}Cu-DOTA-VEGF$_{121}$/rGel exhibited high tumor accumulation and retention and high tumor-to-background contrast up to 48 hours after injection in glioblastoma xenografts. Based on the in vivo pharmacokinetics of ^{64}Cu-DOTA-VEGF$_{121}$/rGel, VEGF$_{121}$/rGel was administered every other day for the treatment of orthotopic U87MG glioblastomas. Histologic analysis revealed specific tumor neovasculature damage after treatment with four doses of VEGF$_{121}$/rGel.[169] ^{64}Cu was also used to site-specifically label VEGF$_{121}$ and it was found that PEGylation showed considerably prolonged blood clearance. Compared with ^{99m}Tc-labeled analog where the tumor uptake (~2%ID/g) was lower than most of the normal organs and the kidney uptake was about 120%ID/g, the PEGylated version gave higher tumor uptake (~2.5%ID/g) and lower kidney uptake at about 65%ID/g.[172]

PET imaging using radiolabeled VEGF can also play a role in other angiogenesis-related diseases besides cancer. Myocardial infarction can lead to the activation of many biologic pathways, including VEGF/VEGFR signaling.[173,174] Using the previously validated PET tracer ^{64}Cu-DOTA-VEGF$_{121}$, the kinetics of VEGFR expression was imaged for the first time in living subjects using a rat model of myocardial infarction.[175] Myocardial infarction was induced by ligation of the left anterior descending coronary artery in Sprague-Dawley rats and confirmed by ultrasound. ^{64}Cu-DOTA-VEGF$_{121}$ PET scans were performed before myocardial infarction induction, and at days 3, 10, 17, and 24 after myocardial infarction induction. Baseline myocardial uptake of ^{64}Cu-DOTA-VEGF$_{121}$ was minimal (0.3 $\pm$ 0.1%ID/g). After myocardial infarction, ^{64}Cu-DOTA-VEGF$_{121}$ myocardial uptake significantly increased (up to 1.0 $\pm$ 0.1%ID/g) and was elevated for 2 weeks, after which it returned to baseline levels. In a hindlimb ischemia model, PET imaging showed significantly higher ^{64}Cu-DOTA-VEGF$_{121}$ uptake in ischemic hindlimbs than in nonischemic hindlimbs. Treadmill exercise training was also found to increase ^{64}Cu-DOTA-VEGF$_{121}$ uptake in ischemic hindlimbs compared with nonexercised hindlimbs.[176] With ^{64}Cu-DOTA-VEGF$_{121}$ PET imaging, the authors have evaluated the VEGFR expression kinetics noninvasively in a rat stroke model. The results revealed that the tracer uptake in the stroke border zone peaked at approximately 10 days after surgery, indicating neovascularization as confirmed by histology (VEGFR-2, BrdU, and lectin staining).[177]

All VEGF-A isoforms bind to both VEGFR-1 and VEGFR-2.[5] In the imaging studies reported to date, specificity to either VEGFR-1 or VEGFR-2 has rarely been achieved as most of the tracers are based on VEGF isoforms. Kidneys have high VEGFR-1 expression that can take up VEGF-A based tracer, which thus usually make it the dose-limiting organ.[170,178] Alanine-scanning mutagenesis has been used to identify a positively charged surface in VEGF$_{165}$ that mediates the binding to VEGFR-2.[179] Arg^{82}, Lys^{84}, and His^{86}, located in a hairpin loop, were found to be critical for binding VEGFR-2, while negatively charged residues, Asp^{63}, Glu^{64}, and Glu^{67}, were associated with VEGFR-1 binding. Mutations in the 63 to 67 region of VEGF exhibited only modest effects on VEGFR-2 binding but significant reduction in affinity with VEGFR-1. Recently, the authors laboratory engineered a D63AE64AE67A mutant of VEGF$_{121}$ (VEGF$_{DEE}$) by recombinant DNA technology to develop a VEGFR-2-specific PET tracer. Cell-binding assay demonstrated that VEGF$_{DEE}$ had about 20-fold lower VEGFR-1 binding affinity and only slightly lower VEGFR-2 binding affinity as compared with VEGF$_{121}$. Both ^{64}Cu-DOTA-VEGF$_{121}$ and ^{64}Cu-DOTA-VEGF$_{DEE}$ had rapid and prominent activity accumulation in VEGFR-2-expressing 4T1 tumors. However, the renal uptake of ^{64}Cu-DOTA-VEGF$_{DEE}$ was significantly lower than that of ^{64}Cu-DOTA-VEGF$_{121}$ as rodent kidneys expressed high levels of VEGFR-1, indicating that VEGF$_{DEE}$ is superior to wild-type VEGF$_{121}$ for imaging tumor angiogenesis.[180] The DOTA conjugation of VEGF proteins in this study is random instead of site-specific. It will be critical to further develop more potent VEGFR-2 specific mutants, site-specifically label VEGF analog proteins with various isotopes including ^{64}Cu, to improve angiogenesis imaging quality and result analysis.[175]

Imaging of matrix metalloproteinases

MMPs are a family of zinc- and calcium-dependent endopeptidases that are responsible for the enzymatic degradation of connective tissue und thus facilitate endothelial cell migration during

Author's personal copy

angiogenesis.[181] Additionally, MMPs process and release bioactive molecules, such as growth factors, proteinase inhibitors, cytokines and chemokines.[182] From the more than 18 members of the MMP family, the gelatinases MMP-2 and -9 are most consistently detected in malignancies.[117] In the progression of the atherosclerotic lesions, MMP-3 and -9 have been shown to limit plaque growth and promote a stable plaque phenotype, and MMP-12 supports atherosclerotic lesion expansion and destabilization.[183] Many strategies have been developed to image MMPs level for the assessment of angiogenesis.[184,185]

The so-called "smart probes" have been developed to contain fluorescent dyes and MMP-cleavable sequences.[186,187] It has been reported a MMP-2-sensitive probe was activated by MMP-2 in vitro, producing up to an 850% increase in near-infrared fluorescent signal intensity, and MMP-2-positive tumors were easily identified as high-signal-intensity regions as early as 1 hour after intravenous injection of the MMP-2 probe.[188]

Via phage display techniques, the MMP-specific decapeptide H-Cys-Thr-Thr-His-Trp-Gly-Phe-Thr-leu-Cys-OH (CTT) was found and could be labeled with ^{125}I and ^{99m}Tc. However, this tracer has unfavorable characteristics for in vivo imaging because the metabolic stability of the compound is low and lipophilicity is high.[189] Another group labeled this peptide with ^{111}In after conjugating it with a highly hydrophilic and negatively charged chelator DTPA. A significant correlation was observed between the accumulation in the tumor as well as tumor-to-blood ratio of ^{111}In-DTPA-CTT and gelatinase activity. Moreover, ^{111}In-DTPA-CTT showed low levels of radioactivity in the liver and kidneys.[190] CTT peptide also has been labeled with ^{64}Cu after DOTA conjugation for PET imaging of MMP. ^{64}Cu-DOTA-CTT inhibited hMMP-2 and mMMP-9 with similar affinity to CTT. MicroPET imaging studies showed that ^{64}Cu-DOTA-CTT was taken up by MMP-2/9-positive B16F10 murine melanoma tumors, however, the low affinity for MMP-2 and MMP-9 and in vivo instability of CTT-based imaging probes need to be overcome for further applications.[191]

Another approach is to label small-molecule MMP inhibitors (MMPIs), which are typically used as antiangiogenic drugs. In general, MMPIs possess a zinc-binding group complexing the zinc ion of the active site and are classified into several groups because of their lead structures.[181] Different ^{18}F and ^{11}C labeled MMPIs have been synthesized and evaluated preclinically with mixed results.[192,193] Fluorinated MMPIs based on lead structures of the broad-spectrum inhibitors N-hydroxy-2(R)-[[(4-methoxyphenyl)sulfonyl](benzyl)-amino]-3-methyl-butanamide (CGS 25,966) and N-hydroxy-2(R)-[[(4-methoxyphenyl)sulfonyl](3-picolyl)-amino]-3-methyl-butanamide (CGS 27,023A) have been synthesized and showed high in vitro MMP inhibition potencies for MMP-2, -8, -9, and -13.[194] However, in vivo microPET study with ^{11}C-CGS 25,966 failed to demarcate MMP-positive tumors.[195] A ^{11}C-labeled MMPI (2R)-2-[[4-(6-fluorohex-1-ynyl)phenyl]sulfonylamino]-3-methylbutyric acid ^{11}C-methyl ester (^{11}C-FMAME), has also been synthesized and applied to two animal models of breast cancer, MCF-7 xenograft transfected with interleukin-1 and MDA-MB-435 xenograft in athymic mice. Again, low tumor-to-blood and tumor-to muscle ratios of these tracers do not allow visualization of the tumors in microPET studies.[192,196] However, biodistribution study with ^{18}F-labeled similar compound, (2R)-2-[4-(6-^{18}F-Fluorohex-1-ynyl)-benzenesulfonylamino]-3-methylbutyric acid (^{18}F-SAV03), showed higher tumor uptake of the tracer than normal organs.[193] Other MMPIs have also been synthesized and labeled with radionuclides including ^{111}In and ^{18}F.[194,197] Nevertheless, significant improvements in tumor MMP targeting and in vivo pharmacokinetics are necessary before the use of MMP-radiotracer imaging will be translated into the clinic.

Imaging of other angiogenesis-related targets

Fibronectin is a large glycoprotein, which can be found physiologically in plasma and tissues. However, the extra-domain B of fibronectin (EDB), consisting of 91 amino acids, is not present in the fibronectin molecule under normal conditions, except for the endometrium in the proliferative phase and some vessels of the ovaries. EDB is interesting as a marker of angiogenesis as it is expressed in a variety of solid tumors, as well as in ocular angiogenesis and wound healing.[198] The human antibody fragment scFv(L19) has been shown to efficiently localize on neovasculature both in animal models and in cancer patients. In a study with patients suffering from various solid tumors, 16 of 20 tumor lesions could be identified by SPECT using ^{123}I-scFv(L19). Whether the unidentified tumors were not detected because they were either in a phase of slow growth with low levels of angiogenesis, or because of the technical limitations of SPECT imaging, is not clear.[199] No reports about PET tracers targeting EDB are available up to now. Other angiogenesis-related biomarkers, such as angiopoietins/Tie receptors,[200] and CD276[201] are also potential targets for angiogenesis imaging. Angiopoietins/Tie receptors are involved in regulation of complex

Author's personal copy

interactions between endothelium and surrounding cells. CD276 has been observed to be over-expressed in tumor versus normal endothelium.

SUMMARY AND PERSPECTIVE

Numerous imaging techniques are available for assessing tissue vasculature on a structural, functional, and molecular level. A wide variety of targeting ligands (small molecules, peptides, peptidomimetics, and antibodies) have been conjugated with various imaging labels for MR imaging, US, optical, SPECT, PET, and multimodality imaging of angiogenesis. All these methods have been successfully used preclinically and will hopefully aid in antiangiogenic drug evaluation in animal studies. Because of its high sensitivity and the low amounts of tracer that have to be used, PET will probably be the first to be used on a wide scale in patients in the intermediate term. In addition, toxicity issues of PET tracers are of less importance compared with MR imaging or US imaging probes as only pica molar amount will be used for imaging purpose. However, it is likely that not one single parameter, target structure, or imaging technique will be used for the assessment of angiogenesis in the future, but rather a multimodality, multiplexing imaging that will allow for evaluation of the angiogenic cascade in its full complexity to acquire comprehensive information. It is predictable that the new generation clinical PET/CT and microPET/microCT, as well as PET/MR imaging and microPET/microMR imaging currently in active development,[202–204] will likely play a major role in molecular imaging of angiogenesis for the years to come.

Although it is generally assumed that noninvasive imaging results correlate with the target expression level, such assumption has not been extensively validated. In most reports, two tumor models are studied, where one acts as a positive control and the other as a negative control. Quantitative correlation between the target expression level in vivo and the noninvasive imaging data is rare.[137,145,205,206] Such correlation is critical for future therapeutic response monitoring, as it would be ideal to be able to monitor the changes in the target expression level quantitatively, rather than qualitatively, in each individual patient. Lack of accurate quantification is one of the hindrances why only a few radiotracers including PET tracers have been used in human beings up to now, and their role in assessment of anti- or proangiogenic therapies is still unsettled.

To further improve imaging of the angiogenesis process at molecular level, it is necessary to identify new angiogenesis-related targets and corresponding specific ligands and to optimize currently available imaging probes. Thorough and full understanding of the physiologic and pathologic changes during angiogenesis will be critical for new target identification. Optimization of currently available imaging probes can be achieved in several ways. First, oligomerization (homo or hetero) the targeting ligand (typically peptide) can improve the binding affinity as well as tissue retention, likely because of the polyvalency effect.[207] Second, site-specific labeling may be advantageous than randomly labeling on lysine residues in terms of retaining the binding affinity and functional activity.[175] Third, incorporation of a linker between the targeting ligand and the label can improve the pharmacokinetic properties. Glycosylation, PEGylation, and various other linkers have been shown to improve the imaging quality. Last, development of new strategies to improve the labeling yield (most applicable to ^{18}F-based tracers) is critical for future clinical studies. To foster the continued discovery and development of angiogenesis-targeted imaging agents, cooperative efforts are needed from cellular and molecular biologists to identify and validate novel imaging targets, chemists and radiochemists to synthesize and characterize the imaging probes, and engineers and medical physicists and mathematicians to develop high-sensitivity and high-resolution imaging devices and hybrid instruments and better image reconstruction algorithms.

Noninvasive imaging of angiogenesis has clinical applications in many aspects, including lesion detection, patient stratification, new drug development and validation, treatment monitoring, and dose optimization. For example, glucosamino ^{99m}Tc-d-c(RGDfK) gamma-camera imaging has been applied to monitor the therapeutic efficacy of paclitaxel in Lewis lung carcinoma tumor-bearing mice.[208] With the development of new tracers with better targeting efficacy and desirable pharmacokinetics, clinical translation will be critical for the maximum benefit of these imaging probes. Most of the molecular imaging probes suffer from the slow translation from bench to bedside. Multiple steps in preclinical development, especially the investigational new drug-directed toxicology, significantly slowed down the process of converting a newly developed agent into a diagnostic imaging probe for clinical testing. The high specificity required for molecular imaging not only leads to higher costs of development but also smaller market potential, which may

Author's personal copy

make them considered too risky by investors for commercial development. However, the situation has gradually changed over the last several years thanks to the continued development and wider availability of scanners dedicated to small-animal imaging studies, as well as the exploratory investigational new drug mechanism proposed by the FDA to allow faster first-in-human studies. Now the molecular imaging techniques can bridge the gap between preclinical and clinical research to develop candidate drugs that have the optimal target specificity, pharmacodynamics, and efficacy. It is expected that in the foreseeable future, anigogenesis imaging with PET tracers will be routinely applied in anticancer clinical trials, paving the way to personalized molecular therapy.

REFERENCES

1. Folkman J. Angiogenesis in cancer, vascular, rheumatoid and other disease. Nat Med 1995;1(1): 27–31.
2. Atluri P, Woo YJ. Pro-angiogenic cytokines as cardiovascular therapeutics: assessing the potential. BioDrugs 2008;22(4):209–22.
3. Pathak AP, Gimi B, Glunde K, et al. Molecular and functional imaging of cancer: advances in MRI and MRS. Methods Enzymol 2004;386:3–60.
4. Rajagopalan S, Trachtenberg J, Mohler E, et al. Phase I study of direct administration of a replication deficient adenovirus vector containing the vascular endothelial growth factor cDNA (CI-1023) to patients with claudication. Am J Cardiol 2002; 90(5):512–6.
5. Ferrara N. Vascular endothelial growth factor: basic science and clinical progress. Endocr Rev 2004; 25(4):581–611.
6. Hurwitz H, Fehrenbacher L, Novotny W, et al. Bevacizumab plus irinotecan, fluorouracil, and leucovorin for metastatic colorectal cancer. N Engl J Med 2004;350(23):2335–42.
7. Kerbel RS. Antiangiogenic therapy: a universal chemosensitization strategy for cancer? Science 2006;312(5777):1171–5.
8. Faivre S, Demetri G, Sargent W, et al. Molecular basis for sunitinib efficacy and future clinical development. Nat Rev Drug Discov 2007;6(9):734–45.
9. Jaffe CC. Measures of response: RECIST, WHO, and new alternatives. J Clin Oncol 2006;24(20): 3245–51.
10. Cai W, Rao J, Gambhir SS, et al. How molecular imaging is speeding up anti-angiogenic drug development. Mol Cancer Ther 2006;5(11): 2624–33.
11. Choe YS, Lee KH. Targeted in vivo imaging of angiogenesis: present status and perspectives. Curr Pharm Des 2007;13(1):17–31.
12. Haubner R. Noninvasive tracer techniques to characterize angiogenesis. Handb Exp Pharmacol 2008;185(II):323–39.
13. Berthelot T, Lasne MC, Deleris G. New trends in molecular imaging of tumor angiogenesis. Anticancer Agents Med Chem 2008;8(5):497–522.
14. Auguste P, Lemiere S, Larrieu-Lahargue F, et al. Molecular mechanisms of tumor vascularization. Crit Rev Oncol Hematol 2005;54(1):53–61.
15. Carmeliet P. Mechanisms of angiogenesis and arteriogenesis. Nat Med 2000;6(4):389–95.
16. Holash J, Maisonpierre PC, Compton D, et al. Vessel cooption, regression, and growth in tumors mediated by angiopoietins and VEGF. Science 1999;284(5422):1994–8.
17. Folkman J. Tumor angiogenesis: therapeutic implications. N Engl J Med 1971;285(21):1182–6.
18. Kalluri R. Basement membranes: structure, assembly and role in tumour angiogenesis. Nat Rev Cancer 2003;3(6):422–33.
19. Bergers G, Benjamin LE. Tumorigenesis and the angiogenic switch. Nat Rev Cancer 2003;3(6):401–10.
20. Nguyen M. Angiogenic factors as tumor markers. Invest New Drugs 1997;15(1):29–37.
21. Landgren E, Schiller P, Cao Y, et al. Placenta growth factor stimulates MAP kinase and mitogenicity but not phospholipase C-gamma and migration of endothelial cells expressing Flt 1. Oncogene 1998;16(3):359–67.
22. Nor JE, Christensen J, Mooney DJ, et al. Vascular endothelial growth factor (VEGF)-mediated angiogenesis is associated with enhanced endothelial cell survival and induction of Bcl-2 expression. Am J Pathol 1999;154(2):375–84.
23. Paku S, Paweletz N. First steps of tumor-related angiogenesis. Lab Invest 1991;65(3):334–46.
24. Djonov V, Schmid M, Tschanz SA, et al. Intussusceptive angiogenesis: its role in embryonic vascular network formation. Circ Res 2000;86(3):286–92.
25. Metzger RJ, Krasnow MA. Genetic control of branching morphogenesis. Science 1999; 284(5420):1635–9.
26. Pepper MS, Ferrara N, Orci L, et al. Vascular endothelial growth factor (VEGF) induces plasminogen activators and plasminogen activator inhibitor-1 in microvascular endothelial cells. Biochem Biophys Res Commun 1991;181(2):902–6.
27. Asahara T, Chen D, Takahashi T, et al. Tie2 receptor ligands, angiopoietin-1 and angiopoietin-2, modulate VEGF-induced postnatal neovascularization. Circ Res 1998;83(3):233–40.
28. Brooks PC, Clark RA, Cheresh DA. Requirement of vascular integrin $a_v b_3$ for angiogenesis. Science 1994;264(5158):569–71.
29. Friedlander M, Brooks PC, Shaffer RW, et al. Definition of two angiogenic pathways by distinct alpha v integrins. Science 1995;270(5241):1500–2.

Author's personal copy

30. Sang QX. Complex role of matrix metalloproteinases in angiogenesis. Cell Res 1998;8(3):171–7.
31. Gamble J, Meyer G, Noack L, et al. B1 integrin activation inhibits in vitro tube formation: effects on cell migration, vacuole coalescence and lumen formation. Endothelium 1999;7(1):23–34.
32. Nakao N, Miura K, Takayasu Y, et al. CT angiography in hepatocellular carcinoma. J Comput Assist Tomogr 1983;7(5):780–7.
33. Less JR, Skalak TC, Sevick EM, et al. Microvascular architecture in a mammary carcinoma: branching patterns and vessel dimensions. Cancer Res 1991;51(1):265–73.
34. Konerding MA, Miodonski AJ, Lametschwandtner A. Microvascular corrosion casting in the study of tumor vascularity: a review. Scanning Microsc 1995;9(4): 1233–43.
35. Schlingemann RO, Rietveld FJ, Kwaspen F, et al. Differential expression of markers for endothelial cells, pericytes, and basal lamina in the microvasculature of tumors and granulation tissue. Am J Pathol 1991;138(6):1335–47.
36. Miettinen M, Lindenmayer AE, Chaubal A. Endothelial cell markers CD31, CD34, and BNH9 antibody to H- and Y-antigens–evaluation of their specificity and sensitivity in the diagnosis of vascular tumors and comparison with von Willebrand factor. Mod Pathol 1994;7(1):82–90.
37. Schlaeger TM, Bartunkova S, Lawitts JA, et al. Uniform vascular-endothelial-cell-specific gene expression in both embryonic and adult transgenic mice. Proc Natl Acad Sci U S A 1997;94(7): 3058–63.
38. Motoike T, Loughna S, Perens E, et al. Universal GFP reporter for the study of vascular development. Genesis 2000;28(2):75–81.
39. Trotter MJ, Olive PL, Chaplin DJ. Effect of vascular marker Hoechst 33342 on tumour perfusion and cardiovascular function in the mouse. Br J Cancer 1990;62(6):903–8.
40. Hashizume H, Baluk P, Morikawa S, et al. Openings between defective endothelial cells explain tumor vessel leakiness. Am J Pathol 2000;156(4):1363–80.
41. Usami N, Iwano S, Yokoi K. Solitary fibrous tumor of the pleura: evaluation of the origin with 3D CT angiography. J Thorac Oncol 2007;2(12):1124–5.
42. McDonald DM, Choyke PL. Imaging of angiogenesis: from microscope to clinic. Nat Med 2003; 9(6):713–25.
43. van Vliet M, van Dijke CF, Wielopolski PA, et al. MR angiography of tumor-related vasculature: from the clinic to the micro-environment. Radiographics 2005;25(Suppl 1):S85–97 [discussion: S97–8].
44. Boudghene FP, Gouny P, Tassart M, et al. Subungual glomus tumor: combined use of MRI and three-dimensional contrast MR angiography. J Magn Reson Imaging 1998;8(6):1326–8.
45. Foster FS, Burns PN, Simpson DH, et al. Ultrasound for the visualization and quantification of tumor microcirculation. Cancer Metastasis Rev 2000; 19(1-2):131–8.
46. Jiang Y, Zhao J, White DL, et al. Micro CT and Micro MR imaging of 3D architecture of animal skeleton. J Musculoskelet Neuronal Interact 2000;1(1):45–51.
47. Tozer GM, Ameer-Beg SM, Baker J, et al. Intravital imaging of tumour vascular networks using multi-photon fluorescence microscopy. Adv Drug Deliv Rev 2005;57(1):135–52.
48. Galbraith SM. Antivascular cancer treatments: imaging biomarkers in pharmaceutical drug development. Br J Radiol 2003;76(Spec No 1):S83–6.
49. Choyke PL, Dwyer AJ, Knopp MV. Functional tumor imaging with dynamic contrast-enhanced magnetic resonance imaging. J Magn Reson Imaging 2003;17(5):509–20.
50. O'Connor JP, Jackson A, Parker GJ, et al. DCE-MRI biomarkers in the clinical evaluation of antiangiogenic and vascular disrupting agents. Br J Cancer 2007;96(2):189–95.
51. Zhang C, Jugold M, Woenne EC, et al. Specific targeting of tumor angiogenesis by RGD-conjugated ultrasmall superparamagnetic iron oxide particles using a clinical 1.5-T magnetic resonance scanner. Cancer Res 2007;67(4):1555–62.
52. Liu G, Rugo HS, Wilding G, et al. Dynamic contrast-enhanced magnetic resonance imaging as a pharmacodynamic measure of response after acute dosing of AG-013736, an oral angiogenesis inhibitor, in patients with advanced solid tumors: results from a phase I study. J Clin Oncol 2005;23(24):5464–73.
53. Thomas AL, Morgan B, Horsfield MA, et al. Phase I study of the safety, tolerability, pharmacokinetics, and pharmacodynamics of PTK787/ZK 222584 administered twice daily in patients with advanced cancer. J Clin Oncol 2005;23(18):4162–71.
54. Medved M, Karczmar G, Yang C, et al. Semiquantitative analysis of dynamic contrast enhanced MRI in cancer patients: Variability and changes in tumor tissue over time. J Magn Reson Imaging 2004; 20(1):122–8.
55. Padhani AR. MRI for assessing antivascular cancer treatments. Br J Radiol 2003;76(Spec No 1): S60–80.
56. Marzola P, Degrassi A, Calderan L, et al. In vivo assessment of antiangiogenic activity of SU6668 in an experimental colon carcinoma model. Clin Cancer Res 2004;10(2):739–50.
57. Faccioli N, Marzola P, Boschi F, et al. Pathological animal models in the experimental evaluation of tumour microvasculature with magnetic resonance imaging. Radiol Med (Torino) 2007;112(3):319–28.
58. Williams DS. Quantitative perfusion imaging using arterial spin labeling. Methods Mol Med 2006;124: 151–73.

Author's personal copy

59. Liu TT, Brown GG. Measurement of cerebral perfusion with arterial spin labeling: Part 1. Methods. J Int Neuropsychol Soc 2007;13(3):517–25.
60. Wolf RL, Detre JA. Clinical neuroimaging using arterial spin-labeled perfusion magnetic resonance imaging. Neurotherapeutics 2007;4(3):346–59.
61. Hsu YY, Chang CN, Jung SM, et al. Blood oxygenation level-dependent MRI of cerebral gliomas during breath holding. J Magn Reson Imaging 2004;19(2):160–7.
62. Baudelet C, Cron GO, Gallez B. Determination of the maturity and functionality of tumor vasculature by MRI: correlation between BOLD-MRI and DCE-MRI using P792 in experimental fibrosarcoma tumors. Magn Reson Med 2006;56(5):1041–9.
63. Fleischer AC, Wojcicki WE, Donnelly EF, et al. Quantified color Doppler sonography of tumor vascularity in an animal model. J Ultrasound Med 1999;18(8):547–51.
64. Forsberg F, Ro RJ, Potoczek M, et al. Assessment of angiogenesis: implications for ultrasound imaging. Ultrasonics 2004;42(1–9):325–30.
65. Drevs J, Hofmann I, Hugenschmidt H, et al. Effects of PTK787/ZK 222584, a specific inhibitor of vascular endothelial growth factor receptor tyrosine kinases, on primary tumor, metastasis, vessel density, and blood flow in a murine renal cell carcinoma model. Cancer Res 2000;60(17):4819–24.
66. Liang JD, Yang PM, Liang PC, et al. Three-dimensional power Doppler ultrasonography for demonstrating associated arteries of hepatocellular carcinoma. J Formos Med Assoc 2003;102(6): 367–74.
67. Stride E, Saffari N. Microbubble ultrasound contrast agents: a review. Proc Inst Mech Eng [H] 2003;217(6):429–47.
68. Niermann KJ, Fleischer AC, Huamani J, et al. Measuring tumor perfusion in control and treated murine tumors: correlation of microbubble contrast-enhanced sonography to dynamic contrast-enhanced magnetic resonance imaging and fluorodeoxyglucose positron emission tomography. J Ultrasound Med 2007;26(6):749–56.
69. Wilson SR, Burns PN, Muradali D, et al. Harmonic hepatic US with microbubble contrast agent: initial experience showing improved characterization of hemangioma, hepatocellular carcinoma, and metastasis. Radiology 2000;215(1):153–61.
70. Burns PN, Wilson SR, Simpson DH. Pulse inversion imaging of liver blood flow: improved method for characterizing focal masses with microbubble contrast. Invest Radiol 2000;35(1):58–71.
71. Quaia E. Microbubble ultrasound contrast agents: an update. Eur Radiol 2007;17(8):1995–2008.
72. Cornud F, Hamida K, Flam T, et al. Endorectal color Doppler sonography and endorectal MR imaging features of nonpalpable prostate cancer: correlation with radical prostatectomy findings. Am J Roentgenol 2000;175(4):1161–8.
73. McCarville MB, Streck CJ, Dickson PV, et al. Angiogenesis inhibitors in a murine neuroblastoma model: quantitative assessment of intratumoral blood flow with contrast-enhanced gray-scale US. Radiology 2006;240(1):73–81.
74. Stieger SM, Bloch SH, Foreman O, et al. Ultrasound assessment of angiogenesis in a matrigel model in rats. Ultrasound Med Biol 2006;32(5):673–81.
75. Ferrara KW, Merritt CR, Burns PN, et al. Evaluation of tumor angiogenesis with US: imaging, Doppler, and contrast agents. Acad Radiol 2000;7(10): 824–39.
76. Hughes MS, Marsh JN, Zhang H, et al. Characterization of digital waveforms using thermodynamic analogs: detection of contrast-targeted tissue in vivo. IEEE Trans Ultrason Ferroelectr Freq Control 2006;53(9):1609–16.
77. Lassau N, Lamuraglia M, Chami L, et al. Gastrointestinal stromal tumors treated with imatinib: monitoring response with contrast-enhanced sonography. Am J Roentgenol 2006;187(5):1267–73.
78. Li PC, Yang MJ. Transfer function analysis of ultrasonic time-intensity measurements. Ultrasound Med Biol 2003;29(10):1493–500.
79. Lavisse S, Lejeune P, Rouffiac V, et al. Early quantitative evaluation of a tumor vasculature disruptive agent AVE8062 using dynamic contrast-enhanced ultrasonography. Invest Radiol 2008;43(2):100–11.
80. Haider MA, Milosevic M, Fyles A, et al. Assessment of the tumor microenvironment in cervix cancer using dynamic contrast enhanced CT, interstitial fluid pressure and oxygen measurements. Int J Radiat Oncol Biol Phys 2005;62(4):1100–7.
81. Bisdas S, Konstantinou GN, Lee PS, et al. Dynamic contrast-enhanced CT of head and neck tumors: perfusion measurements using a distributed-parameter tracer kinetic model. Initial results and comparison with deconvolution-based analysis. Phys Med Biol 2007;52(20):6181–96.
82. Larson DR, Zipfel WR, Williams RM, et al. Water-soluble quantum dots for multiphoton fluorescence imaging in vivo. Science 2003;300(5624):1434–6.
83. Brown EB, Campbell RB, Tsuzuki Y, et al. In vivo measurement of gene expression, angiogenesis and physiological function in tumors using multiphoton laser scanning microscopy. Nat Med 2001;7(7):864–8.
84. Montet X, Ntziachristos V, Grimm J, et al. Tomographic fluorescence mapping of tumor targets. Cancer Res 2005;65(14):6330–6.
85. Jones T. The imaging science of positron emission tomography. Eur J Nucl Med 1996;23(7):807–13.
86. Laking GR, Price PM. Positron emission tomographic imaging of angiogenesis and vascular function. Br J Radiol 2003;76(Spec No 1):S50–9.

Author's personal copy

87. Phelps ME, Hoffman EJ, Mullani NA, et al. Application of annihilation coincidence detection to transaxial reconstruction tomography. J Nucl Med 1975;16(3):210–24.
88. Phelps ME. PET: the merging of biology and imaging into molecular imaging. J Nucl Med 2000;41(4):661–81.
89. Willmann JK, van Bruggen N, Dinkelborg LM, et al. Molecular imaging in drug development. Nat Rev Drug Discov 2008;7(7):591–607.
90. Beyer T, Townsend DW, Brun T, et al. A combined PET/CT scanner for clinical oncology. J Nucl Med 2000;41(8):1369–79.
91. Kamel E, Hany TF, Burger C, et al. CT vs 68Ge attenuation correction in a combined PET/CT system: evaluation of the effect of lowering the CT tube current. Eur J Nucl Med Mol Imaging 2002; 29(3):346–50.
92. Cherry SR, Shao Y, Silverman RW, et al. MicroPET: a high resolution PET scanner for imaging small animals. IEEE Trans Nucl Sci 1997;44(3):1161–6.
93. Chatziioannou AF, Cherry SR, Shao Y, et al. Performance evaluation of microPET: a high-resolution lutetium oxyorthosilicate PET scanner for animal imaging. J Nucl Med 1999;40(7):1164–75.
94. Pichler BJ, Judenhofer MS, Pfannenberg C. Multimodal imaging approaches: PET/CT and PET/MRI. Handb Exp Pharmacol 2008;185(I):109–32.
95. Laking GR, West C, Buckley DL, et al. Imaging vascular physiology to monitor cancer treatment. Crit Rev Oncol Hematol 2006;58(2):95–113.
96. Anderson RE. Cerebral blood flow xenon-133. Neurosurg Clin N Am 1996;7(4):703–8.
97. Wilson RA, Shea MJ, De Landsheere CM, et al. Validation of quantitation of regional myocardial blood flow in vivo with 11C-labeled human albumin microspheres and positron emission tomography. Circulation 1984;70(4):717–23.
98. Dimitrakopoulou-Strauss A, Strauss LG, Burger C. Quantitative PET studies in pretreated melanoma patients: a comparison of 6-[^{18}F]fluoro-L-dopa with ^{18}F-FDG and ^{15}O-water using compartment and noncompartment analysis. J Nucl Med 2001; 42(2):248–56.
99. Acierno LJ. Adolph Fick: mathematician, physicist, physiologist. Clin Cardiol 2000;23(5):390–1.
100. Lammertsma AA, Jones T. Low oxygen extraction fraction in tumours measured with the oxygen-15 steady state technique: effect of tissue heterogeneity. Br J Radiol 1992;65(776):697–700.
101. Iida H, Takahashi A, Tamura Y, et al. Myocardial blood flow: comparison of oxygen-15-water bolus injection, slow infusion and oxygen-15-carbon dioxide slow inhalation. J Nucl Med 1995;36(1):78–85.
102. Wilson CB, Lammertsma AA, McKenzie CG, et al. Measurements of blood flow and exchanging water space in breast tumors using positron emission tomography: a rapid and noninvasive dynamic method. Cancer Res 1992;52(6):1592–7.
103. Anderson H, Price P. Clinical measurement of blood flow in tumours using positron emission tomography: a review. Nucl Med Commun 2002;23(2):131–8.
104. Tseng J, Dunnwald LK, Schubert EK, et al. 18F-FDG kinetics in locally advanced breast cancer: correlation with tumor blood flow and changes in response to neoadjuvant chemotherapy. J Nucl Med 2004;45(11):1829–37.
105. Hoffend J, Mier W, Schuhmacher J, et al. Gallium-68-DOTA-albumin as a PET blood-pool marker: experimental evaluation in vivo. Nucl Med Biol 2005;32(3):287–92.
106. Sipkins DA, Cheresh DA, Kazemi MR, et al. Detection of tumor angiogenesis in vivo by alphaVbeta3-targeted magnetic resonance imaging. Nat Med 1998;4(5):623–6.
107. Wierzbicka-Patynowski I, Niewiarowski S, Marcinkiewicz C, et al. Structural requirements of echistatin for the recognition of alpha vbeta 3 and alpha 5beta 1 Integrins. J Biol Chem 1999; 274(53):37809–14.
108. Cai W, Shin DW, Chen K, et al. Peptide-labeled near-infrared quantum dots for imaging tumor vasculature in living subjects. Nano Lett 2006; 6(4):669–76.
109. Hood JD, Cheresh DA. Role of integrins in cell invasion and migration. Nat Rev Cancer 2002;2(2):91–100.
110. Chen X. Multimodality imaging of tumor integrin alphavbeta3 expression. Mini Rev Med Chem 2006; 6(2):227–34.
111. Hynes RO. Integrins: bidirectional, allosteric signaling machines. Cell 2002;110(6):673–87.
112. Xiong JP, Stehle T, Zhang R, et al. Crystal structure of the extracellular segment of integrin a_vb_3 in complex with an Arg-Gly-Asp ligand. Science 2002;296(5565):151–5.
113. Ruoslahti E, Pierschbacher MD. New perspectives in cell adhesion: RGD and integrins. Science 1987; 238(4826):491–7.
114. Jin H, Varner J. Integrins: roles in cancer development and as treatment targets. Br J Cancer 2004; 90(3):561–5.
115. Mizejewski GJ. Role of integrins in cancer: survey of expression patterns (44435). Proc Soc Exp Biol Med 1999;222(2):124–38.
116. Cai W, Chen X. Anti-angiogenic cancer therapy based on integrin a_vb_3 antagonism. Anticancer Agents Med Chem 2006;6:407–28.
117. Brooks PC, Stromblad S, Sanders LC, et al. Localization of matrix metalloproteinase MMP-2 to the surface of invasive cells by interaction with integrin a_vb_3. Cell 1996;85(5):683–93.
118. Yang JT, Rayburn H, Hynes RO. Embryonic mesodermal defects in a_5 integrin-deficient mice. Development 1993;119(4):1093–105.

Author's personal copy

119. Goh KL, Yang JT, Hynes RO. Mesodermal defects and cranial neural crest apoptosis in a_5 integrin-null embryos. Development 1997; 124(21):4309–19.
120. Taverna D, Hynes RO. Reduced blood vessel formation and tumor growth in a_5-integrin-negative teratocarcinomas and embryoid bodies. Cancer Res 2001;61(13):5255–61.
121. Yang JT, Rayburn H, Hynes RO. Cell adhesion events mediated by a_4 integrins are essential in placental and cardiac development. Development 1995;121(2):549–60.
122. Aumailley M, Gurrath M, Muller G, et al. Arg-Gly-Asp constrained within cyclic pentapeptides. Strong and selective inhibitors of cell adhesion to vitronectin and laminin fragment P1. FEBS Lett 1991;291(1):50–4.
123. Haubner R, Finsinger D, Kessler H. Stereoisomeric peptide libraries and peptidomimetics for designing selective inhibitors of the $\alpha_v\beta_3$ integrin for a new cancer therapy. Angew Chem Int Ed Engl 1997;36:1374–89.
124. Haubner R, Wester HJ, Reuning U, et al. Radiolabeled alpha(v)beta3 integrin antagonists: a new class of tracers for tumor targeting. J Nucl Med 1999;40(6):1061–71.
125. Haubner R, Wester HJ, Weber WA, et al. Noninvasive imaging of alpha(v)beta3 integrin expression using 18F-labeled RGD-containing glycopeptide and positron emission tomography. Cancer Res 2001;61(5):1781–5.
126. Haubner R. Alphavbeta3-integrin imaging: a new approach to characterise angiogenesis? Eur J Nucl Med Mol Imaging 2006;33(Suppl 1):54–63.
127. Harris JM, Martin NE, Modi M. PEGylation: a novel process for modifying pharmacokinetics. Clin Pharmacokinet 2001;40(7):539–51.
128. Chen X, Park R, Shahinian AH, et al. Pharmacokinetics and tumor retention of 125I-labeled RGD peptide are improved by PEGylation. Nucl Med Biol 2004;31(1):11–9.
129. Noiri E, Goligorsky MS, Wang GJ, et al. Biodistribution and clearance of 99mTc-labeled Arg-Gly-Asp (RGD) peptide in rats with ischemic acute renal failure. J Am Soc Nephrol 1996;7(12):2682–8.
130. Chen X, Hou Y, Tohme M, et al. PEGylated Arg-Gly-Asp peptide: 64Cu labeling and PET imaging of brain tumor alphavbeta3-integrin expression. J Nucl Med 2004;45(10):1776–83.
131. Dijkgraaf I, Liu S, Kruijtzer JA, et al. Effects of linker variation on the in vitro and in vivo characteristics of an 111In-labeled RGD peptide. Nucl Med Biol 2007;34(1):29–35.
132. Li ZB, Chen K, Chen X. (68)Ga-labeled multimeric RGD peptides for microPET imaging of integrin alpha(v)beta (3) expression. Eur J Nucl Med Mol Imaging 2008;35(6):1100–8.
133. van Hagen PM, Breeman WA, Bernard HF, et al. Evaluation of a radiolabelled cyclic DTPA-RGD analogue for tumour imaging and radionuclide therapy. Int J Cancer 2000;90(4):186–98.
134. Bach-Gansmo T, Danielsson R, Saracco A, et al. Integrin receptor imaging of breast cancer: a proof-of-concept study to evaluate 99mTc-NC100692. J Nucl Med 2006;47(9):1434–9.
135. Haubner R, Wester HJ, Burkhart F, et al. Glycosylated RGD-containing peptides: tracer for tumor targeting and angiogenesis imaging with improved biokinetics. J Nucl Med 2001;42(2): 326–36.
136. Haubner R, Kuhnast B, Mang C, et al. [18F]Galacto-RGD: synthesis, radiolabeling, metabolic stability, and radiation dose estimates. Bioconjug Chem 2004;15(1):61–9.
137. Haubner R, Weber WA, Beer AJ, et al. Noninvasive visualization of the activated alphavbeta3 integrin in cancer patients by positron emission tomography and [18F]Galacto-RGD. PLoS Med 2005; 2(3):e70.
138. Beer AJ, Haubner R, Goebel M, et al. Biodistribution and pharmacokinetics of the alphavbeta3-selective tracer 18F-galacto-RGD in cancer patients. J Nucl Med 2005;46(8):1333–41.
139. Beer AJ, Haubner R, Wolf I, et al. PET-based human dosimetry of 18F-galacto-RGD, a new radiotracer for imaging alpha v beta3 expression. J Nucl Med 2006;47(5):763–9.
140. Beer AJ, Haubner R, Sarbia M, et al. Positron emission tomography using [18F]Galacto-RGD identifies the level of integrin alpha(v)beta3 expression in man. Clin Cancer Res 2006;12(13):3942–9.
141. Beer AJ, Grosu AL, Carlsen J, et al. [18F]galacto-RGD positron emission tomography for imaging of alphavbeta3 expression on the neovasculature in patients with squamous cell carcinoma of the head and neck. Clin Cancer Res 2007;13(22 Pt 1):6610–6.
142. Beer AJ, Lorenzen S, Metz S, et al. Comparison of integrin alphaVbeta3 expression and glucose metabolism in primary and metastatic lesions in cancer patients: a PET study using 18F-galacto-RGD and 18F-FDG. J Nucl Med 2008;49(1):22–9.
143. Boturyn D, Coll JL, Garanger E, et al. Template assembled cyclopeptides as multimeric system for integrin targeting and endocytosis. J Am Chem Soc 2004;126(18):5730–9.
144. Chen X, Tohme M, Park R, et al. Micro-PET imaging of alphavbeta3-integrin expression with 18F-labeled dimeric RGD peptide. Mol Imaging 2004; 3(2):96–104.
145. Zhang X, Xiong Z, Wu Y, et al. Quantitative PET imaging of tumor integrin alphavbeta3 expression with 18F-FRGD2. J Nucl Med 2006;47(1):113–21.
146. Chen X, Park R, Tohme M, et al. MicroPET and autoradiographic imaging of breast cancer alpha

Author's personal copy

v-integrin expression using 18F- and 64Cu-labeled RGD peptide. Bioconjug Chem 2004;15(1):41–9.
147. Chen X, Liu S, Hou Y, et al. MicroPET imaging of breast cancer alphav-integrin expression with 64Cu-labeled dimeric RGD peptides. Mol Imaging Biol 2004;6(5):350–9.
148. Wu Z, Li ZB, Chen K, et al. MicroPET of tumor integrin alphavbeta3 expression using 18F-labeled PEGylated tetrameric RGD peptide (18F-FPRGD4). J Nucl Med 2007;48(9):1536–44.
149. Li ZB, Cai W, Cao Q, et al. (64)Cu-labeled tetrameric and octameric RGD peptides for small-animal PET of tumor alpha(v)beta(3) integrin expression. J Nucl Med 2007;48(7):1162–71.
150. Thumshirn G, Hersel U, Goodman SL, et al. Multimeric cyclic RGD peptides as potential tools for tumor targeting: solid-phase peptide synthesis and chemoselective oxime ligation. Chemistry 2003;9(12):2717–25.
151. Poethko T, Schottelius M, Thumshirn G, et al. Two-step methodology for high-yield routine radiohalogenation of peptides: (18)F-labeled RGD and octreotide analogs. J Nucl Med 2004;45(5):892–902.
152. Cai W, Wu Y, Chen K, et al. In vitro and in vivo characterization of 64Cu-labeled AbegrinTM, a humanized monoclonal antibody against integrin avb3. Cancer Res 2006;66(19):9673–81.
153. Higuchi T, Bengel FM, Seidl S, et al. Assessment of alphavbeta3 integrin expression after myocardial infarction by positron emission tomography. Cardiovasc Res 2008;78(2):395–403.
154. Ferrara N. VEGF and the quest for tumour angiogenesis factors. Nat Rev Cancer 2002;2(10):795–803.
155. Broumas AR, Pollard RE, Bloch SH, et al. Contrast-enhanced computed tomography and ultrasound for the evaluation of tumor blood flow. Invest Radiol 2005;40(3):134–47.
156. Hicklin DJ, Ellis LM. Role of the vascular endothelial growth factor pathway in tumor growth and angiogenesis. J Clin Oncol 2005;23(5):1011–27.
157. Sun J, Wang DA, Jain RK, et al. Inhibiting angiogenesis and tumorigenesis by a synthetic molecule that blocks binding of both VEGF and PDGF to their receptors. Oncogene 2005;24(29):4701–9.
158. Watanabe H, Mamelak AJ, Wang B, et al. Anti-vascular endothelial growth factor receptor-2 (Flk-1/KDR) antibody suppresses contact hypersensitivity. Exp Dermatol 2004;13(11):671–81.
159. Prewett M, Huber J, Li Y, et al. Antivascular endothelial growth factor receptor (fetal liver kinase 1) monoclonal antibody inhibits tumor angiogenesis and growth of several mouse and human tumors. Cancer Res 1999;59(20):5209–18.
160. Ciardiello F, Caputo R, Damiano V, et al. Antitumor effects of ZD6474, a small molecule vascular endothelial growth factor receptor tyrosine kinase inhibitor, with additional activity against epidermal growth factor receptor tyrosine kinase. Clin Cancer Res 2003;9(4):1546–56.
161. Wedge SR, Ogilvie DJ, Dukes M, et al. ZD4190: an orally active inhibitor of vascular endothelial growth factor signaling with broad-spectrum antitumor efficacy. Cancer Res 2000;60(4):970–5.
162. Kennedy JE, ter Haar GR, Wu F, et al. Contrast-enhanced ultrasound assessment of tissue response to high-intensity focused ultrasound. Ultrasound Med Biol 2004;30(6):851–4.
163. Cai W, Chen X. Multimodality imaging of vascular endothelial growth factor and vascular endothelial growth factor receptor expression. Front Biosci 2007;12:4267–79.
164. Nagengast WB, de Vries EG, Hospers GA, et al. In vivo VEGF imaging with radiolabeled bevacizumab in a human ovarian tumor xenograft. J Nucl Med 2007;48(8):1313–9.
165. Collingridge DR, Carroll VA, Glaser M, et al. The development of [^{124}I]iodinated-VG76e: a novel tracer for imaging vascular endothelial growth factor in vivo using positron emission tomography. Cancer Res 2002;62(20):5912–9.
166. Jayson GC, Zweit J, Jackson A, et al. Molecular imaging and biological evaluation of HuMV833 anti-VEGF antibody: implications for trial design of antiangiogenic antibodies. J Natl Cancer Inst 2002;94(19):1484–93.
167. Scheer MG, Stollman TH, Boerman OC, et al. Imaging liver metastases of colorectal cancer patients with radiolabelled bevacizumab: Lack of correlation with VEGF-A expression. Eur J Cancer 2008;44(13):1835–40.
168. Strauss LG, Koczan D, Klippel S, et al. Impact of angiogenesis-related gene expression on the tracer kinetics of 18F-FDG in colorectal tumors. J Nucl Med 2008;49(8):1238–44.
169. Hsu AR, Cai W, Veeravagu A, et al. Multimodality molecular imaging of glioblastoma growth inhibition with vasculature-targeting fusion toxin VEGF121/rGel. J Nucl Med 2007;48(3):445–54.
170. Cai W, Chen K, Mohamedali KA, et al. PET of vascular endothelial growth factor receptor expression. J Nucl Med 2006;47(12):2048–56.
171. Chen K, Cai W, Li ZB, et al. Quantitative PET Imaging of VEGF receptor expression. Mol Imaging Biol 2008;11(1):15–22.
172. Backer MV, Levashova Z, Patel V, et al. Molecular imaging of VEGF receptors in angiogenic vasculature with single-chain VEGF-based probes. Nat Med 2007;13(4):504–9.
173. Li J, Brown LF, Hibberd MG, et al. VEGF, flk-1, and flt-1 expression in a rat myocardial infarction model of angiogenesis. Am J Physiol 1996;270(5 Pt 2):H1803–11.
174. Soeki T, Tamura Y, Shinohara H, et al. Serial changes in serum VEGF and HGF in patients with

Author's personal copy

acute myocardial infarction. Cardiology 2000; 93(3):168–74.
175. Rodriguez-Porcel M, Cai W, Gheysens O, et al. Imaging of VEGF receptor in a rat myocardial infarction model using PET. J Nucl Med 2008; 49(4):667–73.
176. Willmann JK, Paulmurugan R, Chen K, et al. Ultrasonic imaging of tumor angiogenesis with contrast microbubbles targeted to vascular endothelial growth factor type 2 receptor [revision]. Radiology 2007;246(2):508–18.
177. Cai W, Guzman R, Hsu AR, et al. Positron emission tomography imaging of poststroke angiogenesis. Stroke 2008;40(1):270–7.
178. Simon M, Rockl W, Hornig C, et al. Receptors of vascular endothelial growth factor/vascular permeability factor (VEGF/VPF) in fetal and adult human kidney: localization and [125I]VEGF binding sites. J Am Soc Nephrol 1998;9(6):1032–44.
179. Keyt BA, Nguyen HV, Berleau LT, et al. Identification of vascular endothelial growth factor determinants for binding KDR and FLT-1 receptors. Generation of receptor-selective VEGF variants by site-directed mutagenesis. J Biol Chem 1996; 271(10):5638–46.
180. Wang H, Cai W, Chen K, et al. A new PET tracer specific for vascular endothelial growth factor receptor 2. Eur J Nucl Med Mol Imaging 2007; 34(12):2001–10.
181. Wagner S, Breyholz HJ, Faust A, et al. Molecular imaging of matrix metalloproteinases in vivo using small molecule inhibitors for SPECT and PET. Curr Med Chem 2006;13(23):2819–38.
182. Folgueras AR, Pendas AM, Sanchez LM, et al. Matrix metalloproteinases in cancer: from new functions to improved inhibition strategies. Int J Dev Biol 2004;48(5–6):411–24.
183. Johnson JL, George SJ, Newby AC, et al. Divergent effects of matrix metalloproteinases 3, 7, 9, and 12 on atherosclerotic plaque stability in mouse brachiocephalic arteries. Proc Natl Acad Sci U S A 2005;102(43):15575–80.
184. Hidalgo M, Eckhardt SG. Development of matrix metalloproteinase inhibitors in cancer therapy. J Natl Cancer Inst 2001;93(3):178–93.
185. Li WP, Anderson CJ. Imaging matrix metalloproteinase expression in tumors. Q J Nucl Med 2003; 47(3):201–8.
186. Lee S, Park K, Kim K, et al. Activatable imaging probes with amplified fluorescent signals. Chem Commun (Camb) 2008;(36):4250–60.
187. Lee S, Park K, Lee SY, et al. Dark quenched matrix metalloproteinase fluorogenic probe for imaging osteoarthritis development in vivo. Bioconjug Chem 2008;19(9):1743–7.
188. Bremer C, Bredow S, Mahmood U, et al. Optical imaging of matrix metalloproteinase-2 activity in tumors: feasibility study in a mouse model. Radiology 2001;221(2):523–9.
189. Medina OP, Kairemo K, Valtanen H, et al. Radionuclide imaging of tumor xenografts in mice using a gelatinase-targeting peptide. Anticancer Res 2005;25(1A):33–42.
190. Hanaoka H, Mukai T, Habashita S, et al. Chemical design of a radiolabeled gelatinase inhibitor peptide for the imaging of gelatinase activity in tumors. Nucl Med Biol 2007;34(5):503–10.
191. Sprague JE, Li WP, Liang K, et al. In vitro and in vivo investigation of matrix metalloproteinase expression in metastatic tumor models. Nucl Med Biol 2006;33(2):227–37.
192. Zheng QH, Fei X, Liu X, et al. Synthesis and preliminary biological evaluation of MMP inhibitor radiotracers [11C]methyl-halo-CGS 27023A analogs, new potential PET breast cancer imaging agents. Nucl Med Biol 2002;29(7):761–70.
193. Furumoto S, Takashima K, Kubota K, et al. Tumor detection using 18F-labeled matrix metalloproteinase-2 inhibitor. Nucl Med Biol 2003;30(2):119–25.
194. Wagner S, Breyholz HJ, Law MP, et al. Novel fluorinated derivatives of the broad-spectrum MMP inhibitors N-hydroxy-2(R)-[[(4-methoxyphenyl)sulfonyl](benzyl)- and (3-picolyl)-amino]-3-methylbutanamide as potential tools for the molecular imaging of activated MMPs with PET. J Med Chem 2007;50(23):5752–64.
195. Zheng QH, Fei X, Liu X, et al. Comparative studies of potential cancer biomarkers carbon-11 labeled MMP inhibitors (S)-2-(4′-[11C]methoxybiphenyl-4-sulfonylamino)-3-methylbutyric acid and N-hydroxy-(R)-2-[[(4′-[11C]methoxyphenyl)sulfonyl]benzylamino]-3-methylbut anamide. Nucl Med Biol 2004;31(1):77–85.
196. Zheng QH, Fei X, DeGrado TR, et al. Synthesis, biodistribution and micro-PET imaging of a potential cancer biomarker carbon-11 labeled MMP inhibitor (2R)-2-[[4-(6-fluorohex-1-ynyl)phenyl]sulfonylamino]-3-methylbutyric acid [11C]methyl ester. Nucl Med Biol 2003;30(7):753–60.
197. Kulasegaram R, Giersing B, Page CJ, et al. In vivo evaluation of 111In-DTPA-N-TIMP-2 in Kaposi sarcoma associated with HIV infection. Eur J Nucl Med 2001;28(6):756–61.
198. Neri D, Carnemolla B, Nissim A, et al. Targeting by affinity-matured recombinant antibody fragments of an angiogenesis associated fibronectin isoform. Nat Biotechnol 1997;15(12):1271–5.
199. Santimaria M, Moscatelli G, Viale GL, et al. Immunoscintigraphic detection of the ED-B domain of fibronectin, a marker of angiogenesis, in patients with cancer. Clin Cancer Res 2003;9(2):571–9.
200. Suri C, Jones PF, Patan S, et al. Requisite role of angiopoietin-1, a ligand for the TIE2 receptor, during embryonic angiogenesis. Cell 1996;87(7):1171–80.

Author's personal copy

201. Seaman S, Stevens J, Yang MY, et al. Genes that distinguish physiological and pathological angiogenesis. Cancer Cell 2007;11(6):539–54.
202. Shao Y, Cherry SR, Farahani K, et al. Simultaneous PET and MR imaging. Phys Med Biol 1997;42(10):1965–70.
203. Townsend DW, Beyer T. A combined PET/CT scanner: the path to true image fusion. Br J Radiol 2002;75(Spec No):S24–30.
204. Catana C, Wu Y, Judenhofer MS, et al. Simultaneous acquisition of multislice PET and MR images: initial results with a MR-compatible PET scanner. J Nucl Med 2006;47(12):1968–76.
205. Cai W, Chen K, He L, et al. Quantitative PET of EGFR expression in xenograft-bearing mice using ^{64}Cu-labeled cetuximab, a chimeric anti-EGFR monoclonal antibody. Eur J Nucl Med Mol Imaging 2007;34:850–8 [Epub].
206. Cai W, Ebrahimnejad A, Chen K, et al. Quantitative radioimmunoPET imaging of EphA2 in tumour-bearing mice. Eur J Nucl Med Mol Imaging 2007; 34(12):2024–36.
207. Li ZB, Wu Z, Chen K, et al. 18F-labeled BBN-RGD heterodimer for prostate cancer imaging. J Nucl Med 2008;49(3):453–61.
208. Jung KH, Lee KH, Paik JY, et al. Favorable biokinetic and tumor-targeting properties of 99mTc-labeled glucosamino RGD and effect of paclitaxel therapy. J Nucl Med 2006;47(12):2000–7.